

**COMPUTATIONAL STUDIES OF HORIZONTAL AXIS WIND
TURBINES IN HIGH WIND SPEED CONDITION USING
ADVANCED TURBULENCE MODELS**

A Thesis
Presented to
The Academic Faculty

by

Sarun Benjanirat

In Partial Fulfillment
of the Requirements for the Degree of
Doctor of Philosophy in the
School of Aerospace Engineering

Georgia Institute of Technology
December 2006

COPYRIGHT 2006 BY SARUN BENJANIRAT

**COMPUTATIONAL STUDIES OF HORIZONTAL AXIS WIND
TURBINES IN HIGH WIND SPEED CONDITION USING
ADVANCED TURBULENCE MODELS**

Approved by:

Dr. Lakshmi N. Sankar, Advisor
School of Aerospace Engineering
Georgia Institute of Technology

Dr. P.K. Yeung
School of Aerospace Engineering
Georgia Institute of Technology

Dr. Stephen Ruffin
School of Aerospace Engineering
Georgia Institute of Technology

Dr. Samuel V. Shelton
School of Mechanical Engineering
Georgia Institute of Technology

Dr. Marilyn Smith
School of Aerospace Engineering
Georgia Institute of Technology

Date Approved: August 21, 2006

Dedicated to my parents

ACKNOWLEDGEMENTS

I would like to especially thank my thesis advisor, Dr. Lakshmi N. Sankar, for his useful guidance and firm support. He has encouraged me and made my life at Georgia Tech a positive learning experience. I would like to also thank Dr. P. K. Yeung, Dr. Stephen Ruffin, Dr. Marilyn Smith, and Dr. Samuel V. Shelton for serving in my reading and thesis committee.

I would like to thank Dr. Earl Duque and his colleagues for supporting me with valuable information and discussions that assisted me in working through many problems. I would like to thank Mr. Michael Robinson for wind turbine test information that was very useful in my work. I must not forget Dr. Guanpeng Xu for guiding me through the computational method and his valuable advice on several issues.

The funding for my research was provided by the National Renewable Energy Laboratory. I am grateful in particular to Dr. Scott Schreck for encouraging me to move forward confidently in my research work. I must also thank Dr. J. I. Jagoda for coordinating the support during the last two semesters.

Working at Georgia Tech has been very enjoyable, though challenging. I have been supported throughout this experience by many special people. I would like to thank all of my CFD colleagues, Dr. Liu Yi, Dr. Ebru Usta, Dr. Gang Wang, Vishwas Iyengar, Mina A. Zaki, Chanin Tongchitpakdee, Nandita Yeshala, and Dr. Roxana Vasilescu who have supported me generously. Many thanks also to Karthick Mani, Sujeet Phanse, Nichint Rajmohan, and Joseph Gillman for proofreading my thesis.

Lastly I must thank my parents and sisters who have encouraged me from Thailand on weekly basis. I also thank all of my Thai friends both here in and in Thailand for providing everything I need.

TABLE OF CONTENTS

	Page
ACKNOWLEDGEMENTS.....	iv
LIST OF TABLES.....	x
LIST OF FIGURES.....	xi
NOMENCLATURE.....	xv
SUMMARY.....	xix
CHAPTER 1:INTRODUCTION	1
1.1 Background.....	1
1.2 The Future of Wind Energy	5
1.3 Power Regulation Methods.....	8
1.4 Survey of Available Methods for Aerodynamic Modeling of HAWTs	10
1.4.1 Blade Element Momentum Theory.....	10
1.4.2 Lifting Surface, Prescribed-Wake Code	11
1.4.3 Navier-Stokes Solvers.....	12
1.4.4 Hybrid Methodology.....	14
1.5 Research Objectives and Scope	16
CHAPTER 2:NREL PHASE VI ROTOR	17
2.1 Background.....	17
2.2 Phase VI Rotor.....	18
2.3 Unsteady Aerodynamics Experiments.....	19
2.3.1 Forces Coefficients	22

CHAPTER 3:MATHEMATICAL FORMULATION.....	25
3.1 Governing Equations	25
3.1.1 Non-Dimensionalization of Governing Equations.....	28
3.1.2 Governing Equations in Generalized Coordinates.....	30
3.1.3 Numerical formulation.....	32
3.2 Tip and Root Vortices Modeling	35
3.3 Time Marching Algorithm.....	35
3.4 Initial Conditions	36
3.5 Boundary Conditions	37
3.6 Turbulence Models	38
3.6.1 Baldwin-Lomax Model.....	38
3.6.2 The k- ϵ Model.....	41
3.7 Transition Models	42
3.7.1 Eppler's Transition Model.....	42
3.7.2 Michel's Transition Model	43
CHAPTER 4:ENHACNCEMENTS.....	46
4.1 Turbulence Models	46
4.1.1 Spalart-Allmaras model	47
4.1.2 Spalart-Allmaras Detached Eddy Simulation	56
4.1.3 k- ω SST Model.....	59
4.2 The LU SGS Process	67
CHAPTER 5:WIND TURBINE STATES	69
5.1 The Actuator Disc Concept.....	69

5.2 Momentum Theory	70
5.3 Wind Rotor States	72
5.4 States of Phase VI Rotors	75
CHAPTER 6:RESULTS AND DISCUSSION.....	77
6.1 Computational Setting	77
6.1.1 Available Computational Options.....	77
6.1.2 Effect of the Shed Vortices	79
6.1.3 Grid	79
6.1.4 CFL Number	81
6.1.5 Issues with Compressible Navier-Stokes Equations.....	82
6.2 Grid Sensitivity Study.....	83
6.3 Performance of the Advanced Turbulence Models	84
6.2.1 Computational Cost	85
6.3.2 Torque and Bending Moments.....	86
6.3.3 k- ω SST Model Issues	88
6.3.4 Force Coefficients	90
6.4 Effect of Transition Models	101
6.4.1 Computational Cost associated with the Transitional Models.....	101
6.4.2 Force Coefficients	101
CHAPTER 7:CONCLUSIONS AND RECOMMENDATIONS	106
APPENDIX A:VALIDATION OF TURBULENCE MODELS	110
A.1 Numerical Results	111
REFERENCES	120

VITA.....127

LIST OF TABLES

	Page
Table 2.1 Previous NREL rotor models.....	17
Table 2.2 NASA Ames Test Configuration.....	20
Table 6.1 Computational cost of each grid density.....	83
Table 6.2 Computational cost of turbulence models	85

LIST OF FIGURES

	Page
Figure 1.1 Persian panemone	1
Figure 1.2 Modern-day panemone	2
Figure 1.3 Bush Postmill, the first wind turbine, which attached to an electricity generator	4
Figure 1.4 Poul La Cour wind turbine	4
Figure 1.5 US wind energy map	6
Figure 1.6 Growth of commercial wind turbine size	7
Figure 1.7 Power output versus wind speed using difference control	8
Figure 1.8 LSWT blade and wake model	12
Figure 1.9 Hybrid system methodology.....	14
Figure 2.1 Phase VI rotor blade geometry	18
Figure 2.2 Phase VI rotor twist angle distribution	19
Figure 2.3 Pressure tap locations	21
Figure 2.4 Reference points of the dynamic pressure.....	22
Figure 2.5 Aerodynamics force coefficients convention	23
Figure 3.6 Cell face index.....	33
Figure 3.7 Induced velocities and wind velocities at the boundary.....	37
Figure 3.8 k and ϵ near-wall value.....	42
Figure 4.9 Zones in DES methodology.....	58
Figure 5.1 Energ- extracting actuator disc and stream tube.....	69
Figure 5.2 Variation of C_P and C_T with axial induction factor	72

Figure 5.3 Rotor states	73
Figure 5.4 Flow field and force coefficients for phase VI rotor at low, intermediate, and high wind speeds.....	75
Figure 6.1 Convergence history	78
Figure 6.2 Sectional view of the computational C-grid at a typical radial location	80
Figure 6.3 Close-up of area near the surface	81
Figure 6.4 Effects of grid density on torque prediction	83
Figure 6.5 Effect of grid density on the power prediction error	84
Figure 6.6 Effects of turbulence models on low speed shaft torque.....	86
Figure 6.7 Effects of turbulence models on root flap bending moment	87
Figure 6.8 Effects of turbulence models on root edge bending moment	88
Figure 6.9 Sensitivity to the distance of the first point to the wall	89
Figure 6.10 Force coefficient topology.....	90
Figure 6.11 Effects of turbulence models on C_N distribution in the radial direction.....	91
Figure 6.12 Effects of turbulence models on C_T distribution in the radial direction.....	92
Figure 6.13 Effects of turbulence models on C_p distribution in the radial direction at 7 m/s	95
Figure 6.14 Effects of turbulence models on C_p distribution in the radial direction at 10 m/s.....	96
Figure 6.15 Effects of turbulence models on C_p distribution in the radial direction at 13 m/s.....	97
Figure 6.16 Effects of turbulence models on C_p distribution in the radial direction at 15 m/s.....	98

Figure 6.17 Effects of turbulence models on C_p distribution in the radial direction at 20 m/s.....	99
Figure 6.18 Effects of turbulence models on C_p distribution in the radial direction at 25 m/s.....	100
Figure 6.19 Effects of transition models on C_N distribution in the radial direction	103
Figure 6.20 Effects of transition models on C_T distribution in the radial direction.....	104
Figure 6.21 Effects of transition models on C_p distribution in the radial direction at 7 m/s	105
Figure 6.22 Effects of transition models on boundary layer thickness at 30% Chord and 7m/s.....	105
Figure A.1 Grid used in the turbulent models validation.....	110
Figure A.2 Grid used in the turbulent models validation.....	112
Figure A.3 Pressure Distribution for Angle of Attack = 0 degree, Fully Turbulent Calculation	113
Figure A.4 Pressure Distribution for Angle of Attack = 1.02 degree, Fully Turbulent Calculation	114
Figure A.5 Pressure Distribution for Angle of Attack = 5.13 degree, Fully Turbulent Calculation	114
Figure A.6 Pressure Distribution for Angle of Attack = 9.22 degree, Fully Turbulent Calculation	115
Figure A.7 Pressure Distribution for Angle of Attack = 14.24 degree, Fully Turbulent Calculation	115

Figure A.8 Pressure Distribution for Angle of Attack = 20.15 degree, Fully Turbulent Calculation	116
Figure A.9 Profile of Turbulence Viscosity at 5.13 degree on the suction surface at $\frac{3}{4}$ chord	116
Figure A.10 Lift Coefficients.....	118
Figure A.11 Drag Coefficients.....	119

NOMENCLATURE

a	Speed of sound
c	Chord length
C_D	Pressure drag force coefficient
C_L	Lift force coefficient
C_M	Pitching moment coefficient
C_N	Normal force coefficient
C_p	Pressure coefficient
C_T	Tangent force coefficient
d	Distant from the wall
e	Internal energy
\tilde{e}	Internal energy per unit mass
\bar{E}_I, \bar{E}_V	Inviscid and viscous flux
$\bar{F}_I, \bar{G}_I, \bar{H}_I$	Cartesian components of the inviscid flux vectors
$\bar{F}_V, \bar{G}_V, \bar{H}_V$	Cartesian components of the viscous flux vectors
f_{v1}	Damping function for Spalart-Allmaras model
I	Identity metric
J	Jacobian of transformation
k	Turbulent kinetic energy
K	Thermal conductivity
l	Mixing length

L, D, U	Lower, diagonal and upper block triangular matrix
L_R	Reference length
M	Mach number
M_{tip}	Tip Mach number
p	Pressure
P_{meas}	Measured pressured corrected for centrifugal force
Pr	Prandtl number
Pr_T	Turbulent Prandtl number
PTM	Damping function for transition model
\bar{q}	Vector of conserved flow variables
q_L, q_R	Left and right fluxes crossing a cell face
Q_{norm}	Dynamics pressure from 5-hole probe
r	Rotor radius
R	Gas constant
Re	Reynolds number
Re_{tip}	Tip Reynolds number
R_θ	Momentum thickness
R_x	Length Reynolds number
RHS	Shorthand notation for the terms on the right hand side for any equation
S	Surface control volume
S	Vorticity
T	Temperature

u, v, w	Cartesian components of velocity
U^+, U^-	Convection velocity used in upwind scheme
\tilde{V}	Deforming control volume
$\vec{V}_{\tilde{V}}$	Velocity vector on the control volume surface
\vec{V}_{grid}	Grid velocity
\vec{V}_{wind}	Wind velocity
$\vec{V}_{induced}$	Induced velocity
x, y, z	Cartesian coordinates
x_i	Normalized distance in chordwise direction
y_i	Normalized distance normal to chordwise direction
y^+	Non-dimensional normal distance

Greek Symbols

α	Angle of attack
β	Blade pitch angle
ε	Turbulent kinetic energy dissipation rate
γ	Ratio of specific heats
γ_{tr}	Chen and Tyson transition factor
ϕ	Local twist angle
κ	Von-Karman constant

ρ	Density
ρ_∞	Free stream density
Ω	Rotational speed
τ_{ij}	Shear stress tensor component
τ, ξ, η, ζ	Non-orthogonal body fitted coordinate system
μ	Molecular viscosity
μ_T	Turbulent viscosity
μ_∞	Free steam molecular viscosity
$\tilde{\nu}$	Undamped turbulent viscosity

Subscripts

FP	Associated with the full potential zone
i, j, k	Grid indices
NS	Associated with the Navier-Stokes zone
T	Turbulent
x, y, z, t, ξ, η, ζ, τ	Derivative with respect to
∞	Freestream condition

Superscripts

n, n+1	Time level
--------	------------

SUMMARY

Next generation horizontal-axis wind turbines (HAWTs) will operate at very high wind speeds. Existing engineering approaches for modeling the flow phenomena are based on blade element theory, and cannot adequately account for 3-D separated, unsteady flow effects. Therefore, researchers around the world are beginning to model these flows using first principles-based computational fluid dynamics (CFD) approaches.

In this study, an existing first principles-based Navier-Stokes approach is being enhanced to model HAWTs at high wind speeds. The enhancements include improved grid topology, implicit time-marching algorithms, and advanced turbulence models. The advanced turbulence models include the Spalart-Allmaras one-equation model, k - ϵ , k - ω and Shear Stress Transport (k - ω -SST) models. These models are also integrated with detached eddy simulation (DES) models.

Results are presented for a range of wind speeds, for a configuration termed National Renewable Energy Laboratory Phase VI rotor, tested at NASA Ames Research Center. Grid sensitivity studies are also presented. Additionally, effects of existing transition models on the predictions are assessed. Data presented include power/torque production, radial distribution of normal and tangential pressure forces, root bending moments, and surface pressure fields. Good agreement was obtained between the predictions and experiments for most of the conditions, particularly with the Spalart-Allmaras-DES model.

CHAPTER 1

INTRODUCTION

1.1 Background

Human beings have used wind energy in a variety of forms since ancient times. For example, sails have been used for sea travel since the pre-historic period. The use of wind energy also expanded on land in places such as Persia and China. The first documented design by the Persians for harnessing the wind dates to around 500 to 900 AD (figure 1.1), and was used for grinding grain and pumping water. The Persian panemone was not very efficient. The main force driving the turbine was drag, which is much less effective than lift. Furthermore, only half of the rotor cross section was used to generate power. The Chinese are also believed to have used wind energy for more than 2000 years. The oldest surviving documentation of the vertical-axis turbine, as used by the Chinese, dates back to 1219 A.D.

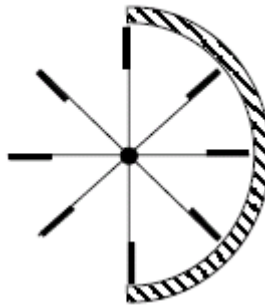


Figure 1.1 Persian panemone

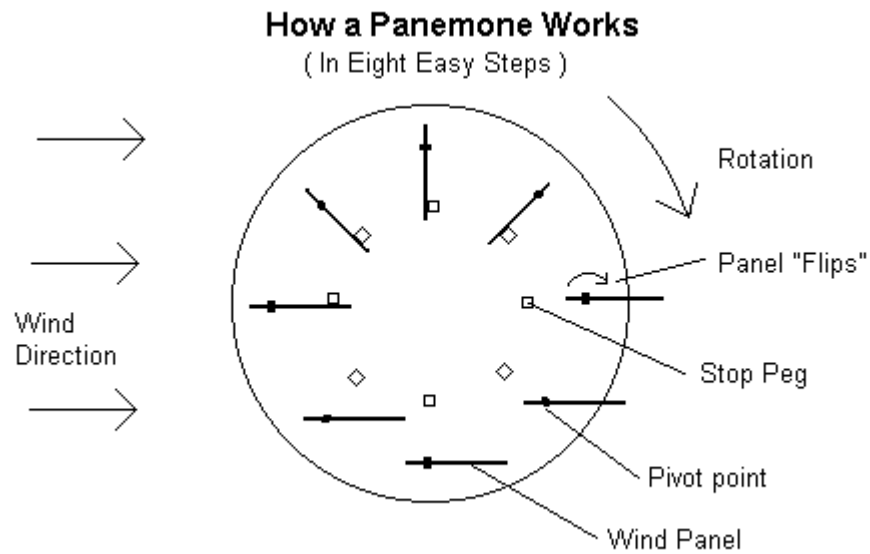


Figure 1.2 Modern-day panemone

With advances in wind turbine technology, vertical-axis wind turbines (VAWTs) evolved into more efficient forms. Modern VAWT designs easily rival modern horizontal-axis wind turbines (HAWTs) with several advantages. Unfortunately, the mechanical complexity of the VAWT prevents it from being widely used today.

In Europe, the first HAWT emerged circa 1270 AD. Interestingly, no evidence survives that can explain why the Europeans abandoned the VAWT plants and invented the new design. Some believe that it was the design of the water wheel, a type of horizontal-axis turbine, which might have inspired the change. Though the European

design used sails rather than airfoils, and relied on drag rather than lift effects, this approach was more efficient than the panemone because it could utilize the whole cross section of the rotor to extract energy from the wind. This design would eventually evolve into the classical Dutch windmill circa 1390 AD. Windmills remained the principal source of generated power in Europe until the emergence of the steam engine in the eighteenth century. Although many improvements were made in subsequent years, the basic design of the windmill did not change substantially for centuries.

With the ready availability and manageability of the steam engine after the industrial revolution, windmills were abandoned. Most large wind turbines were replaced by the more controllable steam engines. This trend continued for more than one hundred years, leaving small wind turbines only in rural areas. A few large wind turbines survived for practical uses such as pumping water. New large windmills were also constructed occasionally. However, their development was affected by the availability of cheaper fossil fuel engines.

Charles F. Brush built the first windmill designed to generate electricity in Cleveland, Ohio, in 1888 largely in response to the increased demand for electricity. The drag-driven 17 meter (m) diameter rotor produced only 12 kilowatts (kW) of direct current and was a primary source of energy for the next twenty years. It was also the first to use the step up gearbox to operate at low RPM.

In Denmark, Poul La Cour built the first wind turbine in 1891. This machine was the first to exploit advances in aerodynamics. Though it was more efficient than earlier machines, it still could not compete with the cheaper steam engines.

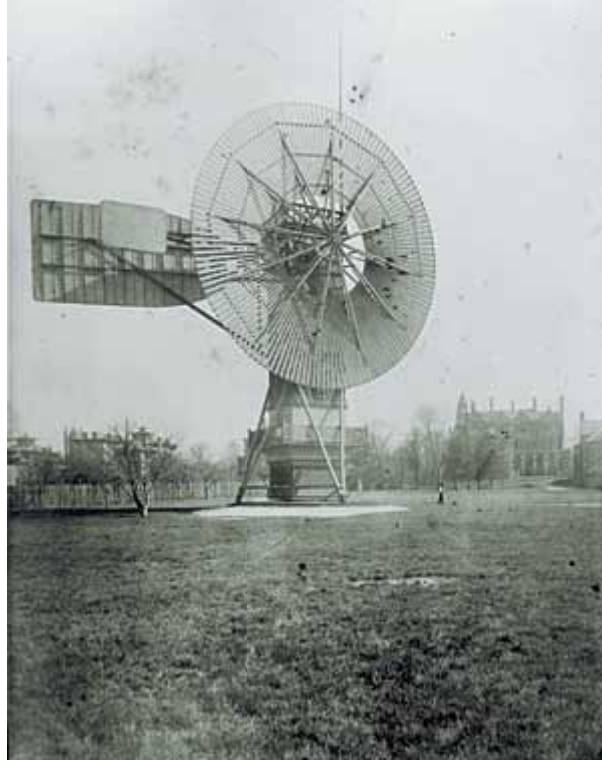


Figure 1.3 Bush Postmill, the first wind turbine, which attached to an electricity generator



Figure 1.4 Poul La Cour wind turbine

In order to for wind energy to become competitive, it would take the technological advancements in aerodynamics and material science of the twentieth century and the fuel crisis. Rapid advances in aerodynamics and material science during the latter part of the twentieth century and the oil crisis in the 1970s reignited the interest in wind energy. As time went on, the environmental concern both in the western US and around the world placed wind energy in a very competitive position compared to other renewable energy sources.

Modern wind turbines primarily rely on lift forces rather of drag to generate torque and power. This has considerably improved the efficiency with which energy may be extracted. For example, the modern 17 m diameter rotor can generate more than 70 kW, a huge improvement over the 12 kW power that the Bush Postmill produced. Improvements in material science have allowed the use of composite material-based rotors that are light, strong, and damage-tolerant. Use of lightweight materials has allowed the designers to increase the diameter of modern wind turbines.

1.2 The Future of Wind Energy

At the end of 2003, the installed capacity of wind turbines had risen to more than 40 gigawatts (GW). Over 80 terawatt hours (TW-hr) of electricity have been generated during that time. This figure still accounts for only about 0.5% of the total power generation in the world. Wind power generation capacity is rising at an average rate of about 19% per year and is projected to reach 95 GW by 2008.

Given the rising price of fossil fuels, stricter environmental regulations, and improvements in technology, this growth rate can be higher than projected. The rapid

growth in the generation of wind power has been further facilitated by supportive government policies and cost reductions brought about by technical progress and the economy of scale. Larger diameter rotors are now routinely used. In the year 2003, the average installed capacity of the wind turbine was 1.2 megawatts (MW). This is nearly double the average capacity of all previously installed wind turbines. Next generation wind turbines are expected to produce power in the 3 MW to 6 MW range.

The map below shows feasible sites in the United States for harvesting wind energy. Wind speeds range from 5 m/s in the east to 11 m/s on the west coast of Alaska. Most wind turbines, therefore, are designed for operation at these wind speeds.

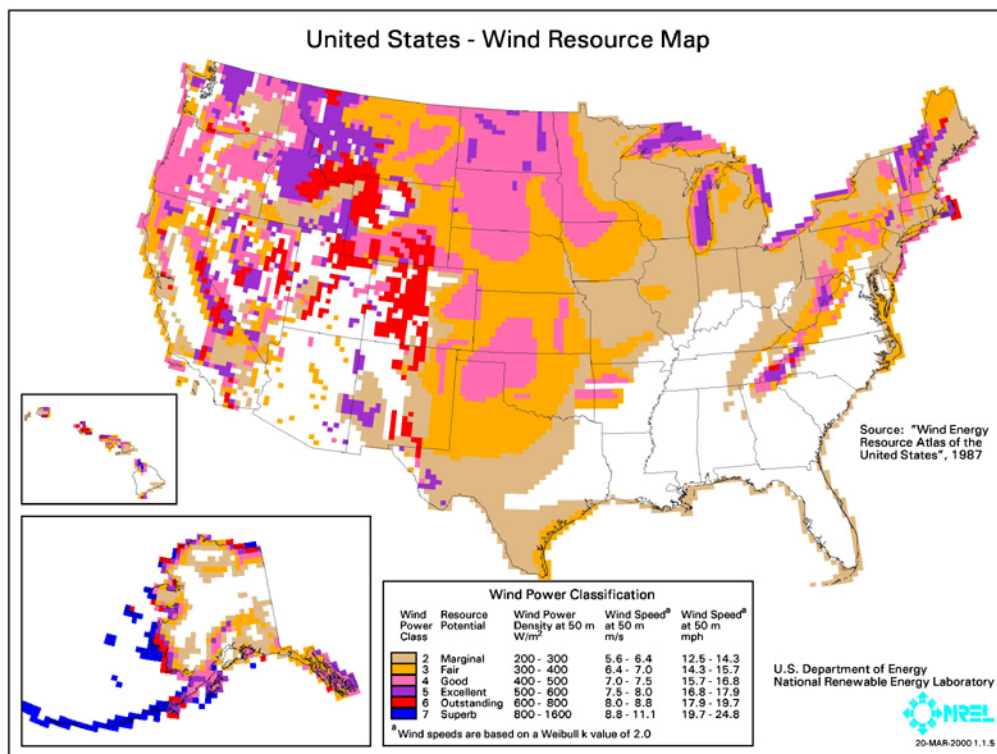


Figure 1.5 US wind energy map

While ready availability of wind power is beyond human control, it is possible to increase the power output through advanced design of rotor blades and by increasing the

swept area. The simplicity of the latter makes it the preferable choice for today's technology. Figure 1.6 shows the rapid increase of the rotor size (as measured by the rotor diameter) over the past two decades. Even a small increase in the diameter (~ by 40%) can increase the power output by a power of two.

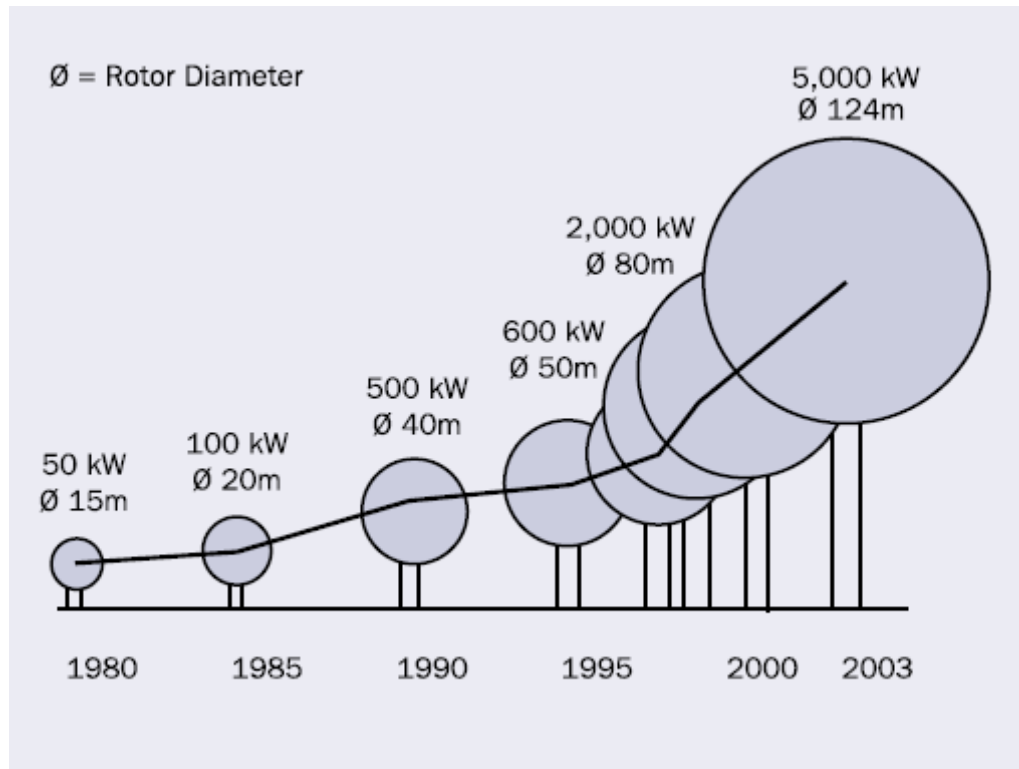


Figure 1.6 Growth of commercial wind turbine size

While large generators provide more power at better efficiency than the smaller ones, this increase places the following limitations on turbine operation. Normally, a power generator will operate efficiently at the design (or rated) output of power. At lower levels of power production, the generator will operate at a much lower efficiency. On the other hand, production of power at levels much higher than that the generator is designed for will cause damage to the machinery. A mechanism is therefore needed to regulate the

power extraction from the rotor so that the generator operates at its optimum conditions even as wind speed increases beyond the designed limit.

1.3 Power Regulation Methods

As illustrated in figure 1.7, power extracted from wind kinetic energy increases with wind speed. When wind speed reaches design conditions, which in most cases is the average wind speed at that location as shown in figure 1.4, the power extracted from the rotor will stop increasing and stabilize even as the wind speed increases. The power extraction from the rotor is matched with the rated power of the generator so that the wind turbine will operate at optimal efficiency.

There are two major approaches for achieving this goal. The first is to control the blade pitching angle. This method provides the best control over the power output of the rotor. Unfortunately, this method requires a very sophisticated control system that is expensive to operate and maintain in routine commercial use. For this reason, only a small number of pitch-regulated power regulators have been installed in the field.

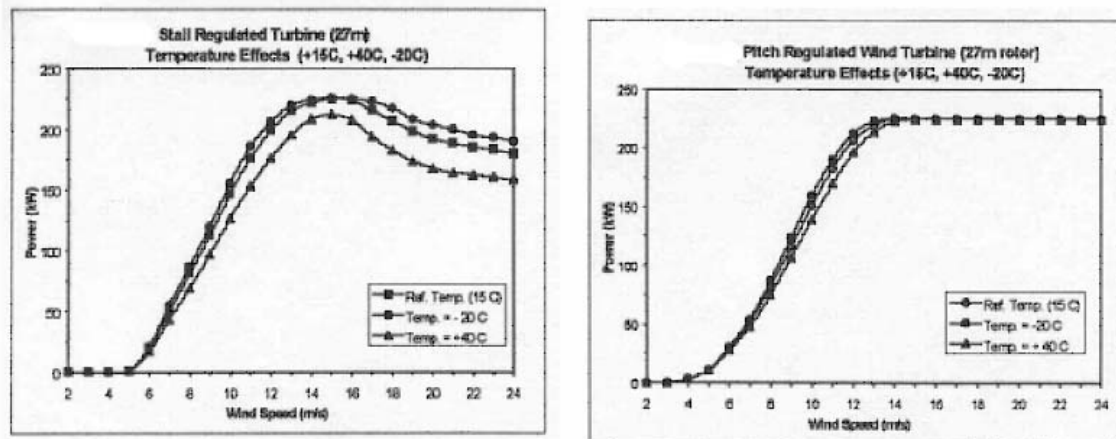


Figure 1.7 Power output versus wind speed using difference control with the effect of temperature (Information from Vestas Wind System A/S Denmark.)

Most modern wind turbines are stall-regulated, and rely on the aerodynamic design of rotors rather than complex control. These designs allow the turbine to maintain a constant power output at the rated power of the generator. The geometry of the blade is carefully designed so that the flow will partially stall when the rated power is reached. The drawback of this turbine type is shown in figure 1.6. Even with careful design, today's engineering methods are unable predict the proper power output as the pitch is changed.

However, the power output profile shown in figure 1.6 raises the problem of high aerodynamic loads. As the size of the turbine increases, the blades will be subjected to higher loads from their own weight, and from the airloads produced by the flow around the blades, tower, and nearby turbine structures. These loads arising from complex 3-D phenomena must be accurately predicted in order to design large rotors that are aerodynamically efficient, have the desired structural strength, and have an adequate fatigue life.

Much work has been done on the development of engineering approaches for modeling wind turbines. These methods use a table-look up of 2-D airfoil load characteristics and are coupled to structural analyses as mentioned by Buhl [1]. These methods, however, are not adequate for predicting accurate loads at high wind speeds where the flow is unsteady, three-dimensional, and stalled. The industries and researchers are therefore turning to the use of first principles-based modeling of the flow using computational fluid dynamics (CFD). The rapid advances in computational algorithms and the ready availability of high-speed computers and clusters have made CFD a tool that is complementary to traditional engineering approaches.

1.4 Survey of Available Methods for Aerodynamic Modeling of HAWTs

Section 1.4 reviews briefly methods for modeling horizontal axis wind turbines.

1.4.1 Blade Element Momentum Theory

The rotors found in current generation HAWT systems are designed using a combination of 2-D airfoil analysis and design tools (Tangler [2], Eppler [3], and Selig [4]), and combined blade element and momentum (BEM) theory (Glauert [5], Hansen [6], Laino [7]). A number of comprehensive computer codes using this methodology, such as Yawdyn [8], are currently available. In some of these analyses, unsteady flow effects are captured using unsteady potential flow theory and dynamic stall models (e.g., Leishman and Beddoes [9]). Buhl [10] has documented many of these BEM computer codes, which are maintained by the National Renewable Energy Laboratory (NREL).

While computationally efficient and highly useful, these methods are incapable of accurately modeling three-dimensional cross flows, tower shadow effects, tip relief effects, and sweep effects. These three-dimensional effects can alter the airloads, affect the fatigue life, and significantly influence the total cost of ownership of HAWT systems. In spite of these drawbacks, BEM is the most widely used method for design and analysis of HAWT systems. BEM's simplicity requires neither a complex procedure nor a sophisticated machine. Researchers are trying to increase the accuracy of combined blade element-momentum methods in the stall and post stall regime. Such studies (e.g., Tangler[11], Duque [12], [13]) were done by using advanced 2-D CFD methods combined with experiments to produce the airfoil look-up tables needed in BEM. The 2-

D stall characteristics are empirically modified so that the blade sections stall at a higher angle of attack to mimic 3-D stall. The complexity of 3-D effects makes this “stall delay” model inaccurate. A stall delay model might predict an accurate result at one span-wise station, but completely fail to predict the stall at another station. More sophisticated stall delay models are needed to reduce the time needed for computation.

1.4.2 Lifting Surface, Prescribed-Wake Code

In an attempt to better model the 3-D aerodynamic characteristics of the rotor, the Lifting Surface, Prescribed-Wake code (LSWT) was developed for NREL by Kocurek [14]. This method combined a lifting surface representation of the rotor blade with a model of the rotor wake. The wake model allows the trailing vortices shed by the blade in the vicinity of the blade tip to roll up. This results in an improvement over the 2-D methods. If the wake obstacle interactions are known, this method can be used for more complex flows, including tower shadow effects and non-axial flow effects. While this method models some of the important 3-D phenomena, the inviscid theory behind this method cannot predict stall. Moreover, the viscous effects are still not considered except through profile drag effects from a table-look up. Consequently, this method cannot handle the flow at stall and post stall.

This problem was solved by using the known C_N and C_T at stall occurrence to calibrate the strength of singularity on each panel. From these known parameters, the C_L , C_D , and angle of attack can be obtained, from which the tip vortex and root vortex strength can be estimated. This information from lifting surface methods have been used to improve BEM codes. Nevertheless, LSWT is referred to as a calibration tool for many

BEM codes before the stall regime. Beyond stall, many researchers use LSWT as a tool to convert C_N and C_{Tto} to C_l , C_d , and angle of attack.

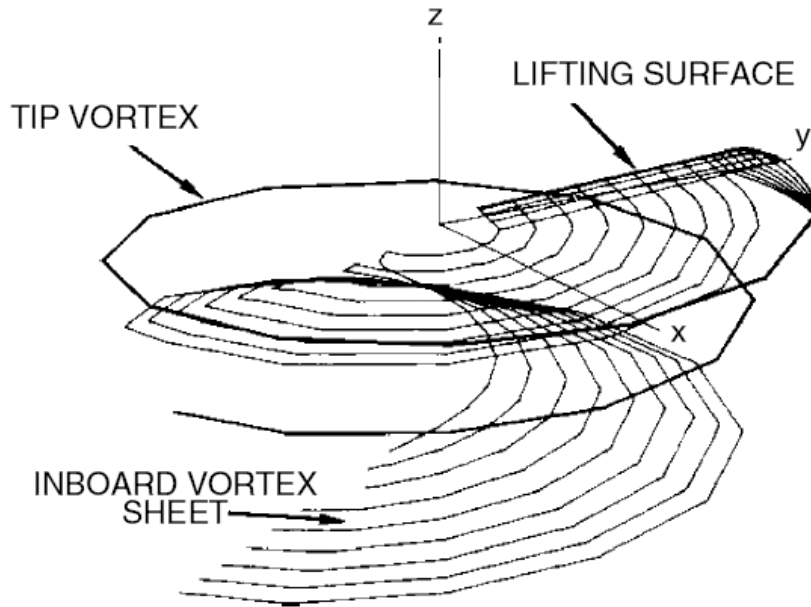


Figure 1.8 LSWT blade and wake model

An improved version of the LSWT method is found in CAMRAD II, a comprehensive rotorcraft analysis that also solves the potential flow equation. Instead of using the lifting surface, it uses a vortex lattice representation of the rotor coupled to a free wake model made of trailing and shed vortices. When the 2-D airloads data are in use, a stall delay model is needed.

1.4.3 Navier-Stokes Solvers

The Navier-Stokes method solves the flow-governing equations directly. Unlike the previous methods, it has the potential to predict the correct flow field without a prior knowledge of the airfoil load characteristics. This approach solves for the flow properties at the surface as well as the interior of the flow field and can give much more details of

the flow field than the other methods. The clear advantage of this procedure is its robustness—it can be used at all wind speeds with modification. However, this method also needs much more computational power, making it less suitable for design studies where a large number of design variables must be parametrically changed.

Full Navier-Stokes simulations of HAWT configurations have been completed by researchers both in the US and Europe. Using of experimental data for NREL the Phase II rotor, Duque [12], [13] compared the accuracy of BEM, vortex lattice, and Reynolds-Averaged Navier Stokes (RANS) methods. He found that though the BEM and VL predicted results more accurately than RANS, they were heavily dependent on the accuracy of the stall delay models. In Denmark, Sorensen [15] used an incompressible RANS method to predict performance of the same rotor. The results were in reasonable agreement with the experiment. His RANS simulations provided greater detail of flow around the blade than were available from the simpler approaches.

In 2000, the NREL invited several universities and research institutes to participate in a blind run competition. All participants were given the new wind turbine configuration (NREL Phase VI rotor) and asked to compute to the aerodynamic characteristics for a range of wind conditions and yaw angles. Further information about wind tunnel data can be found in the document by Hand [16]. In this blind run, the RANS simulations by Sorensen [17] correlated best with measurements. With the same methodology, Madsen [18] studied the effects of yaw on air loads. Other participants such as Duque [19] show comparatively good results using RANS. The performance predictions by Xu [20], were also in very good agreement with the experiment,

particularly at high wind speeds. Overall, the results from the blind run demonstrated the superiority of the RANS approaches over simpler engineering methods.

1.4.4 Hybrid Methodology

Though RANS is robust and more accurate compared to engineering approaches, it can be computationally costly. An alternative is a zonal approach, where RANS is used only where needed. This method increases the solution efficiency by dividing the flow field into three regimes: (a) a small viscous region surrounding the individual rotor blades where the Navier-Stokes equations are solved, (b) a potential flow region which carries the acoustic and pressure waves generated by the rotor to the far field, and (c) a Lagrangian scheme for capturing the tip vortices that leave the rotor and convected away from the rotor by the wind as shown below.

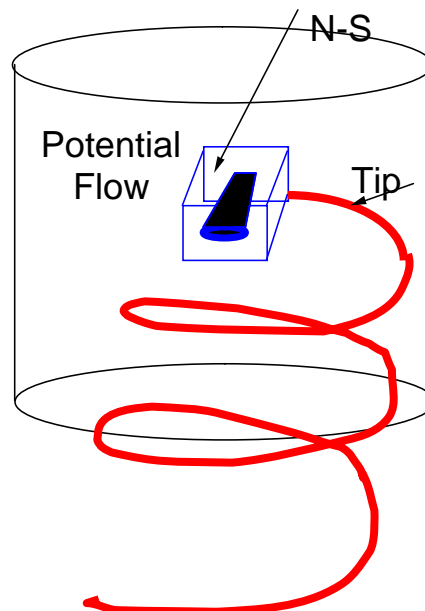


Figure 1.9 Hybrid system methodology

Moulton and colleagues [21] added the Navier-Stokes inner zone to the existing full-potential hover code, HELIX-I. Sankar, et. al., [22], [23], [24] used a similar idea by

coupling the unsteady full potential equation with the Navier-Stokes equations and predicted unsteady viscous transonic flow over an F-5 wing with good results. In this case, the methodology was proved accurate while reducing the computational time by half. Berezin [25] expanded the use of this method to rotors operating in high speed forward flight. Berezin used a comprehensive analysis (RDYNE) to compute the induced flow at the rotor disk, and also accounted for the elastic deformation of the blades, by coupling the aerodynamic analysis to a structural representation of the rotor.

The fixed and free-wake models were implemented into the methodology by Berkman [26] to reduce the convergence time, and to remove the dependence of the method on an external inflow model. This hybrid methodology was improved further by Yang [27] for use in forward flight—laying the groundwork for the simulations of wind turbines under yaw conditions. With support from NREL, Xu [28], [29], [30] applied this hybrid methodology to wind turbines. Though Xu's approach could accurately predict performance of the new wind turbine in the blind run comparison, several lessons were learned. The accuracy of performance prediction of stall-regulated wind turbines depends on the precise prediction of location and degree of transition on the suction surface. Further work on improved turbulence viscosity prediction is conducted by Benjanirat [31], [32]. He included the effects of inboard vortices on inflow, and concluded that the improved turbulence models are necessary for improved prediction of wind turbine performance at high wind conditions.

Tongchitpakdee [33] has recently extended the approaches given in Ref 32-33 to rotors operating in yaw, and has studied the effects of active devices (circulation control) and passive devices (Gurney flaps) on the power production.

1.5 Research Objectives and Scope

This research focuses on expanding an existing first-principles methodology described in Ref. [31] and [32] with advanced turbulence models, to understand the development of physical flow around wind turbines over a range of wind speeds. Several advanced turbulence and transition models are implemented and studied. The effects of modern two equation turbulence models on the prediction of separated flow are assessed. An advanced Detached Eddy Simulation (DES) is also investigated to evaluate whether it will improve the predictions at high wind speeds. A grid sensitivity study is also completed to provide an understanding of the impact of a grid density on the solution accuracy..

CHAPTER 2

NREL PHASE VI ROTOR

Over the past two decades, the National Renewable Energy Laboratory has developed and tested several wind turbine configurations. This chapter provides information about one of these configurations, called the phase VI rotor that has been extensively used in this study.

2.1 Background

Phase VI rotor is the name given to the latest development from the series of “combined experiments” conducted by NREL since 1987. The objective of these experiments was to bridge the gap between 2-D design environment and 3-D operation. The knowledge from each phase was used to understand the complexity of the physical flow around the blade and to improve the new rotor in subsequent phases. Table 2-1 provides a brief summary of some of the wind turbine rotors developed and tested by NREL.

Table 2.1 Previous NREL rotor models

	Phase II	Phase III	Phase IV	Phase V
Data collection dates	4/25/89–7/25/92	4/7/95–6/6/95	4/3/96–5/18/96 and 4/29/97–5/7/97	4/3/96–5/18/96 and 4/29/97–5/7/97
Blades / hub	untwisted / rigid	twisted / rigid	twisted / rigid	twisted / teeter
Number of blades	3	3	3	2

It should be noted that these field tests of these wind turbines were completed at a site in Colorado. Though the results were useful, the accuracy was questionable since many factors—including wind speed—could not be not controlled.

2.2 Phase VI Rotor

The phase VI rotor is a stall-regulated rotor designed by Giguère and Selig [34] under contract by NREL from March 1998 through March 1999. This 10 m diameter, stall-regulated turbine with full-span pitch control has a power rating of 20 kW. The phase VI rotor blade has linear taper and non-linear twist. It is exclusively made of S809 airfoil sections from root to tip. The phase VI rotor is the first in which a linear taper was specified so that the chord length at 80% span was 457 mm and 305 mm at the tip.

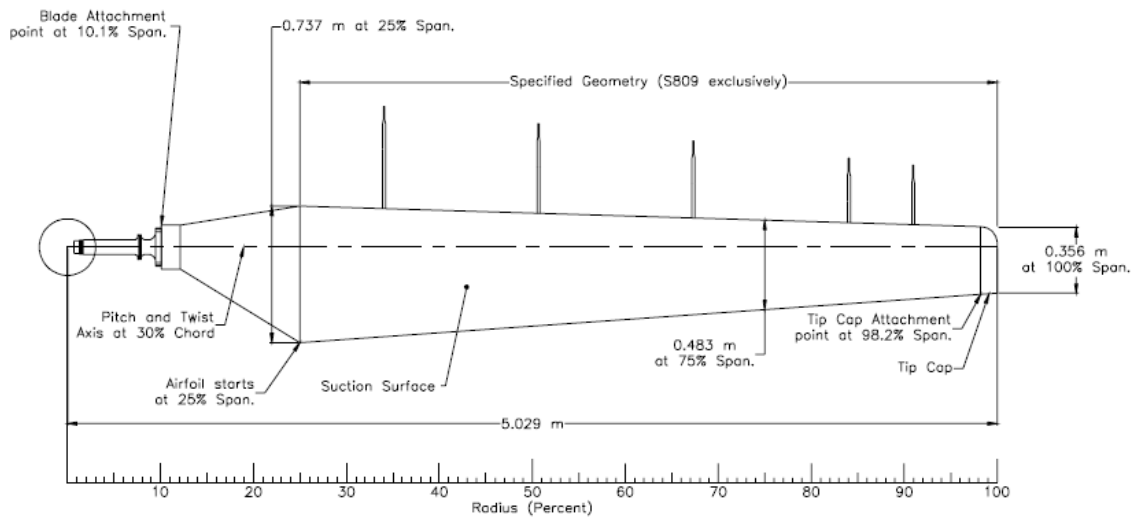


Figure 2.1 Phase VI rotor blade geometry

The non-linear twist angle variation is shown in figure 2.1, with the pitch angle set to zero at 75% span. The same planform was used in two- and three-blade configurations, both. When used in a two-blade configuration, the designers recommended that the span be increased to 11 m—about 10% longer than its three-blade counterpart—and operated at 78 rpm instead of 72 rpm.

In the wind tunnel tests to be discussed later, a two-bladed configuration with a 5 m radius and operating at 72 rpm was used. This blade is designed for constant-speed operation but should also run at variable speed.

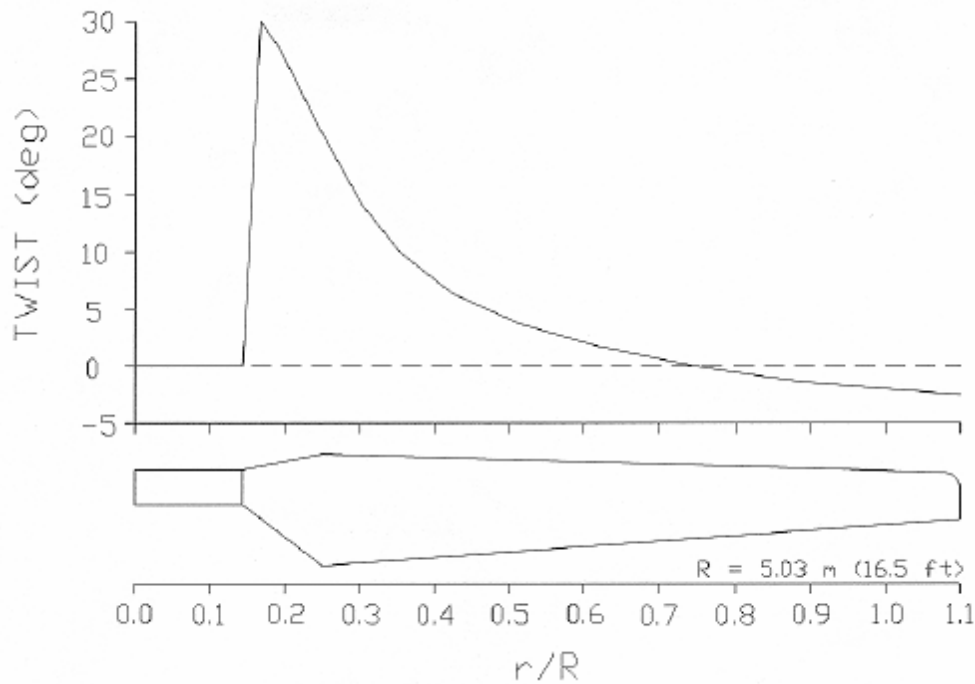


Figure 2.2 Phase VI rotor twist angle distribution

The S809 airfoil replaced the original Grumman airfoil since the phase V test in 1998. Airfoils, Inc. created this airfoil, the design of which features better power production and reduction of sensitivity to leading edge roughness. The S809 performance information is documented in a paper by Somer [35]. 2-D wind tunnel tests of this airfoil have been conducted at Delft University, Colorado State University, and Ohio State University.

2.3 Unsteady Aerodynamics Experiments

A full-scale wind tunnel test was completed in the 80 ft by 120 ft wind tunnel at NASA Ames Research Center in 1999 through 2000 [36]. The objective of this test was to investigate the effects of unsteady flow produced by the off-design condition and the obstacles near the wind turbine. This study was expected to provide insights that could

not be obtained from the existing design process using steady 2-D data. The full-scale equipment was used in a controlled environment. The basic information of the machine is shown below.

Table 2.2 NASA Ames Test Configuration

Number of Blades	2
Rotor Diameter	Varies: 10.058 m/9.886 m/11.064 m
Hub Height	12.192 m
Type of Rotor	Teetered/Rigid
Rotational Speed	71.63 rpm
Power Regulation	Stall
Rated Power	19.8 kW
Location of Rotor	Upwind/Downwind
Rotational Direction	CCW (viewed from upwind)

The testing was done in several test sequences to simulate the combinations of the effects of upwind/downwind operation, yaw, and using rigid or teetered hub.

The blade surface pressure distribution was measured by arrays of pressure sensors at several spanwise stations. Twenty-two taps were instrumented at five primary spanwise locations: 30%, 46.6%, 63.3%, 80%, and 95%. Furthermore, several pairs of pressure sensors were installed at 4% and 34% chords at several spanwise locations.

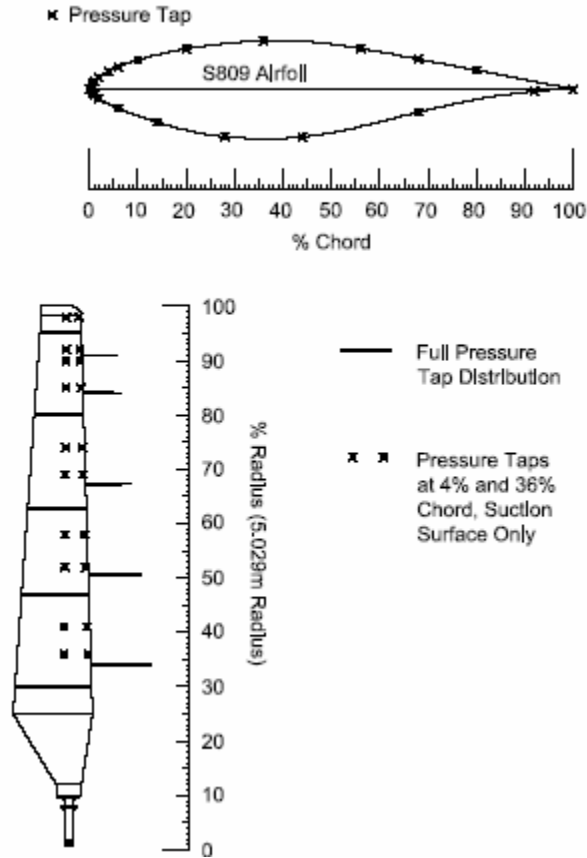
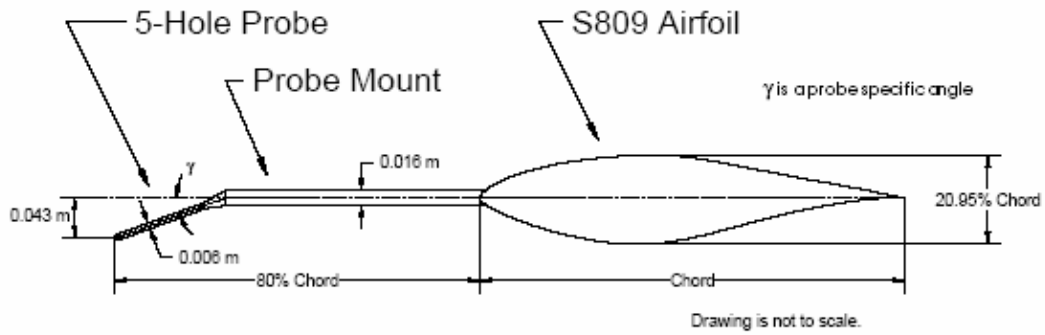


Figure 2.3 Pressure tap locations

Five-hole probes were installed at 34%, 51%, 67%, 84%, and 91% spans to measure the dynamic pressure and the local effective angles of attack. The probe's tip was located at 80% of the chord length upstream of the leading edge and about 20 degrees below the chord line. The measured dynamic pressure was used in the calculation of the pressure and force coefficients in the experiments.



**Figure 2.4 Reference points of the dynamic pressure
(Picture from Ref [36])**

2.3.1 Forces Coefficients

From both the blade surface pressure distribution and the dynamic pressure, the pressure coefficient may be calculated automatically by the system using the definition below.

$$C_p = \frac{P_{meas}}{Q_{norm}} \quad (2-1)$$

where

C_p is the pressure coefficient

P_{meas} is the measured gauge pressure corrected for centrifugal force, Pa

Q_{norm} is the dynamics pressure calculated from the five-hole probe, Pa

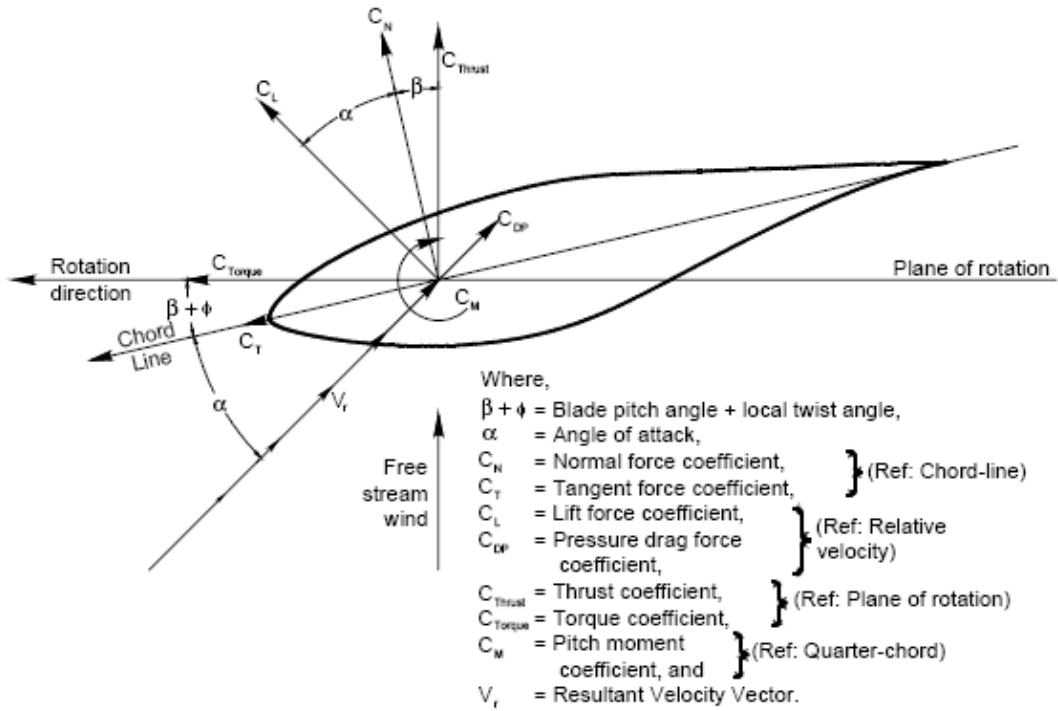


Figure 2.5 Aerodynamics force coefficients convention
(from D. Simms, et. al. [36])

Both normal force coefficients and tangential force coefficients are also calculated automatically by the system. The definition is provided below.

$$C_N = \sum_i \left(\frac{C_{p_{i+1}} + C_{p_i}}{2} \right) (x_{i+1} - x_i) \quad (2-2)$$

$$C_T = \sum_i \left(\frac{C_{p_{i+1}} + C_{p_i}}{2} \right) (y_{i+1} - y_i) \quad (2-3)$$

$$C_M = \sum_i \left[\left(\frac{C_{p_{i+1}} + C_{p_i}}{2} \right) \left[(x_{i+1} - x_i) \left(\frac{(x_{i+1} - x_i)}{2} + x_i - 0.25 \right) + (y_{i+1} - y_i) \left(\frac{(y_{i+1} - y_i)}{2} + y_i \right) \right] \right] \quad (2-4)$$

where

C_p is the pressure coefficient

x_i is the normalized distance in chord wise direction

y_i is the normalized distance normal to chord wise direction

Bending moments were measured using the strain gauges at the root of each blade. Torque was also measured by using strain gauges on the low-speed shaft. All were recorded in the database by NREL. However, they can also be estimated from the force coefficients.

Blade surface pressures, angle of attack, and inflow dynamic pressure at five span locations on one blade were carefully measured. Blade root bending moments, low-speed shaft-bending moments, and nacelle yaw moments were recorded, as well as blade tip and nacelle accelerations. Positional measurements, such as nacelle yaw, rotor azimuth, and blade pitch were included in the data. Experiments were undertaken at wind speeds ranging from 5 m/s to 25 m/s at several yaw angles, and in both upwind and downwind conditions including the effect of the tower.

The highly accurate measurements of the complex flow around the blade of the phase VI rotor make this configuration an excellent candidate for validating the CFD methodology.

CHAPTER 3

MATHEMATICAL FORMULATION

This study uses the computer code Windrotor, which is under continuous development at Georgia Institute of Technology. This code has been built from earlier studies and was originally used for modeling helicopter rotors and compressors. Sankar and Wake developed a version of this analysis for helicopter rotors [37]. The hybrid methodology was added by Xu, who studied wind turbine applications in 1998 [20]. As part of the present study, a number of algorithmic improvements have been made. In this chapter, the mathematical modeling behind the algorithm is described in detail.

3.1 Governing Equations

The Navier-Stokes equations describe the conservation of mass, momentum, and energy. The fluid in this study is air, for which the Newtonian fluid assumption is a valid approximation. In the present work, body forces, heat addition, and mass diffusion are all neglected. The unsteady 3-D RANS equations are solved in a body-fitted coordinate system that rotates with the turbine blade. The flow field is divided into a number of control volumes or cells. Over each of these cells, the governing equations may be expressed in integral form as follows:

$$\frac{d}{dt} \iiint_{\tilde{V}} \bar{q} d\tilde{V} + \iint_S (\bar{E}_I - q \bar{V}_{\tilde{V}}) \cdot \bar{n} dS = \iint_S \bar{E}_V \cdot \bar{n} dS \quad (3.1)$$

Here \tilde{V} is a deforming control volume, S is the surface of the control volume, $\bar{V}_{\tilde{V}}$ is the velocity of the control volume surfaces, and \bar{q} is the flow vector:

$$\bar{q} = \begin{Bmatrix} \rho \\ \rho u \\ \rho v \\ \rho w \\ e \end{Bmatrix} \quad (3.2)$$

with density, ρ ; momentum components in each principal direction ρu , ρv , and ρw ; and the total energy per unit volume, e . The quantity e is the summation of the internal energy ($\frac{p}{\gamma-1}$) and kinetic energy ($\frac{1}{2}\rho(u^2 + v^2 + w^2)$), where p is the static pressure. All velocity components above are in an inertial Cartesian frame. The vector q may be viewed as the state of the flow properties, averaged within the cell.

The quantities E_I and E_V are the inviscid and viscous flux, respectively, and defined as follows:

$$\begin{aligned} \bar{E}_I &= \bar{F}_I + \bar{G}_I + \bar{H}_I \\ \bar{E}_V &= \bar{F}_V + \bar{G}_V + \bar{H}_V \end{aligned} \quad (3.3)$$

A PDE form of the Navier-Stokes equations can be obtained by applying conservation principles to an infinitesimally small fluid element fixed in space. Under the additional assumption of no body forces, no external heat addition, and no mass diffusion, the 3-D Navier-Stokes equations may be written in the following compact vector form in an inertial Cartesian system:

$$\frac{\partial \bar{q}}{\partial t} + \frac{\partial \bar{F}_I}{\partial x} + \frac{\partial \bar{G}_I}{\partial y} + \frac{\partial \bar{H}_I}{\partial z} = \frac{\partial \bar{F}_V}{\partial x} + \frac{\partial \bar{G}_V}{\partial y} + \frac{\partial \bar{H}_V}{\partial z} \quad (3.4)$$

$$\bar{F}_I = \begin{Bmatrix} \rho \\ \rho u^2 + p \\ \rho uv \\ \rho uw \\ u(e+p) \end{Bmatrix}, \bar{G}_I = \begin{Bmatrix} \rho \\ \rho uv \\ \rho v^2 + p \\ \rho vw \\ v(e+p) \end{Bmatrix}, \bar{H}_I = \begin{Bmatrix} \rho \\ \rho uw \\ \rho vw \\ \rho w^2 + p \\ w(e+p) \end{Bmatrix} \quad (3.5)$$

$$\bar{F}_V = \begin{Bmatrix} 0 \\ \tau_{xx} \\ \tau_{yx} \\ \tau_{zx} \\ E_x \end{Bmatrix}, \bar{G}_V = \begin{Bmatrix} 0 \\ \tau_{xy} \\ \tau_{yy} \\ \tau_{zy} \\ E_y \end{Bmatrix}, \bar{H}_V = \begin{Bmatrix} 0 \\ \tau_{xz} \\ \tau_{yz} \\ \tau_{zz} \\ E_z \end{Bmatrix} \quad (3.6)$$

The pressure property p is related to the internal energy through:

$$\begin{aligned} p &= \rho RT \\ &= \rho \cdot (\gamma - 1) \cdot \tilde{e} \\ &\cong (\gamma - 1) \left[e - \frac{1}{2} \rho (u^2 + v^2 + w^2) \right] \end{aligned} \quad (3.7)$$

τ_{xx}, τ_{xy} etc. are the components of the stress tensor, defined using Stokes relations and the

Boussinesq hypothesis:

$$\left. \begin{aligned} \tau_{xx} &= (\lambda + 2\mu)u_x + \lambda v_y + \lambda w_z \\ \tau_{xy} &= \mu(u_y + v_x) \\ \tau_{xz} &= \mu(u_z + w_x) \\ \tau_{yy} &= \lambda u_x + \mu(\lambda + 2\mu)v_y + \lambda w_z \\ \tau_{yz} &= \mu(v_z + w_y) \\ \tau_{zz} &= \lambda u_x + \lambda v_y + (\lambda + 2\mu)w_z \end{aligned} \right\} \quad (3.8)$$

$$\begin{aligned}
E_x &= u\tau_{xx} + v\tau_{xy} + w\tau_{xz} + K \frac{\partial}{\partial x}(T) \\
E_y &= u\tau_{xy} + v\tau_{yy} + w\tau_{yz} + K \frac{\partial}{\partial y}(T) \\
E_z &= u\tau_{xz} + v\tau_{yz} + w\tau_{zz} + K \frac{\partial}{\partial z}(T)
\end{aligned} \tag{3.9}$$

By using the Stokes hypothesis, the value λ can be eliminated from the equation with this relationship:

$$\lambda = -\frac{2}{3}\mu \tag{3.10}$$

The quantity μ is the molecular viscosity coefficient. In turbulent flows, this viscosity is augmented with the addition of a “turbulent viscosity,” μ_T . The molecular viscosity μ is a property of the fluid, so it can be treated as a constant if the temperature is not changing significantly. In this study, Sutherland’s Law is used to estimate laminar viscosity. The details of this estimation will be described in the next chapter.

Likewise, K is the thermal conductivity and is the sum of molecular and effective conductivity. It is defined as:

$$K = \frac{C_p \mu}{Pr} + \frac{C_p \mu_T}{Pr_T} \tag{3.11}$$

Here, Pr is the Prandtl number (≈ 0.72) and Pr_T is the turbulent Prandtl number (≈ 0.80).

3.1.1 Non-Dimensionalization of Governing Equations

In the present work, all simulations are done in a non-dimensional form. The non-dimensionalizing parameters are:

L_R : Reference length [chord of the rotor blade at 75% station (radius) in this study]

a_∞ : Free stream speed of sound

ρ_∞ : Free stream fluid density

μ_∞ : Molecular viscosity of fluid

$$\begin{aligned}
 x^* &= \frac{x}{L_R} & u^* &= \frac{u}{a_\infty} & t^* &= \frac{ta_\infty}{L_R} & \mu^* &= \frac{\mu}{\mu_\infty} & \varepsilon^* &= \frac{\mu_\infty \omega}{\rho_\infty a_\infty^4} \\
 y^* &= \frac{y}{L_R} & v^* &= \frac{v}{a_\infty} & \rho^* &= \frac{\rho}{\rho_\infty} & k^* &= \frac{k}{a_\infty^2} \\
 z^* &= \frac{z}{L_R} & w^* &= \frac{w}{a_\infty} & p^* &= \frac{p}{\rho_\infty a_\infty^2} & \omega^* &= \frac{\mu_\infty \omega}{\rho_\infty a_\infty^2}
 \end{aligned}$$

The asterisk denotes a dimensionless variable. When this non-dimensionalization procedure is applied to equation (3.4), the non-dimensional state vector, inviscid and viscous fluxes take a form similar to equation (3.12)

$$\frac{\partial \bar{q}^*}{\partial t^*} + \frac{\partial \bar{F}_I}{\partial x^*} + \frac{\partial \bar{G}_I}{\partial y^*} + \frac{\partial \bar{H}_I}{\partial z^*} = \frac{M_{tip}}{\text{Re}_{tip}} \left[\frac{\partial \bar{F}_V}{\partial x^*} + \frac{\partial \bar{G}_V}{\partial y^*} + \frac{\partial \bar{H}_V}{\partial z^*} \right] \quad (3.12)$$

The only difference is the appearance of the tip Reynolds number and Mach number on the right-hand side of equation (3.12). These are defined as:

$$\text{Re}_{tip} = \frac{\rho_\infty \Omega R L_R}{\mu_\infty} \quad (3.13)$$

$$M_{tip} = \frac{\Omega R}{a_\infty} \quad (3.14)$$

where Ω is the angular velocity of the blade and R is the blade radius. Hereafter, for the sake of readability, the asterisk denoting non-dimensional quantities will be dropped.

3.1.2 Governing Equations in Generalized Coordinates

The governing equation may be re-written in any coordinate system. In many cases, a body-fitted coordinate system is used. The transformation linking the physical coordinate system (x, y, z, t) and the non-orthogonal body-fitted coordinate system (ξ, η, ζ, τ) may be formally expressed as follows:

$$\begin{aligned}\tau &= \tau(t) \\ \xi &= \xi(x, y, z, t) \\ \eta &= \eta(x, y, z, t) \\ \zeta &= \zeta(x, y, z, t)\end{aligned}\tag{3.15}$$

In this case, a C-H grid topology is used, and the above equation may be thought of as a mapping of the (x, y, z) coordinates of the grid in the C-H grid with a uniformly spaced Cartesian coordinate system (ξ, η, ζ) , where ξ, η and ζ represent the three curvilinear coordinate directions along the chordwise, spanwise and normal direction of the rotor respectively. The symbol τ represents the time. It differs from the symbol “ t ” as follows: a derivative with respect to t is taken holding x, y , and z fixed, whereas a derivative with respect to τ is taken holding ξ, η , and ζ fixed.

The conversion between Cartesian to curvilinear coordinates uses the chain rule of differentiation. The transformed equation can be rewritten in the generalized curvilinear coordinate system as:

$$\frac{\partial \bar{q}}{\partial \tau} + \frac{\partial \bar{F}_I}{\partial \xi} + \frac{\partial \bar{G}_I}{\partial \eta} + \frac{\partial \bar{H}_I}{\partial \zeta} = \frac{M_{tip}}{\text{Re}_{tip}} \left[\frac{\partial \bar{F}_V}{\partial \xi} + \frac{\partial \bar{G}_V}{\partial \eta} + \frac{\partial \bar{H}_V}{\partial \zeta} \right]\tag{3.16}$$

As in the original equations, \bar{q} contains the conserved flow variables. Here, \bar{E}_I and \bar{E}_V are the transformed inviscid flux vectors and transformed viscous flux

vectors, respectively. The relations of these general domain flux vectors and their physical domain counterparts are given below.

$$\begin{aligned}
\bar{\bar{q}} &= \frac{\bar{q}}{J} \\
\bar{\bar{F}}_I &= \frac{1}{J}(\bar{F}_I \xi_x + \bar{G}_I \xi_y + \bar{H}_I \xi_z + \bar{q} \xi_t) \\
\bar{\bar{G}}_I &= \frac{1}{J}(\bar{F}_I \eta_x + \bar{G}_I \eta_y + \bar{H}_I \eta_z + \bar{q} \xi_t) \\
\bar{\bar{H}}_I &= \frac{1}{J}(\bar{F}_I \zeta_x + \bar{G}_I \zeta_y + \bar{H}_I \zeta_z + \bar{q} \xi_t) \\
\bar{\bar{F}}_V &= \frac{1}{J}(\bar{F}_V \xi_x + \bar{G}_V \xi_y + \bar{H}_V \xi_z + \bar{q} \xi_t) \\
\bar{\bar{G}}_V &= \frac{1}{J}(\bar{F}_V \eta_x + \bar{G}_V \eta_y + \bar{H}_V \eta_z + \bar{q} \xi_t) \\
\bar{\bar{H}}_V &= \frac{1}{J}(\bar{F}_V \zeta_x + \bar{G}_V \zeta_y + \bar{H}_V \zeta_z + \bar{q} \xi_t)
\end{aligned} \tag{3.17}$$

where J is the Jacobian of the transformation given by:

$$\begin{aligned}
J &= \frac{\partial(\xi, \eta, \zeta)}{\partial(x, y, z)} \\
&= \begin{vmatrix} \xi_x & \xi_y & \xi_z \\ \eta_x & \eta_y & \eta_z \\ \zeta_x & \zeta_y & \zeta_z \end{vmatrix} \\
&= \frac{1}{x_\xi (y_\eta z_\zeta - y_\zeta z_\eta) + x_\eta (y_\zeta z_\xi - y_\xi z_\zeta) + x_\zeta (y_\xi z_\eta - y_\eta z_\xi)}
\end{aligned} \tag{3.18}$$

All metrics appearing in the expressions for the Jacobian and the time metrics are calculated by:

$$\begin{aligned}
\xi_x &= J(y_\eta z_\zeta - y_\zeta z_\eta) & \eta_x &= -J(y_\xi z_\zeta - y_\zeta z_\xi) & \zeta_x &= J(y_\xi z_\eta - y_\eta z_\xi) \\
\xi_y &= -J(x_\eta z_\zeta - x_\zeta z_\eta) & \eta_y &= J(x_\xi z_\zeta - x_\zeta z_\xi) & \zeta_y &= -J(x_\xi z_\eta - x_\eta z_\xi) \\
\xi_z &= J(x_\eta y_\zeta - y_\zeta x_\eta) & \eta_z &= -J(x_\xi y_\zeta - x_\zeta y_\xi) & \zeta_z &= J(x_\xi y_\eta - y_\eta x_\xi)
\end{aligned} \tag{3.19}$$

$$\xi_t = -x_\tau \xi_x - y_\tau \xi_y - z_\tau \xi_z \quad \eta_t = -x_\tau \eta_x - y_\tau \eta_y - z_\tau \eta_z \quad \zeta_t = -x_\tau \zeta_x - y_\tau \zeta_y - z_\tau \zeta_z$$

where x_τ , y_τ , and z_τ represent the grid velocity components. The component of equation

3.17 can then be rewritten in vector form as:

$$\begin{aligned} \bar{\vec{q}} &= \frac{1}{J} \begin{Bmatrix} \rho \\ \rho u \\ \rho v \\ \rho w \\ e \end{Bmatrix} \\ \bar{\vec{F}}_I &= \frac{1}{J} \begin{Bmatrix} \rho U \\ \rho u U + \xi_x p \\ \rho v U + \xi_y p \\ \rho w U + \xi_z p \\ U(e+p) - \xi_t p \end{Bmatrix}, \bar{\vec{G}}_I = \frac{1}{J} \begin{Bmatrix} \rho V \\ \rho u V + \eta_x p \\ \rho v V + \eta_y p \\ \rho w V + \eta_z p \\ V(e+p) - \eta_t p \end{Bmatrix}, \bar{\vec{H}}_I = \frac{1}{J} \begin{Bmatrix} \rho W \\ \rho u W + \eta_x p \\ \rho v W + \eta_y p \\ \rho w W + \eta_z p \\ W(e+p) - \eta_t p \end{Bmatrix} \quad (3.20) \\ \bar{\vec{F}}_V &= \frac{1}{J} \begin{Bmatrix} 0 \\ \xi_x \tau_{xx} + \xi_y \tau_{xy} + \xi_z \tau_{xz} \\ \xi_x \tau_{yx} + \xi_y \tau_{yy} + \xi_z \tau_{yz} \\ \xi_x \tau_{zx} + \xi_y \tau_{zy} + \xi_z \tau_{zz} \\ \xi_x R + \xi_y S + \xi_z T \end{Bmatrix}, \\ \bar{\vec{G}}_V &= \frac{1}{J} \begin{Bmatrix} 0 \\ \eta_x \tau_{xx} + \eta_y \tau_{xy} + \eta_z \tau_{xz} \\ \eta_x \tau_{yx} + \eta_y \tau_{yy} + \eta_z \tau_{yz} \\ \eta_x \tau_{zx} + \eta_y \tau_{zy} + \eta_z \tau_{zz} \\ \eta_x R + \eta_y S + \eta_z T \end{Bmatrix}, \\ \bar{\vec{H}}_V &= \frac{1}{J} \begin{Bmatrix} 0 \\ \zeta_x \tau_{xx} + \zeta_y \tau_{xy} + \zeta_z \tau_{xz} \\ \zeta_x \tau_{yx} + \zeta_y \tau_{yy} + \zeta_z \tau_{yz} \\ \zeta_x \tau_{zx} + \zeta_y \tau_{zy} + \zeta_z \tau_{zz} \\ \zeta_x R + \zeta_y S + \zeta_z T \end{Bmatrix} \end{aligned}$$

3.1.3 Numerical formulation

One can discretize either the differential equations form of the governing equation (3.16) or the integral form (3.1) to arrive at comparable algebraic equations. The integral

form of the governing equations was discretized as follows. Let (i, j, k) represent a control volume, whose six faces $(i \pm \frac{1}{2}, j \pm \frac{1}{2}, k \pm \frac{1}{2})$ are shown above. The discretized form of equation (2.1) becomes:

$$\begin{aligned} \frac{\partial(q \cdot Vol)}{\partial \tau} = & -(\bar{E}_{i+\frac{1}{2}} - \bar{E}_{i-\frac{1}{2}}) - (\bar{F}_{j+\frac{1}{2}} - \bar{F}_{j-\frac{1}{2}}) - (\bar{G}_{k+\frac{1}{2}} - \bar{G}_{k-\frac{1}{2}}) \\ & + (\bar{E}_{vi+\frac{1}{2}} - \bar{E}_{vi-\frac{1}{2}}) + (\bar{F}_{vj+\frac{1}{2}} - \bar{F}_{vj-\frac{1}{2}}) + (\bar{G}_{vk+\frac{1}{2}} - \bar{G}_{vk-\frac{1}{2}}) \end{aligned} \quad (3.21)$$

where $\bar{E}, \bar{F}, \bar{G}$ are the discretized forms of the inviscid flux shown in (2.1); the $\bar{E}_v, \bar{F}_v, \bar{G}_v$ are the viscous counterparts. The inviscid flux \bar{E} is given by:

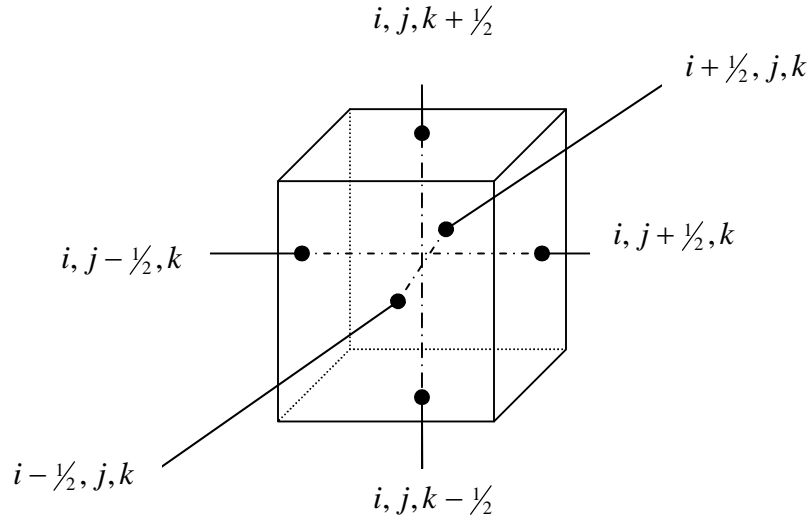


Figure 3.6 Cell face index

$$\bar{E}_{i+\frac{1}{2}} = \left. \begin{array}{l} \rho(\vec{V} - \vec{V}_{Grid}) \cdot \bar{n} \Delta S \\ \rho u(\vec{V} - \vec{V}_{Grid}) \cdot \bar{n} \Delta S + p \cdot \vec{i} \cdot \bar{n} \Delta S \\ \rho v(\vec{V} - \vec{V}_{Grid}) \cdot \bar{n} \Delta S + p \cdot \vec{j} \cdot \bar{n} \Delta S \\ \rho w(\vec{V} - \vec{V}_{Grid}) \cdot \bar{n} \Delta S + p \cdot \vec{k} \cdot \bar{n} \Delta S \\ \rho(\vec{V} - \vec{V}_{Grid}) \cdot \bar{n} \left(C_v + \frac{u^2 + v^2 + w^2}{2} \right) + p \cdot \vec{V} \cdot \bar{n} \Delta S \end{array} \right\}_{i+\frac{1}{2},j,k} \quad (3.22)$$

This flux may be computed in many ways. In symmetric finite-volume schemes (e.g., Jameson-Turkel-Schmidt Schemes), the properties at half points are computed using simple average $\frac{(\rho_i + \rho_{i+1})}{2}$, etc.

In modern upwind schemes, the fluxes account for the jumps in flow properties across acoustic, vortical, and entropy waves, and also take into consideration the direction of propagation (upwind versus downwind) these waves. At each time step, a fictitious diaphragm separating the fluid states and the left and right sides of a cell face is broken, giving rise to these waves. These waves are similar to those generated in a 1-D Riemann (shock tube) problem for which exact solutions are available. In the present work, Roe's approximate Riemann solver was used. \bar{E} was written as:

$$\bar{E} = \frac{\bar{E}(q_L) + \bar{E}(q_R)}{2} - \left| \frac{\partial \bar{E}}{\partial q} \right| (q_R - q_L) \quad (3.23)$$

where q_R and q_L are values of flow property vector q at $i + \frac{1}{2}$, which is appropriately interpolated from values stored at the nodes $i, i \pm 1, i \pm 2$ etc. In this work, a third order MUSCL interpolation has been used. In smooth regions:

$$\begin{aligned}
q_L|_{i+\frac{1}{2}} &= q_i + \frac{1}{3}(q_{i+1} - q_i) + \frac{1}{6}(q_i - q_{i-1}) \\
q_R|_{i-\frac{1}{2}} &= q_{i+1} - \frac{1}{3}(q_{i+1} - q_i) - \frac{1}{6}(q_{i+2} - q_{i-1})
\end{aligned}
\tag{3.24}$$

High order interpolation will give spurious oscillations, and limiters are used that drop the orders of interpolation to first order (e.g., $q_L = q_i$, $q_R = q_{i+1}$). In the low speed flow applications of this work, no such limiters were necessary.

$\bar{E}_v, \bar{F}_v, \bar{G}_v$, etc. were computed using standard symmetric schemes. The reader is referred to Xu [20] for detail.

3.2 Tip and Root Vortices Modeling

The Navier-Stokes solver captures the near-wake effects. Outside of the Navier-Stokes domain, the tip and root vortices are modeled in a Lagrangean fashion. In the present analysis, either a prescribed-wake or a free-wake model may be used. However, only the prescribed-wake model has been extensively used to date. With the prescribed-wake option, the user can choose to either use the classical-wake model or the Kocurek and Tangler-wake model [38] to describe the (x,y,z) coordinates of the tip and root vortices as a function of vortex wake age, and other global parameters (e.g. wind speed and disk loading or thrust coefficient).

The effect of the modeled wake is fed back to the Navier-Stokes domain using the Biot-Savart law. The induced velocities are used as boundary conditions.

3.3 Time Marching Algorithm

The discretized form of equation (2.1) may be written in semi-discrete form as:

$$\frac{\partial(q \cdot Vol)}{\partial \tau} = -\delta_{\xi} \bar{E} - \delta_{\eta} \bar{F} - \delta_{\zeta} \bar{G} + \delta_{\xi} \bar{E}_v + \delta_{\eta} \bar{F}_v + \delta_{\zeta} \bar{G}_v \quad (3.25)$$

where $\delta_{\xi} \bar{E} = \bar{E}_{i+\frac{1}{2},j,k} - \bar{E}_{i-\frac{1}{2},j,k}$, etc discussed earlier.

These equations may be integrated using a variety of approaches—explicit methods, implicit non-iterative methods and implicit iterative methods. The implicit schemes (iterative or non-iterative) are favored because of their superior temporal stability characteristics. These schemes may be formally written as:

$$\bar{\delta}_{\tau}(q \cdot Vol) = R^{n+1} \Big|_{i,j,k} \quad (3.26)$$

where R is the right side of equation (2.1), also called the residual. In steady state applications (e.g., axial flow conditions at low wind speeds), the solution converges to a steady state that is independent of the time step size. Because the present approach is designed for use in steady and unsteady flow conditions (e.g., high wind speeds, yawed flow), all the calculations were done in a time accurate mode.

The starting point of this effort was a three-factor ADI scheme for solving equations (2.20). Details of this scheme are given in Xu [20]. In the present study, the ADI scheme was replaced by a more robust two-factor LU scheme that will be discussed later.

3.4 Initial Conditions

The following initial values were used in the calculation:

$$\begin{aligned} \rho &= \rho_{\infty} \\ u &= 0 \\ v &= 0 \\ w &= 0 \\ p &= p_{\infty} \\ T &= T_{\infty} \end{aligned} \quad (3.27)$$

3.5 Boundary Conditions

At all solid boundaries, the no slip condition was applied:

$$\vec{V} = \vec{V}_{grid} \quad (3.28)$$

where \vec{V}_{grid} is the velocity of the blade as seen in an inertial coordinate system (i.e. a stationary observer). The surface was assumed adiabatic. Thus:

$$\frac{\partial T}{\partial n} = 0 \quad (3.29)$$

It is also assumed that:

$$\frac{\partial p}{\partial n} = 0 \quad (3.30)$$

At the in flow boundaries the velocities were prescribed as:

$$\vec{V} = \vec{V}_{wind} + \vec{V}_{induced} \quad (3.31)$$

where $\vec{V}_{induced}$ represents induced velocity from the all the tip and root vortices over the “reference” blade. The details of how $\vec{V}_{induced}$ is computed are discussed later.

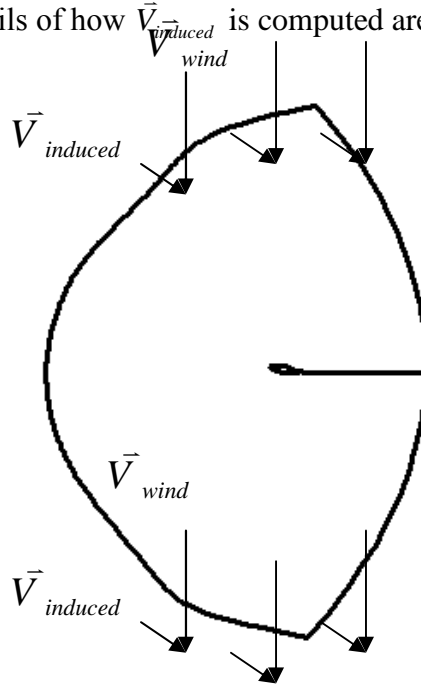


Figure 3.7 Induced velocities and wind velocities at the boundary

At the downstream boundary, where the wake from the blade leaves the grid, pressure was specified (equal to p_∞) and all other quantities (density, velocities) were extrapolated.

The properties at the cut were interpolated from the values at the points above and below the cut.

3.6 Turbulence Models

As part of this study, several turbulence models were implemented and are available in the Windrotor code. Those new turbulence models are described in the next chapters. Older turbulence models available in the analysis (e.g. the Baldwin-Lomax model) were also rewritten to improve their efficiency and improve the readability of the code. Many new features of FORTRAN 95 are also used to improve the computational speed and reduce memory requirements.

3.6.1 Baldwin-Lomax Model

The Baldwin-Lomax model [39] is the baseline zero-equation model in the Windrotor code. This is an equilibrium eddy viscosity model is a variant of the classical Cebeci-Smith model, and works well for attached flows. However, it is known that the eddy viscosity is out of equilibrium when the flow is separated. The accuracy of this model is therefore doubtful. Even though the model seems to yield reasonable results when used in some separate flow calculations, no attempt was made to assess this model, due to the non-equilibrium nature of the turbulent flows considered here.

In Baldwin-Lomax model, as in all eddy viscosity models, the Reynolds stress tensor can be replaced with:

$$-\rho \overline{u'_i u'_j} = \mu_T \left(\frac{\partial u_i}{\partial x_j} + \frac{\partial u_j}{\partial x_i} \right) \quad (3.32)$$

The eddy viscosity is computed in the Baldwin-Lomax model with a two-layer method:

$$\begin{aligned} \mu_T &= \mu_{T,inner} \quad y \leq y_{crossover} \\ \mu_T &= \mu_{T,outer} \quad y > y_{crossover} \end{aligned}$$

Here $y_{crossover}$ is the location in the shear layer where $\mu_{T,inner}$ exceeds $\mu_{T,outer}$ as one marches away from the wall.

In the inner layer close the wall, the dimensional eddy viscosity μ_T is given by:

$$(\mu_T)_{innerlayer} = \rho l_m^2 |\omega| \quad (3.33)$$

The μ_T used in the Windrotor code is non-dimensionalized using the reference values in

3.1.1.1. The non-dimensional value of this turbulence viscosity coefficient is:

$$(\mu_T)_{innerlayer} = \rho l_m^{*2} |\omega^*| \left(\frac{Re_{tip}}{M_{tip}} \right) \quad (3.34)$$

Recall the use of the asterisks to distinguish the non-dimensional variables from their dimensional counterparts. Here $|\omega|$ is the magnitude of vorticity in Cartesian coordinate system defined (with the asterisks suppressed for improved readability) as:

$$|\omega| = \sqrt{\left(\frac{\partial w}{\partial y} - \frac{\partial v}{\partial z} \right)^2 + \left(\frac{\partial u}{\partial z} - \frac{\partial w}{\partial x} \right)^2 + \left(\frac{\partial v}{\partial x} - \frac{\partial u}{\partial y} \right)^2} \quad (3.35)$$

Here, l_m is the mixing length, given by:

$$l_m^* = ky^* [1 - \exp(-y^{*+} / 26)] \quad (3.36)$$

and k is the Von-Karman constant taken as 0.41. The non-dimensional distance y^+ (with the asterisk suppressed for improved readability) is given by:

$$y^+ = \frac{\sqrt{\rho \tau_w}}{\mu} y \quad (3.37)$$

The non-dimensional form of this equation is:

$$y^+ = \frac{\sqrt{\rho^* \tau_w^*}}{\mu^*} y^* \left(\frac{\text{Re}_{tip}}{M_{tip}} \right)^{\frac{1}{2}} \quad (3.38)$$

The quantity $\left(1 - \exp(-y^{*+} / 26)\right)$ is called the Van Driest damping factor.

In the outer layer, the eddy viscosity is calculated as:

$$(\mu_T)_{outlayer} = 0.0168(1.6) \rho F_{wake} F_{kleb} \quad (3.39)$$

where

$$F_{wake} = \min\left(y_{\max} F_{\max}, \frac{y_{\max} u_{dif}^2}{F_{\max}}\right) \quad (3.40)$$

and

$$u_{dif} = (\sqrt{u^2 + v^2 + w^2})_{\max} - (\sqrt{u^2 + v^2 + w^2})_{\min} \quad (3.41)$$

The second term in u_{dif} is taken to be zero, except in the wakes. F_{\max} is the maximum value of the following function, and y_{\max} is the distance from the solid wall (or a wake cut) at which F_{\max} occurs:

$$F(y) = y |\omega| [1 - \exp(-y^+ / 26)] \quad (3.42)$$

In the wakes, $\exp(-y^+ / 26)$ is set to zero. The Klebanoff intermittency correction is applied to smoothly reduce the eddy viscosity to zero in the far-field.

$$F_{kleb} = \left[1 + 5.5 \left(\frac{0.3y}{y_{\max}} \right)^6 \right]^{-1} \quad (3.43)$$

3.6.2 The k-ε Model

In the k-ε model, the eddy viscosity is evaluated in terms of the turbulent kinetic energy, k, and the dissipation rate, ε, as follows [40]:

$$v_T = C_\mu \frac{k^2}{\varepsilon} \quad (3.44)$$

The temporal and spatial evolution of k can be obtained from solving the turbulent kinetic energy transport equation:

$$\frac{\partial k}{\partial t} + U_j \frac{\partial k}{\partial x_j} = \tau_{ij} \frac{\partial U_i}{\partial x_j} - \varepsilon + \frac{\partial}{\partial x_j} \left[\left(\nu + \frac{v_T}{\sigma_k} \right) \frac{\partial k}{\partial x_j} \right] \quad (3.45)$$

where

$$\tau_{ij} = 2\nu_T S_{ij} - 2k\delta_{ij} \quad (3.46)$$

and S_{ij} is the strain rate.

The transport and diffusion of the dissipation rate ε is governed by:

$$\frac{\partial \varepsilon}{\partial t} + U_j \frac{\partial \varepsilon}{\partial x_j} = C_{\varepsilon 1} \frac{\varepsilon}{k} \tau_{ij} \frac{\partial U_i}{\partial x_j} - C_{\varepsilon 2} \frac{\varepsilon^2}{k} + \frac{\partial}{\partial x_j} \left[\left(\nu + \frac{v_T}{\sigma_\varepsilon} \right) \frac{\partial \varepsilon}{\partial x_j} \right] \quad (3.47)$$

The constants in the k-ε formulation are listed below.

$$C_{\varepsilon 1} = 1.44, C_{\varepsilon 2} = 1.92, C_\mu = 0.09, \sigma_k = 1.0, \sigma_\varepsilon = 1.3$$

These are the “classical” constants, and no attempts have been made to modify them to improve the correlation.

The k-ε model needs a special near-wall treatment due to its tendency to over-predict the dissipation rate close to the near-wall region. That causes a problem with over-prediction of shear stress in that region. The Gorski model [41] offers a solution to this problem by superseding the value of k and ε near the wall with an alternate analytical approximation. The value of k is curve fit to vary with y^3 , and ε is set to a constant near

the wall. This model provides good agreement with the experimental result, though there is no support for this curve fit from theory of turbulent flows.

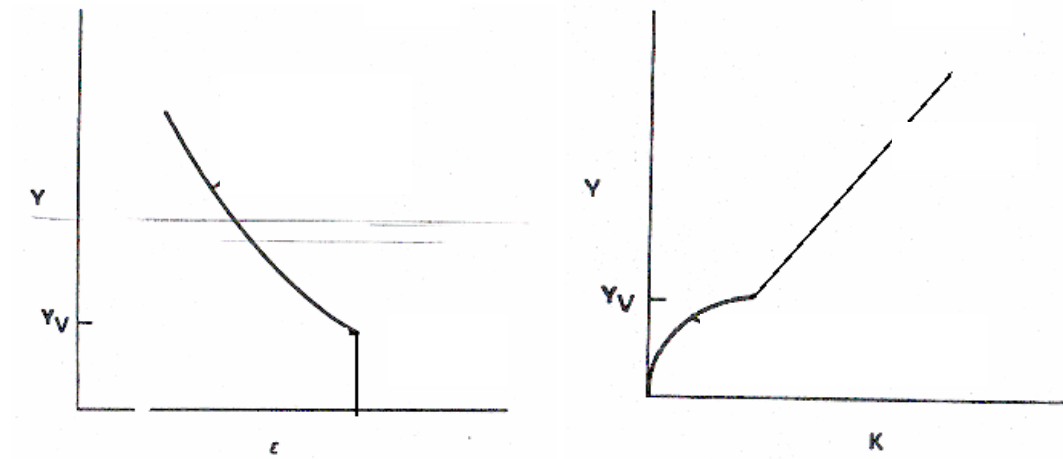


Figure 3.8 k and ϵ near-wall value

3.7 Transition Models

3.7.1 Eppler's Transition Model

Eppler's model was coded as a set of subroutines. The surface pressure distribution on the turbine blade is passed to this model, one radial location at a time. In the present work, the stream-wise growth of laminar boundary layer quantities (such as the momentum thickness, shape factor H , energy thickness δ_3 , and the factor $H_{32} = \delta_3/\theta$) are computed using an integral boundary layer technique. Transition is predicted to occur if the Reynolds number based on the momentum thickness becomes large so that:

$$\log\left(\frac{u_e \theta}{\nu}\right) > 18.4H_{32} - 21.74 - 0.34r \quad (3.48)$$

Here, “ r ” is a roughness factor. For highly polished surfaces, r may be taken to be zero. A value of 4 is used for insect contaminated surfaces, and a value of $r=6$ is considered a very rough surface.

It must be emphasized that Eppler’s model is intended for viscous flows where the boundary layer is steady, at least in a Reynolds time-averaged sense. Flow around wind turbines is highly unsteady, and the Eppler’s criterion will, at best, give only a first order estimate of the transition location.

This model also predicts that transition has occurred if the laminar boundary layer separates, causing a separation bubble near the leading edge of the rotor.

3.7.2 Michel’s Transition Model

In this model, transition is said to occur at the chord-wise location where the local Reynolds number based on the momentum thickness, R_θ , is related to the length of the Reynolds number, R_x , by:

$$R_\theta = 1.174 \left(1 + \frac{22400}{R_x} \right) R_x^{0.46} \quad (3.49)$$

In order to avoid an abrupt transition, Chen and Thyson [44] recommend that the eddy viscosity is multiplied by the factor:

$$\gamma_{tr} = 1 - \exp \left[-G(x - x_{tr}) \int_{x_{tr}}^x \frac{dx}{u_e} \right] \quad (3.50)$$

Upstream of the onset point of the transition region, γ_{tr} , is set to zero. The quantity G is computed from:

$$G = \left(\frac{3}{C^2} \right) \frac{u_e^3}{v^2} R_{x_{tr}}^{-1.34} \quad (3.51)$$

where the transition Reynolds number, $R_{x_{tr}} = \left(\frac{u_e x}{\nu} \right)_{tr}$

and

$$C^2 = 213(\log R_{x_{tr}} - 4.7323) \quad (3.52)$$

It should be noted that the quantity R_x is based on the local freestream velocity (the magnitude of the vector sum of wind speed and the blade velocity due to rotation $\vec{\Omega} \times \vec{r}$). Thus, for wind turbines:

$$R_x = \frac{u_\infty x}{\nu} = \frac{x u_{\infty local}}{c V_{tip}} c V_{tip} = \left(\frac{x}{c} \right) \left(\sqrt{\left(\frac{v_{Wind}}{V_{tip}} \right)^2 + \left(\frac{r}{R} \right)^2} \right) Re_{tip} \quad (3.53)$$

where r is the local radial distance from the hub, R is the tip radius, and x/c is the non-dimensional x coordinate. The Reynolds number based on the momentum thickness is also computed using the freestream velocity, not the boundary layer edge velocity.

In the present work, the actual quantity γ_{tr} was computed as follows:

$$\begin{aligned} \gamma_{tr} &= 1 - \exp \left[-G(x - x_{tr}) \int_{x_{tr}}^x \frac{dx}{u_e} \right] \\ &= 1 - \exp \left\{ \left[- \left(\frac{3}{C^2} \right) R_{x_{tr}}^{-1.34} \left(\frac{u_e}{u_{\infty local}} \right)^3 \frac{(x - x_{tr})}{c} \int_{x_{tr}}^x \frac{d \frac{x}{c}}{\left(\frac{u_e}{u_{\infty local}} \right)} \left(\frac{u_{\infty local} c}{\nu} \right)^2 \right] \right\} \\ &= 1 - \exp \left\{ (\dots) Re_{local}^2 \right\} \end{aligned} \quad (3.54)$$

where

$$\mathbf{Re}_{\text{local}} = \left(\sqrt{\left(\frac{v_{\text{Wind}}}{V_{\text{tip}}} \right)^2 + \left(\frac{r}{R} \right)^2} \right) \mathbf{Re}_{\text{tip}} \quad (3.55)$$

CHAPTER 4

ENHANCEMENTS

4.1 Turbulence Models

The starting point for this work was a version of the wind turbine analysis given in Ref. 21, with the Baldwin-Lomax turbulence model. Three new turbulence models have been added to the hybrid methodology by the present investigator: Spalart-Allmaras model, the Detached Eddy Simulation (DES) variant of the Spalart-Allmaras model, and Mentor's k-omega SST model. These turbulence models are expected to perform better than the zero-equation model in the separated flow. Rotta argued in his work that the turbulence viscosities predicted by the zero-equation models are at equilibrium while the real flow for such values is not in equilibrium. Therefore, the accuracy of the existing Baldwin-Lomax model is in question for predicting the performance of wind turbines that are often operating under separated flow conditions.

The newly implemented turbulence models solve the turbulence kinetic energy transport equation. Additionally, the two-equation model solves the dissipation transport equation. Because these transport equations have a common form it is sufficient to describe the detailed solution procedure for only one of them. In this chapter, the discretization and the solution procedure will be given for only the Spalart-Allmaras model. The transport equations for the turbulence kinetic energy and dissipation rate can be easily solved with the same procedure.

4.1.1 Spalart-Allmaras model

The baseline Spalart-Allmaras (SA) model was proposed in a paper presented at the AIAA 30th Aerospace Science Meeting and Exhibit in 1992 [42]. A minor change (later known as version Ia) was published in La Recherche Aérospatiale in 1994 [43] and is presented here.

Governing Equations

The Reynolds stress term in the Navier-Stoke equation is defined as $-\overline{u_i u_j} = 2\nu_t S_{ij}$. The eddy viscosity, ν_t , is given by:

$$\nu_t = \tilde{\nu} f_{\nu 1} \quad (4.1)$$

where $f_{\nu 1}$ is a damping function used to drive the eddy viscosity to zero near the surface. This damping factor is zero at the wall and gradually rises to unity as the distance from the wall increases. $f_{\nu 1}$ is defined as follows:

$$f_{\nu 1} = \frac{\chi^3}{\chi^3 + c_{\nu 1}^3} \text{ and } \chi = \frac{\tilde{\nu}}{\nu} \quad (4.2)$$

where, ν is the molecular viscosity calculated by the Sutherland Law.

This damping factor ensures that the turbulence viscosity coefficient should obey the transport equation except in the zone near the wall. The transport equation can be written in the form of the operating parameter $\tilde{\nu}$ as shown below.

$$\begin{aligned}
\frac{D\tilde{v}}{Dt} = & c_{b1}[1-f_{t2}]\tilde{S}\tilde{v} \\
& + \frac{1}{\sigma} \left[\nabla \cdot ((v + \tilde{v})) \nabla \tilde{v} + c_{b2} (\nabla \tilde{v})^2 \right] \\
& - \left[c_{w1} f_w - \frac{c_{b1}}{\kappa^2} f_{t2} \right] \left[\frac{\tilde{v}}{d} \right]^2 \\
& + f_{t1} \Delta U^2
\end{aligned} \tag{4.3}$$

The four terms on the right-hand side correspond to production, diffusion, dissipation, and transition/ trip effects, respectively. The individual components of the production term are defined as:

$$\tilde{S} \equiv S + \frac{\tilde{v}}{\kappa^2 d^2} f_{v2} \tag{4.4}$$

and

$$f_{v2} = 1 - \frac{\chi}{1 + \chi f_{v1}} \tag{4.5}$$

where S is the magnitude of the vorticity, and d is the distance to the closest wall.

The function f_w is the dissipation term defined as

$$\begin{aligned}
f_w = & g \left[\frac{1 + c_{w3}^6}{g^6 + c_{w3}^6} \right]^{\frac{1}{6}}, \\
g = & r + c_{w2} (r^6 - r), \\
r \equiv & \frac{\tilde{v}}{\tilde{S} \kappa^2 d^2}
\end{aligned} \tag{4.6}$$

The value of f_w will reach a constant as r increases. To avoid floating point overflow, it is recommended that the numerical value of r be limited to 10 [42]. In the present implementation, this limiting was not needed.

The function f_{t2} is defined as:

$$f_{t2} = c_{t3} \exp(-c_{t4} \chi^2) \quad (4.7)$$

The trip term is not applied in the code due to the use of a transition model, but it is mentioned here for completeness. The trip term is used to simulate the transition process so that it would suppress turbulent viscosity upstream of the transition area. The function f_{t1} is defined as

$$f_{t1} = c_{t1} g_t \exp\left(-c_{t2} \frac{\omega_t^2}{\Delta U^2} [d^2 + g_t^2 d_t^2]\right) \quad (4.8)$$

where:

d_t is the distance from the point in the flow field to the trip on the wall

ω_t is the wall vorticity at the trip

ΔU is the difference between velocity at the field point and that at the trip

$g_t \equiv \min(0.1, \Delta U / \omega_t \Delta x_t)$

Δx_t is the grid spacing along the wall at the trip

The constants are $c_{b1} = 0.1355$, $\sigma = 2/3$, $c_{b2} = 0.622$, $\kappa = 0.41$,
 $c_{w1} = \frac{c_{b1}}{\kappa^2} + \frac{(1 + c_{b2})}{\sigma}$, $c_{w2} = 0.3$, $c_{w3} = 2$, $c_{v1} = 7.1$, $c_{t1} = 1$, $c_{t2} = 2$, $c_{t3} = 1.2$, $c_{t4} = 0.5$.

It must be noted that, the last two elements (c_{t3}, c_{t4}) have numerical values in later implementations of the SA model that are different from the recommended values in the first version of SA model. The Prandtl number is equal to 0.9 for this model; there is no need to change anything for compressible flow. Density variations have very weak influence on turbulence. Thus, this issue is not a concern here.

Initial and Boundary Conditions

The initial and boundary conditions given here are for solving the dimensional equation. The non-dimensional version will be addressed later.

The wall boundary condition is $\tilde{v} = 0$. The value of \tilde{v} should be zero in the freestream as well, but anything less than $\frac{v}{10}$ is sufficient. The initial condition in the freestream should be set to a small value. Setting $\tilde{v} = \frac{v}{10}$ is recommended.

Non-Dimensionalization

The Navier-Stokes solver solves the non-dimensional form of the SA model. Therefore, the transport equation must also be rewritten in a non-dimensional form. All of the terms and parameters used must be checked and non-dimensionalized accordingly. The reference parameters are listed in the table 3.1, and are the same parameters used in the Navier-Stokes solver. For example:

$$\begin{aligned}\tilde{S} &= S + \frac{\tilde{v}}{\kappa^2 d^2} f_{v2} \\ \Rightarrow \tilde{S}^* \left(\frac{a_\infty}{L} \right) &= S^* \left(\frac{a_\infty}{L} \right) + \frac{\tilde{v}^* (v_\infty)}{\kappa^2 d^2 (L^2)} f_{v2} \\ \Rightarrow \tilde{S}^* &= S^* + \frac{\tilde{v}}{\kappa^2 d^2} f_{v2} \left(\frac{v_\infty M_{tip}}{LV_{tip}} \right) \\ \Rightarrow \tilde{S}^* &= S^* + \frac{\tilde{v}}{\kappa^2 d^2} f_{v2} \left(\frac{M_{tip}}{\text{Re}_{tip}} \right)\end{aligned}\tag{4.9}$$

Hereafter, for the sake of readability, the asterisk denoting non-dimensional quantities are dropped. After some rearrangement and non-dimensionalization, the transport equation looks as follows.

$$\begin{aligned}
\frac{D\tilde{v}}{Dt} &= c_{b1} [1 - f_{t2}] S \tilde{v} \\
&+ \frac{M_{ip}}{\text{Re}_{ip}} \frac{1}{\sigma} \frac{\partial}{\partial x_j} \left[(v + (1 + c_{b2}) \tilde{v}) \frac{\partial \tilde{v}}{\partial x_j} \right] - \frac{M_{ip}}{\text{Re}_{ip}} \frac{c_{b2}}{\sigma} \tilde{v} \frac{\partial^2 \tilde{v}}{\partial x_j^2} \\
&- \frac{M_{ip}}{\text{Re}_{ip}} \left[c_{w1} f_w - \frac{c_{b1}}{\kappa^2} [(1 - f_{t2}) f_{v2} + f_{t2}] \right] \left[\frac{\tilde{v}}{d} \right]^2 \\
&+ f_{t1} \Delta U^2 (a_\infty^2)
\end{aligned} \tag{4.10}$$

Discretization

The transport equations of the turbulence models are calculated separately from the Navier-Stokes equations. The size of the time step is the same as the main equations. It is therefore possible to take the advantage of the implicit form.

Using $\tilde{v}^{(t+1)} = \tilde{v}^{(t)} + \Delta \tilde{v}^{(t)}$, the left hand side of the transport equation can be written in a transformed coordinate system (ξ, η, ζ, τ) as:

$$\begin{aligned}
\frac{(\tilde{v} + \Delta \tilde{v}) - \tilde{v}}{\Delta \tau} + U \frac{\partial(\tilde{v} + \Delta \tilde{v})}{\partial \xi} + V \frac{\partial(\tilde{v} + \Delta \tilde{v})}{\partial \eta} + W \frac{\partial(\tilde{v} + \Delta \tilde{v})}{\partial \zeta} &= RHS \\
\frac{\Delta \tilde{v}}{\Delta \tau} + U \frac{\partial \Delta \tilde{v}}{\partial \xi} + V \frac{\partial \Delta \tilde{v}}{\partial \eta} + W \frac{\partial \Delta \tilde{v}}{\partial \zeta} &= RHS - \left(U \frac{\partial \tilde{v}}{\partial \xi} + V \frac{\partial \tilde{v}}{\partial \eta} + W \frac{\partial \tilde{v}}{\partial \zeta} \right)
\end{aligned}$$

These convection terms are discretized using the upwind scheme on both sides of the equation. The convection velocities are defined such that only one will have a value dependent on the direction of the flow.

$$\begin{aligned}
U^+ &= \frac{(U + |U|)}{2} \\
U^- &= \frac{(U - |U|)}{2}
\end{aligned} \tag{4.11}$$

Subsequently,

$$\begin{aligned}
U \frac{\partial \Delta \tilde{v}}{\partial \xi} &= U^+ (\Delta \tilde{v}_i - \Delta \tilde{v}_{i-1}) + U^- (\Delta \tilde{v}_{i+1} - \Delta \tilde{v}_i) \\
&= -U^+ \Delta \tilde{v}_{i-1} + (U^+ - U^-) \Delta \tilde{v}_i + U^- \Delta \tilde{v}_{i+1}
\end{aligned} \tag{4.12}$$

On the right-hand side, the diffusion terms are the most complicated in terms of implementation and operation count. The algebraic form can be rewritten in tensor form for simplicity. The physical coordinate is transferred to the calculation coordinate as shown below.

$$\begin{aligned}
\frac{\partial}{\partial x_j} \left[(\nu + (1 + c_{b2}) \tilde{\nu}) \frac{\partial \tilde{v}}{\partial x_j} \right] &= \xi_x \frac{\partial}{\partial \xi} \left[\xi_x () \frac{\partial \tilde{v}}{\partial \xi} \right] + \xi_y \frac{\partial}{\partial \xi} \left[\xi_y () \frac{\partial \tilde{v}}{\partial \xi} \right] + \xi_z \frac{\partial}{\partial \xi} \left[\xi_z () \frac{\partial \tilde{v}}{\partial \xi} \right] \\
&+ \eta_x \frac{\partial}{\partial \eta} \left[\eta_x () \frac{\partial \tilde{v}}{\partial \eta} \right] + \eta_y \frac{\partial}{\partial \eta} \left[\eta_y () \frac{\partial \tilde{v}}{\partial \eta} \right] + \eta_z \frac{\partial}{\partial \eta} \left[\eta_z () \frac{\partial \tilde{v}}{\partial \eta} \right] \\
&+ \zeta_x \frac{\partial}{\partial \zeta} \left[\xi_x () \frac{\partial \tilde{v}}{\partial \zeta} \right] + \zeta_y \frac{\partial}{\partial \zeta} \left[\xi_y () \frac{\partial \tilde{v}}{\partial \zeta} \right] + \zeta_z \frac{\partial}{\partial \zeta} \left[\xi_z () \frac{\partial \tilde{v}}{\partial \zeta} \right]
\end{aligned} \tag{4.13}$$

where () is shortened to $(\nu + (1 + c_{b2}) \tilde{\nu})$. Each of these nine terms can be discretized as follows. The first three terms in the ξ -direction are given below.

$$\begin{aligned}
\xi_x \frac{\partial}{\partial \xi} \left[\xi_x () \frac{\partial \tilde{v}}{\partial \xi} \right] &= \xi_{x_i} \xi_{x_{i+\frac{1}{2}}} ()_{i+\frac{1}{2}} [(\tilde{v} + \Delta \tilde{v})_{i+1} - (\tilde{v} + \Delta \tilde{v})_i] - \xi_{x_i} \xi_{x_{i-\frac{1}{2}}} ()_{i-\frac{1}{2}} [(\tilde{v} + \Delta \tilde{v})_i - (\tilde{v} + \Delta \tilde{v})_{i-1}] \\
\xi_y \frac{\partial}{\partial \xi} \left[\xi_y () \frac{\partial \tilde{v}}{\partial \xi} \right] &= \xi_{y_i} \xi_{y_{i+\frac{1}{2}}} ()_{i+\frac{1}{2}} [(\tilde{v} + \Delta \tilde{v})_{i+1} - (\tilde{v} + \Delta \tilde{v})_i] - \xi_{y_i} \xi_{y_{i-\frac{1}{2}}} ()_{i-\frac{1}{2}} [(\tilde{v} + \Delta \tilde{v})_i - (\tilde{v} + \Delta \tilde{v})_{i-1}] \\
\xi_z \frac{\partial}{\partial \xi} \left[\xi_z () \frac{\partial \tilde{v}}{\partial \xi} \right] &= \xi_{z_i} \xi_{z_{i+\frac{1}{2}}} ()_{i+\frac{1}{2}} [(\tilde{v} + \Delta \tilde{v})_{i+1} - (\tilde{v} + \Delta \tilde{v})_i] - \xi_{z_i} \xi_{z_{i-\frac{1}{2}}} ()_{i-\frac{1}{2}} [(\tilde{v} + \Delta \tilde{v})_i - (\tilde{v} + \Delta \tilde{v})_{i-1}]
\end{aligned} \tag{4.14}$$

The values at the half-points may be calculated using simple averages as:

$$\begin{aligned}
()_{i+\frac{1}{2}} &= \frac{[()_i + ()_{i+1}]}{2} \\
()_{i-\frac{1}{2}} &= \frac{[()_{i-1} + ()_i]}{2}
\end{aligned} \tag{4.15}$$

After some rearrangement, the following form results.

$$\begin{aligned}
& \xi_x \frac{\partial}{\partial \xi} \left[\xi_x () \frac{\partial \tilde{v}}{\partial \xi} \right] + \xi_y \frac{\partial}{\partial \xi} \left[\xi_y () \frac{\partial \tilde{v}}{\partial \xi} \right] + \xi_z \frac{\partial}{\partial \xi} \left[\xi_z () \frac{\partial \tilde{v}}{\partial \xi} \right] \\
&= [A] ()_{i-\frac{1}{2}} (\tilde{v} + \Delta \tilde{v})_{i-1} - \left\{ [A] ()_{i-\frac{1}{2}} + [B] ()_{i+\frac{1}{2}} \right\} (\tilde{v} + \Delta \tilde{v})_i + [B] ()_{i+\frac{1}{2}} (\tilde{v} + \Delta \tilde{v})_{i+1} \\
&= [A] ()_{i-\frac{1}{2}} \tilde{v}_{i-1} - \left\{ [A] ()_{i-\frac{1}{2}} + [B] ()_{i+\frac{1}{2}} \right\} \tilde{v}_i + [B] ()_{i+\frac{1}{2}} \tilde{v}_{i+\frac{1}{2}} \\
&+ [A] ()_{i-\frac{1}{2}} \Delta \tilde{v}_{i-1} - \left\{ [A] ()_{i-\frac{1}{2}} + [B] ()_{i+\frac{1}{2}} \right\} \Delta \tilde{v}_i + [B] ()_{i+\frac{1}{2}} \Delta \tilde{v}_{i+\frac{1}{2}}
\end{aligned} \tag{4.16}$$

where

$$[A] = \xi_{x_i} \xi_{x_{i+\frac{1}{2}}} + \xi_{x_i} \xi_{x_{i+\frac{1}{2}}} + \xi_{x_i} \xi_{x_{i+\frac{1}{2}}} \tag{4.17}$$

$$[B] = \xi_{x_i} \xi_{x_{i-\frac{1}{2}}} + \xi_{x_i} \xi_{x_{i-\frac{1}{2}}} + \xi_{x_i} \xi_{x_{i-\frac{1}{2}}}$$

Those terms with $\Delta \tilde{v}$ are implicitly treated and moved to the left-hand side of the equation. Notice that the coefficient in front of Δv_i , which form the diagonal term of the matrix, is the biggest of all the coefficients. When it is brought over to the left side, the

matrices become diagonally dominant. Terms such as $\frac{\partial^2 \tilde{v}}{\partial x_j^2}$ may be rewritten as:

$$\begin{aligned}
\frac{\partial^2 \tilde{v}}{\partial x_j^2} &= \xi_x \frac{\partial}{\partial \xi} \left[\xi_x \frac{\partial \tilde{v}}{\partial \xi} \right] + \xi_y \frac{\partial}{\partial \xi} \left[\xi_y \frac{\partial \tilde{v}}{\partial \xi} \right] + \xi_z \frac{\partial}{\partial \xi} \left[\xi_z \frac{\partial \tilde{v}}{\partial \xi} \right] \\
&+ \eta_x \frac{\partial}{\partial \eta} \left[\eta_x \frac{\partial \tilde{v}}{\partial \eta} \right] + \eta_y \frac{\partial}{\partial \eta} \left[\eta_y \frac{\partial \tilde{v}}{\partial \eta} \right] + \eta_z \frac{\partial}{\partial \eta} \left[\eta_z \frac{\partial \tilde{v}}{\partial \eta} \right] \\
&+ \zeta_x \frac{\partial}{\partial \zeta} \left[\xi_x \frac{\partial \tilde{v}}{\partial \zeta} \right] + \zeta_y \frac{\partial}{\partial \zeta} \left[\xi_y \frac{\partial \tilde{v}}{\partial \zeta} \right] + \zeta_z \frac{\partial}{\partial \zeta} \left[\xi_z \frac{\partial \tilde{v}}{\partial \zeta} \right]
\end{aligned} \tag{4.18}$$

The derivatives in each direction of (4.18) can be written in the form:

$$\begin{aligned}
& \xi_x \frac{\partial}{\partial \xi} \left[\xi_x \frac{\partial \tilde{v}}{\partial \xi} \right] + \xi_y \frac{\partial}{\partial \xi} \left[\xi_y \frac{\partial \tilde{v}}{\partial \xi} \right] + \xi_z \frac{\partial}{\partial \xi} \left[\xi_z \frac{\partial \tilde{v}}{\partial \xi} \right] \\
&= [A] \tilde{v}_{i-1} - \{ [A] + [B] \} \tilde{v}_i + [B] \tilde{v}_{i+1} + [A] \Delta \tilde{v}_{i-1} - \{ [A] + [B] \} \Delta \tilde{v}_i + [B] \Delta \tilde{v}_{i+1}
\end{aligned} \tag{4.19}$$

The same $[A]$ and $[B]$ as referred to in (4.17) are also applied here. The terms with $\Delta \tilde{v}$ are also moved to the left-hand side of the equation as the diffusion terms.

The production term, dissipation term and the trip term do not require any rigorous effort in the discretization process as they use the local parameters. However, it is possible and recommended to treat this term implicitly as well. By using $\tilde{v}^{(t+1)} = \tilde{v}^{(t)} + \Delta\tilde{v}^{(t)}$, the dissipation term is written as:

$$\left[c_{w1}f_w - \frac{c_{b1}}{\kappa^2}[(1-f_{t2})f_{v2} + f_{t2}] \right] \left[\frac{\tilde{v}^{(t+1)}}{d} \right]^2 = \left[\frac{\tilde{v}^{(t)^2} + 2\tilde{v}^{(t)}\Delta\tilde{v}^{(t)} + \Delta\tilde{v}^{(t)^2}}{d^2} \right] \quad (4.20)$$

$$\approx \left[\tilde{v}^{(t)^2} + 2\tilde{v}^{(t)} \left[\right] \Delta\tilde{v}^{(t)} + \left[\right] \Delta\tilde{v}^{(t)^2} \right]$$

using $\left[\right] = \frac{c_{w1}f_w - \frac{c_{b1}}{\kappa^2}[(1-f_{t2})f_{v2} + f_{t2}]}{d^2}$ for clarification.

Of the three parts, the last ($\left[\right] \Delta\tilde{v}^{(t)^2}$) can be neglected because it is deemed small compared to the other two terms. As the sign in front of this dissipation term is negative (refer to equation. 4.10), the second part can be moved to the left hand side to strengthen the diagonal term. This process can also be applied to the production term, but the sign in front of the production term will reduce the diagonal domination of the matrix when moved to left hand side. Therefore, it is not recommended.

Boundary and Initial Conditions

The non-dimensional quantity $\tilde{v}_\infty = 1.341946$ was used (which is about $v_\infty/10$ in the dimensional version) everywhere to initialize the eddy viscosity, except on the solid surface where it is set to zero.

Time Marching

The discretized form of transport equations can be easily represented using the following matrix form.

$$[I + \Delta\tau(U\delta_\xi + V\delta_\eta + W\delta_\zeta) + \Delta\tau(2\tilde{v}[\])]\Delta\tilde{v} = \Delta tRHS \quad (4.21)$$

where RHS are the summation of production, dissipation, diffusion and the convection terms as described in the discretization process. The $[\]$ represents:

$$\frac{\left[c_{w1}f_w - \frac{c_{b1}}{\kappa^2}[(1-f_{t2})f_{v2} + f_{t2}] \right]}{d^2}$$

The equation is in the matrix form $[M]\Delta\tilde{v} = \Delta tRHS$, which is possible to solve directly, but impractical. In this study, the matrix M was replaced by the sum $L+D+U$, where each of the element matrices L , D , and U are readily invertible.

$$(L + D + U)\Delta\tilde{v} = \Delta tRHS \quad (4.22)$$

where L is a lower block triangular matrix with null matrices on the diagonal, D is a block diagonal matrix formed out of both positive and negative flux Jacobians, and U is an upper block triangular matrix with null matrices on the diagonal. In the case of a nonsingular matrix D , the equation may be written as:

$$D(D^{-1}L + I + D^{-1}U)\Delta\tilde{v} = \Delta tRHS \quad (4.23)$$

which can be approximated as:

$$D(I + D^{-1}L)(I + D^{-1}U)\Delta\tilde{v} = \Delta tRHS \quad (4.24)$$

or

$$(D + L)D^{-1}(D + U)\Delta\tilde{v} = \Delta tRHS \quad (4.25)$$

For this SA model, these matrices may be shown to be:

$$\begin{aligned}
(D+L) &= -\Delta\tau(U^+ + V^+ + W^+ + [A])(\)_{i-\frac{1}{2}} + 1 \\
D &= (I + \Delta\tau[(U^+ + U^-) + (V^+ + V^-) + (W^+ + W^-) + 2\tilde{v}[\] + \{[A] + [B]\}(\)_i + 1]) \\
(D+U) &= \Delta\tau(U^- + V^- + W^- + [B])(\)_{i+\frac{1}{2}} + 1
\end{aligned} \tag{4.26}$$

where $[A]$ and $[B]$ are defined by equation 4.17, $(\)_{i+\frac{1}{2}}$ and $(\)_{i-\frac{1}{2}}$ are defined by equation

4.15, and $[\]$ represents
$$\frac{\left[c_{w1}f_w - \frac{c_{b1}}{\kappa^2}[(1-f_{t2})f_{v2} + f_{t2}] \right]}{d^2}.$$

The set of matrices can be solved in the process such that:

$$\begin{aligned}
(D+L)X &= \Delta t RHS \\
D^{-1}Y &= X \\
(D+U)\Delta\tilde{v} &= Y
\end{aligned} \tag{4.27}$$

where each matrix is has either lower, or diagonal, or upper part only. The inversion of these matrices can be accomplished by backward or forward substitution. The new \tilde{v} can be estimated by $\tilde{v}^{\langle t+1 \rangle} = \tilde{v}^{\langle t \rangle} + \Delta\tilde{v}^{\langle t \rangle}$.

4.1.2 Spalart-Allmaras Detached Eddy Simulation

SA model has been extensively calibrated and works well for attached, wall-bounded viscous layers, but is not suitable to handle separated flows or free shear layers. Spalart proposed a method to improve the SA model to handle such situations—the Detached Eddy Simulation (DES).

DES methodology combines both the classical SA model and a large eddy simulation (LES) in the same calculation. The classical SA model will be used near the surface; LES will be used at the free shear layer regions far away from the surface, where the turbulence scale is large enough to be captured with the coarser grid size in that

region. This approach requires much smaller computational time than the LES approach alone (which will require extremely fine grids in the near wall region) and uses the advantage of RANS in the area that does not need LES. This method aims to capture the complexities of the free shear flow in the separated areas over the rotor, and can potentially yield a more accurate performance prediction.

Spalart, Jou, Strelets, and Allmaras [45] presented this method in 1997 and used the relationship between the SA model and the Smagorinsky subgrid scale (SGS) model often used in LES. Since then, many researchers have explored this idea. Camelli and Lohner [46] have studied the coupling of the DES model with the Baldwin Lomax turbulence model; Nichols and Nelson [47] used the Menter's SST two-equation turbulence model in conjunction with a DES strategy. Other research groups, including Batten, Goldberg, and Chakravathy [48] have attempted to link RANS and LES zone using synthetic turbulence prediction. Kapadia and Roy [49] applied DES on turbo machinery cooling systems. Other researchers [50], [51] have used DES on the surface and sphere, respectively.

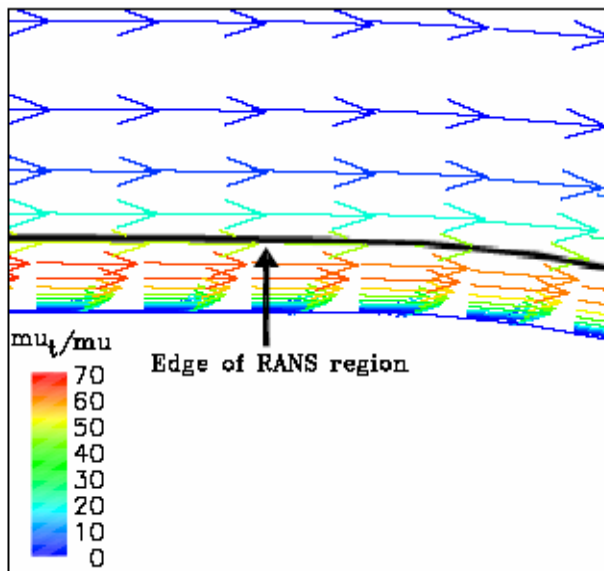


**Figure 4.9 Zones in DES methodology
(from R.H. Nichols [47])**

Johansen and colleagues [52] have also evaluated the use of DES on phase VI rotors. However, the results are based on the flow over the turbine blade as a fixed wing. DES models have also been validated for flows around basic objects (e.g., Nichols [47]). It was found that DES predicts a smaller turbulence viscosity. The flow field shows more activity than using RANS and the results in many cases can be compared to the LES results.

DES uses the idea that if the grid is fine enough, it is possible for the RANS to capture the turbulence by itself. This is possible at an area far away from the surface where the turbulence scale is comparable to the grid size in the area. Therefore, this method is especially useful in the separated flow.

This method simulates the turbulence kinetic energy transfer from large scale to smaller scale, instead of dissipation. This leads to the modification of the dissipation term

in the transport equation. This can be done by replacing the nearest wall, d by \tilde{d} , where \tilde{d} is defined as:

$$\tilde{d} \equiv \min(d, C_{DES} \Delta) \quad (4.28)$$

In this case, Δ is the largest distance from the grid point under consideration to the nearest neighbors. It can be written in mathematical form as:

$$\Delta \equiv \max(\Delta x, \Delta y, \Delta z) \quad (4.29)$$

The constant C_{DES} is set to 0.65 for the homogeneous turbulence without modification in this work. In general, the normal distance from the wall, d , is far smaller than $C_{DES} \Delta$ in the area close to the surface and the transport equation is recovered to the original SA transport equation. In the area far away from the surface, $C_{DES} \Delta$ dominates. There, the Smagorinsky turbulence viscosity $\tilde{\nu} \propto S \Delta^2$ transfers turbulence kinetic energy instead of dissipating it. The size of the viscosity predicted by the Smagorinsky model will be higher than those models using the original dissipation term, as discussed later in the calculation.

4.1.3 k- ω SST Model

The k- ω SST is one of the two models proposed by Menter [53] in 1993. Both models aim to take advantage of both k- ε and k- ω . The k- ε is the most widely used two-equation model today; however, it overpredicts the turbulence length scale in the near-wall region. This behavior, therefore, overpredicts the shear stress that might delay or prevent the separation in the area of inverse pressure gradients.

The original k- ω , based on the Wilcox 1988 model [54] and [55], has a different problem. It is very sensitive to freestream values that are specified outside the shear layer.

It was found that the solution to the transport equations could deviate significantly with different values of ω in the far field.

The original k- ω model is given by

$$\frac{D\rho k}{Dt} = \tau_{ij} \frac{\partial u_i}{\partial x_j} + \beta^* \rho \omega k + \frac{\partial}{\partial x_j} \left[(\mu + \sigma_{k1} \mu_t) \frac{\partial k}{\partial x_j} \right] \quad (4.30)$$

$$\frac{D\rho \omega}{Dt} = \frac{\gamma_1}{v_t} \tau_{ij} \frac{\partial u_i}{\partial x_j} - \beta_1 \rho \omega^2 + \frac{\partial}{\partial x_j} \left[(\mu + \sigma_{\omega 1} \mu_t) \frac{\partial \omega}{\partial x_j} \right] \quad (4.31)$$

where the model constants are

$$\sigma_{k1} = 0.85, \sigma_{\omega 1} = 0.5, \beta_1 = 0.0750, \beta^* = 0.09, \kappa = 0.41, \gamma_1 = \frac{\beta_1}{\beta^*} - \frac{\sigma_{\omega 1} \kappa^2}{\sqrt{\beta^*}}$$

The relationship between ε and ω is:

$$\varepsilon = \beta^* k \omega \quad (4.32)$$

It should be noted that many papers use C_μ in place of β^* .

The k- ε can be rewritten in the form of ω as:

$$\frac{D\rho k}{Dt} = \tau_{ij} \frac{\partial u_i}{\partial x_j} + \beta^* \rho \omega k + \frac{\partial}{\partial x_j} \left[(\mu + \sigma_{k1} \mu_t) \frac{\partial k}{\partial x_j} \right] \quad (4.33)$$

$$\frac{D\rho \omega}{Dt} = \frac{\gamma_2}{v_t} \tau_{ij} \frac{\partial u_i}{\partial x_j} - \beta_2 \rho \omega^2 + \frac{\partial}{\partial x_j} \left[(\mu + \sigma_{\omega 2} \mu_t) \frac{\partial \omega}{\partial x_j} \right] + 2\rho \sigma_{\omega 2} \frac{1}{\omega} \frac{\partial k}{\partial x_j} \frac{\partial \omega}{\partial x_j} \quad (4.34)$$

However, the constants are set differently from those of original k- ε equations. These are shown below.

$$\sigma_{k2} = 1.0, \sigma_{\omega 2} = 0.856, \beta_2 = 0.0828, \beta^* = 0.09, \kappa = 0.41, \gamma_1 = \frac{\beta_2}{\beta^*} - \frac{\sigma_{\omega 2} \kappa^2}{\sqrt{\beta^*}}$$

The last term of the second transport equation is the cross diffusion term. This term arises from the difference of the coefficients between ε and ω equations, which makes the two equations different. More information can be found in Wilcox [53].

Governing Equations

Menter[53] utilizes both models by using the original k- ω model near the solid surface and changes gradually to k- ε in the freestream. The change is smoothly controlled by the weight function of the coefficients on both models. The combined form of the k- ω and k- ε can be written in a form that utilizes k and ω as follows:

$$\frac{D\rho k}{Dt} = \tau_{ij} \frac{\partial u_i}{\partial x_j} + \beta^* \rho \omega k + \frac{\partial}{\partial x_j} \left[(\mu + \sigma_{k1} \mu_t) \frac{\partial k}{\partial x_j} \right] \quad (4.35)$$

$$\frac{D\rho \omega}{Dt} = \frac{\gamma}{\nu_t} \tau_{ij} \frac{\partial u_i}{\partial x_j} - \beta \rho \omega^2 + \frac{\partial}{\partial x_j} \left[(\mu + \sigma_\omega \mu_t) \frac{\partial \omega}{\partial x_j} \right] + 2\rho(1 - F_1) \sigma_\omega \frac{1}{\omega} \frac{\partial k}{\partial x_j} \frac{\partial \omega}{\partial x_j} \quad (4.36)$$

The weight function is defined as:

$$\phi = F_1 \phi_1 + (1 - F_1) \phi_2 \quad (4.37)$$

where ϕ are those coefficient of both k-omega and k-epsilon equations. The function F_1 is defined as:

$$F_1 = \tanh(\arg_1^4) \quad (4.38)$$

with:

$$\arg_1 = \min \left(\max \left(\frac{\sqrt{k}}{0.09\omega y}, \frac{500\nu}{y^2\omega} \right), \frac{4\rho\sigma_{\omega 2}k}{CD_{k\omega}y^2} \right) \quad (4.39)$$

where y is the distance to the nearest surface and $CD_{k\omega}$ is the cross-diffusion term as defined below.

$$CD_{k\omega} = \max\left(2\rho\sigma_{\omega 2} \frac{1}{\omega} \frac{\partial k}{\partial x_j} \frac{\partial \omega}{\partial x_j}, 10^{-20}\right) \quad (4.40)$$

The turbulence stress tensor $\tau_{ij} = -\overline{\rho u_i u_j}$ is:

$$\tau_{ij} = \mu_t \left(\frac{\partial u_i}{\partial x_j} + \frac{\partial u_j}{\partial x_i} - \frac{2}{3} \frac{\partial u_k}{\partial x_k} \delta_{ij} \right) - \frac{2}{3} \rho k \delta_{ij} \quad (4.41)$$

The turbulence viscosity can be estimated from

$$\nu_t = \frac{a_1 k}{\max(a_1 \omega, \Omega F_2)} \quad (4.42)$$

where Ω is the absolute value of the vorticity, $a_1 = 0.31$, and F_2 is given by:

$$F_2 = \tanh(\arg_2^2) \quad (4.43)$$

with:

$$\arg_2 = \max\left(2 \frac{\sqrt{k}}{0.09\omega y}, \frac{500\nu}{y^2\omega}\right) \quad (4.44)$$

Non-Dimensionalization

The non-dimensional form of the transport equations can be written as:

$$\frac{D\rho k}{Dt} = \tau_{ij} \frac{\partial u_i}{\partial x_j} \left(\frac{M_{tip}}{\text{Re}_{tip}} \right) + \beta^* \rho \omega k \left(\frac{\text{Re}_{tip}}{M_{tip}} \right) + \frac{\partial}{\partial x_j} \left[(\mu + \sigma_{k1} \mu_t) \frac{\partial k}{\partial x_j} \right] \left(\frac{M_{tip}}{\text{Re}_{tip}} \right) \quad (4.45)$$

$$\begin{aligned} \frac{D\rho\omega}{Dt} = & \frac{\gamma}{\nu_t} \tau_{ij} \frac{\partial u_i}{\partial x_j} \left(\frac{M_{tip}}{\text{Re}_{tip}} \right) - \beta \rho \omega^2 \left(\frac{\text{Re}_{tip}}{M_{tip}} \right) + \frac{\partial}{\partial x_j} \left[(\mu + \sigma_\omega \mu_t) \frac{\partial \omega}{\partial x_j} \right] \left(\frac{M_{tip}}{\text{Re}_{tip}} \right) \\ & + 2\rho(1-F_1)\sigma_\omega \frac{1}{\omega} \frac{\partial k}{\partial x_j} \frac{\partial \omega}{\partial x_j} \left(\frac{M_{tip}}{\text{Re}_{tip}} \right) \end{aligned} \quad (4.46)$$

The weight function is defined in the same manner as the dimension form:

$$\phi = F_1 \phi_1 + (1 - F_1) \phi_2 \quad (4.47)$$

where ϕ are those coefficient of both k-epsilon and k-omega equations. The function F_1 is defined as:

$$F_1 = \tanh(\arg_1^4) \quad (4.48)$$

with:

$$\arg_1 = \min \left(\max \left(\frac{\sqrt{k}}{0.09\omega y} \left(\frac{M_{tip}}{\text{Re}_{tip}} \right), \frac{500\nu}{y^2\omega} \left(\frac{M_{tip}}{\text{Re}_{tip}} \right)^2, \frac{4\rho\sigma_{\omega_2}k}{CD_{k\omega}y^2} \right) \right) \quad (4.49)$$

where y is the distance to the nearest surface and $CD_{k\omega}$ is the cross-diffusion term as shown above or as defined in (4.43) The turbulence stress tensor $\tau_{ij} = -\rho \overline{u_i' u_j'}$ is:

$$\tau_{ij} = \mu_t \left(\frac{\partial u_i}{\partial x_j} + \frac{\partial u_j}{\partial x_i} - \frac{2}{3} \frac{\partial u_k}{\partial x_k} \delta_{ij} \right) - \frac{2}{3} \rho k \delta_{ij} \quad (4.50)$$

The turbulence viscosity is estimated from

$$\nu_t = \min \left(\frac{\rho k}{\omega}, \frac{a_1 \rho k}{\Omega F_2} \left(\frac{\text{Re}_{tip}}{M_{tip}} \right) \right) \quad (4.51)$$

where Ω is the absolute value of the vorticity, $a_1 = 0.31$, and F_2 is given by:

$$F_2 = \tanh(\arg_2^2) \quad (4.52)$$

with

$$\arg_2 = \max \left(2 \frac{\sqrt{k}}{0.09\omega y} \left(\frac{M_{tip}}{\text{Re}_{tip}} \right), \frac{500\nu}{y^2\omega} \left(\frac{M_{tip}}{\text{Re}_{tip}} \right)^2 \right) \quad (4.53)$$

Initial and Boundary Conditions

The following dimensional initial freestream values are chosen to apply to the whole flow except at the solid surface:

$$\begin{aligned} \omega_\infty &= (1 \rightarrow 10) \frac{U_\infty}{L} \\ \nu_{t\infty} &= 10^{-3} \nu \\ k_\infty &= \nu_{t\infty} \omega_\infty \end{aligned} \quad (4.54)$$

In the non-dimensional version, the freestream values are also used as the initial values except on the solid surface and are set as follows:

$$\begin{aligned} \omega_\infty &= 1 \times 10^{-6} \\ \nu_{t\infty} &= 0.009 \\ k_\infty &= 9 \times 10^{-9} \end{aligned} \quad (4.55)$$

Transition Prediction

The model is based on the work of Langtry and Sjolander [56], which is a modification of Wilcox's 1994 low-Reynolds number model [57]. The model is centered on the Vorticity Reynolds Number as defined as

$$\text{Re}_v = \frac{\rho y^2}{\mu} \frac{\partial u}{\partial y} = \frac{\rho y^2}{\mu} \Omega \quad (4.56)$$

or

$$\text{Re}_v = \frac{\rho y^2}{\mu} \Omega \left(\frac{\text{Re}_{tip}}{M_{tip}} \right) \quad (4.57)$$

in non-dimensional form.

This model controls the transition from laminar to turbulent through the regulation of production terms in the turbulence kinetic energy transport equation. The damping factor (PTM) is multiplied with the original production term in the k - ω SST model. This function is defined as:

$$PTM = 1 - (PTM_1 + PTM_2)F_3 \quad (4.58)$$

$$PTM_1 = \begin{cases} 1 - \left[\begin{aligned} &(3.82 \times 10^{-4})\text{Re}_v + (-3.94 \times 10^{-7})\text{Re}_v^2 \\ &+ (1.43 \times 10^{-10})\text{Re}_v^3 \end{aligned} \right], \text{Re}_v < 1000 \\ 1 - [0.12 + (1 \times 10^{-5})\text{Re}_v], \text{Re}_v \geq 1000 \end{cases}$$

$$PTM_2 = \begin{cases} -|K|^{0.4} \frac{\text{Re}_v}{80}, K < 0 \\ 0, K \geq 0 \end{cases} \quad (4.59)$$

$$K = -\frac{\mu}{\rho^2 U^3} [1 - M^2] \frac{dp}{ds}$$

The non-dimensional form of K is written as:

$$K = -\frac{\mu}{\rho^2 U^3} [1 - M^2] \frac{dp}{ds} \left(\frac{M_{tip}}{\text{Re}_{tip}} \right) \quad (4.60)$$

The new transport equations are rewritten as:

$$\frac{D\rho k}{Dt} = PTM \cdot \tau_{ij} \frac{\partial u_i}{\partial x_j} + \beta^* \rho \omega k + \frac{\partial}{\partial x_j} \left[(\mu + \sigma_{k1} \mu_t) \frac{\partial k}{\partial x_j} \right] \quad (4.61)$$

$$\frac{D\rho \omega}{Dt} = \frac{\gamma}{v_t} \tau_{ij} \frac{\partial u_i}{\partial x_j} - \beta \rho \omega^2 + \frac{\partial}{\partial x_j} \left[(\mu + \sigma_\omega \mu_t) \frac{\partial \omega}{\partial x_j} \right] + 2\rho(1 - F_1) \sigma_\omega \frac{1}{\omega} \frac{\partial k}{\partial x_j} \frac{\partial \omega}{\partial x_j} \quad (4.62)$$

or in non-dimensional form as:

$$\frac{D\rho k}{Dt} = PTM \cdot \tau_{ij} \frac{\partial u_i}{\partial x_j} \left(\frac{M_{tip}}{Re_{tip}} \right) + \beta^* \rho \omega k \left(\frac{Re_{tip}}{M_{tip}} \right) + \frac{\partial}{\partial x_j} \left[(\mu + \sigma_{k1} \mu_t) \frac{\partial k}{\partial x_j} \right] \left(\frac{M_{tip}}{Re_{tip}} \right) \quad (4.63)$$

$$\begin{aligned} \frac{D\rho\omega}{Dt} &= \frac{\gamma}{\nu_t} \tau_{ij} \frac{\partial u_i}{\partial x_j} \left(\frac{M_{tip}}{Re_{tip}} \right) - \beta \rho \omega^2 \left(\frac{Re_{tip}}{M_{tip}} \right) + \frac{\partial}{\partial x_j} \left[(\mu + \sigma_{\omega} \mu_t) \frac{\partial \omega}{\partial x_j} \right] \left(\frac{M_{tip}}{Re_{tip}} \right) \\ &+ 2\rho(1-F_1)\sigma_{\omega} \frac{1}{\omega} \frac{\partial k}{\partial x_j} \frac{\partial \omega}{\partial x_j} \left(\frac{M_{tip}}{Re_{tip}} \right) \end{aligned} \quad (4.64)$$

Furthermore, other parameters also need modification. These are the transformation parameters as described below:

$$R_k = 6, R_{\omega} = 6, R_{\beta} = 6, R_T = \frac{\mu_T}{\mu}$$

$$\sigma_{k1} = 0.85, \sigma_{\omega1} = 0.5, \beta_1 = 0.0750, \gamma_0 = 0.1, \gamma_1 = \frac{5\gamma_0 + (R_T/R_{\omega})}{9 + (R_T/R_{\omega})},$$

$$\beta_1^* = 0.09 \cdot \frac{5/18 + (R_T/R_{\beta})^4}{1 + (R_T/R_{\beta})^4}$$

$$\sigma_{k2} = 1.0, \sigma_{\omega2} = 0.856, \beta_2 = 0.828, \kappa = 0.41, \gamma_2 = \frac{\beta_2}{\beta_2^*} - \frac{\sigma_{\omega2}\kappa}{\sqrt{\beta_2^*}}, \beta_2^* = 0.09$$

In addition, the turbulence viscosity estimation is also changed. It is now estimated from:

$$\mu_t = \min \left[\alpha^* \frac{\rho k}{\omega}, a_1 \frac{\rho k}{\Omega F_2} \right] \quad (4.65)$$

The new parameter α^* is also calculated based on zone using

$$\alpha_1^* = \frac{\beta_1/3 + R_T/R_k}{1 + R_T/R_k}$$

and

$$\alpha_2^* = 1$$

These parameters would be used to replace those in the original k-omega SST model. The computational processes for discretizing and solving the transport equations remain the same as that for the SA model described earlier.

4.2 The LU SGS Process

In the early versions of the wind turbine analyses [Ref. 22] the Navier-Stokes equations were originally solved by the ADI process. This method, though straightforward, required a set of arbitrary numerical viscosities. Yoon and Jameson [58] proposed the LU SGS method. This method takes advantage of a strong diagonal dominance and provides very built-in locally adaptive numerical viscosity that, in turn, generates a very stable calculation. It may be expanded for use with multiprocessing machines in the future [59], [60], [61].

After normalizing the dimensional equations, the non-dimensional form of the equations can be rewritten in vector form as:

$$\left[I + \Delta t \delta_\xi \hat{A} + \Delta t \delta_\eta \hat{B} + \Delta t \delta_\zeta \hat{C} \right] \Delta q = -\Delta t J [RHS] \quad (4.66)$$

where

$$\hat{A} = \frac{\partial \hat{E}}{\partial \hat{q}} = \hat{A}^+ + \hat{A}^- \quad (4.67)$$

\hat{E} is the vector F, G, H in the Navier-Stokes equations as shown in previous chapter.

The exact values of \hat{A}^+, \hat{A}^- can be calculated from the relation shown in equations (4.72, 4.73). However, it is very expensive to compute their exact metrics.

$$\hat{A}^+ = T \Lambda^+ T^+ \quad (4.68)$$

$$\hat{A}^- = T\Lambda^-T^- \quad (4.69)$$

There are many ways to approximate the value of these metrics. This work uses Yoon and Jameson's model that estimate the values of \hat{A}^+ , \hat{A}^- from

$$\hat{A}^+ = \frac{\hat{A} + (|U| + a|\bar{\nabla}\xi|)}{2} \quad (4.70)$$

$$\hat{A}^- = \frac{\hat{A} - (|U| + a|\bar{\nabla}\xi|)}{2} \quad (4.71)$$

The same process is also applied to \hat{B}^+ , \hat{B}^- , \hat{C}^+ and \hat{C}^- . The values are dependent on the velocity components from the respective dimension.

The resulting form is:

$$\left[I + \Delta t \delta_\xi \hat{A}^+ + \Delta t \delta_\xi \hat{A}^- + \Delta t \delta_\eta \hat{B}^+ + \Delta t \delta_\eta \hat{B}^- + \Delta t \delta_\zeta \hat{C}^+ + \Delta t \delta_\zeta \hat{C}^- \right] \Delta q = -\Delta t J [RHS] \quad (4.72)$$

Equation (4.72) has a matrix on the left hand side that is similar in form to the L+D+U matrix described earlier for the SA equation, and may be solved in a very similar manner.

For further details of the LU-SGS scheme, the reader is referred to Ref. [58].

CHAPTER 5

WIND TURBINE STATES

5.1 The Actuator Disc Concept

A wind turbine is a device that extracts kinetic energy from the wind and converts it to the shaft torque. As some of its kinetic energy is removed, the wind that passes through the rotor disc slows down. In actuator disc models, it is assumed that the air particles that pass through the disc do not interfere with the stationary particles outside the stream tube. This stream tube extended far upstream as well as downstream of the rotor forming a long tube of circular cross section as shown in figure 5.1.

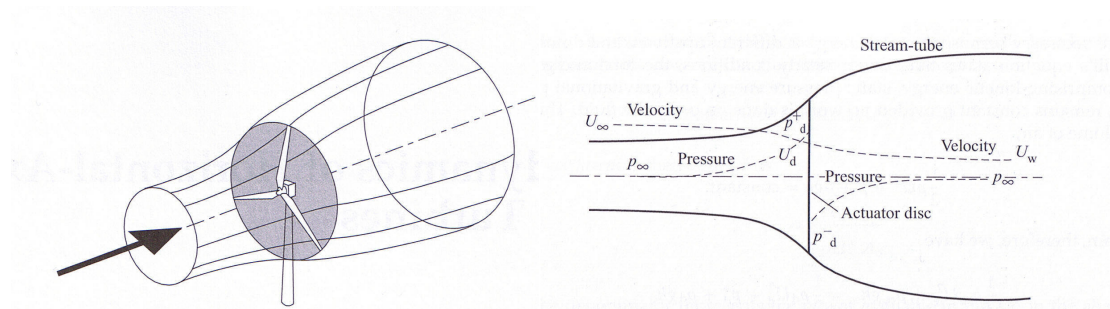


Figure 5.1 Energy-extracting actuator disc and stream tube
(from T. Burton [64])

The approaching air upstream of the turbine will gradually slow down in the presence of a wind turbine. To conserve mass, the stream tube expands as shown above. However, except when the particles cross the actuator disc, no energy is extracted from the air particles. Bernoulli's equation is thus applicable upstream and downstream of the rotor, but not across the rotor. The static pressure gradually rises both upstream and downstream of the rotor to compensate for the

decrease of kinetic energy. Across the rotor disk, there is an abrupt drop in static pressure as energy is extracted from the air particles. The static pressure begins to rise downstream of the rotor disk and eventually recovers to the atmospheric pressure far downstream..

From conservation of mass, under 1-D steady incompressible flow assumptions,

$$\rho A_{\infty} U_{\infty} = \rho A_d U_d = \rho A_w U_w \quad (5.1)$$

The symbol ∞ refers to conditions far upstream, d refers to condition at the disc, and w refers to conditions in the far wake.

The difference between far upstream velocity and the velocity at the disc is due to the effect of induced velocity. Therefore, the net streamwise velocity at the disk is:

$$U_d = U_{\infty}(1 - a) \quad (5.2)$$

where a is the induction factor. Far downstream of the rotor, for conservation of momentum and energy, it may be shown ([64] or [62]) that:

$$U_w = U_{\infty}(1 - 2a) \quad (5.3)$$

It should be noted that this concept does not take into account losses associated with viscous losses, swirl losses, and tip losses.

5.2 Momentum Theory

From conservation of momentum principles,

$$\text{Rate of change of momentum of the fluid particles} = F = (U_{\infty} - U_w)\rho A_d U_d \quad (5.4)$$

This rate of change of momentum is equal to the pressure forces exerted by the rotor disk on the fluid particles. Thus,:

$$F = (p_d^+ - p_d^-)A_d = 2\rho A_d U_{\infty}^2(1 - a) \quad (5.5)$$

The power extracted from the rotor may be estimated by applying the conservation of energy to a control volume across the actuator disk. It may be shown that:

$$Power = 2\rho A_d U_\infty^3 (1 - a) \quad (5.6)$$

The power coefficient is defined as:

$$C_p = \frac{Power}{\frac{1}{2}\rho U_\infty^3 A_d} = 4a(1 - a)^2 \quad (5.7)$$

The torque coefficient is estimated as:

$$C_T = \frac{Power}{\frac{1}{2}\rho U_\infty^2 A_d} = 4a(1 - a) \quad (5.8)$$

Figure 5.2 shows the variation of power coefficient as a function of induction factor. Setting the derivative of C_p with respect to a to zero, we can determine the induction factor that maximizes power extraction. $a = \frac{1}{3}$. At that point $C_{p_{max}} = \frac{16}{27} = 0.593$. In other words, only 59.3% of the kinetic energy of the particles course the rotor disk can be extracted under ideal conditions. This limit is known as the Betz limit. Wind turbine designers strive to optimize the blade (planform, twist, airfoil shape, tip speed, and number of blades) to achieve a power coefficient that is as close to the Betz limit as possible

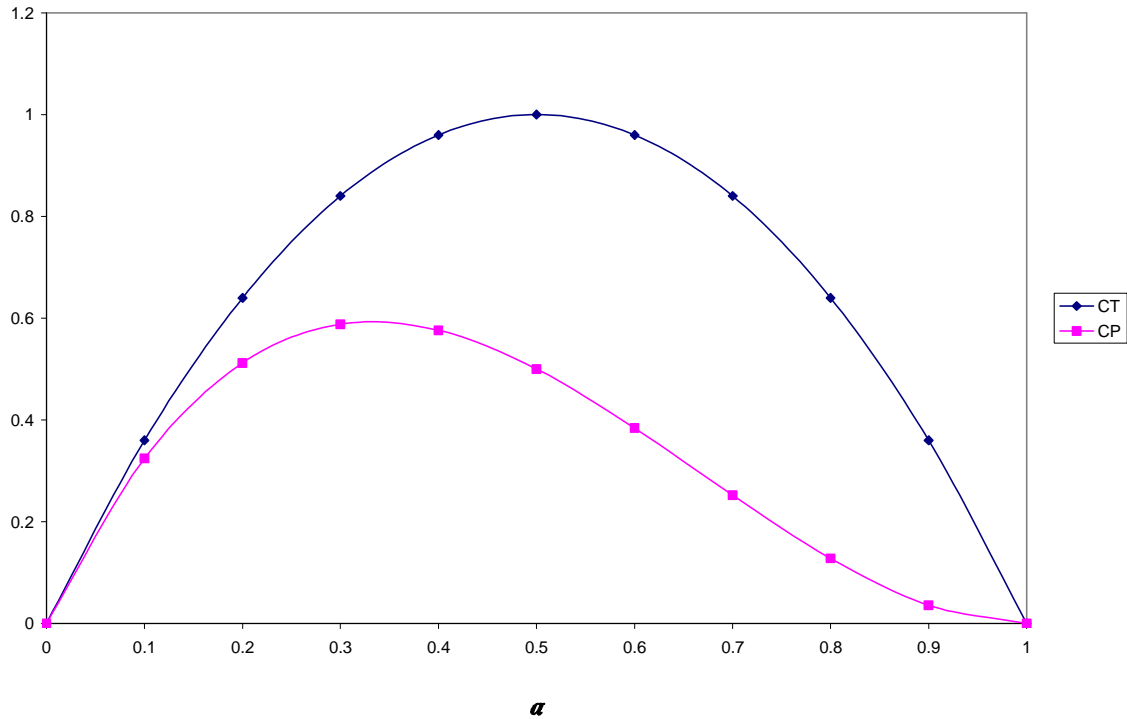


Figure 5.2 Variation of C_p and C_T with axial induction factor (from T. Burton [64])

5.3 Wind Rotor States

Although wind turbine rotor is usually operated close to its design point to extract energy from the wind and convert it into shaft power, other states of operations may occur. A wind turbine designer should have an understanding of these states and loads, dynamics, and control. The theory of rotor state was proposed by Glauert [63] and was extended later by others, e.g. Wilson and Lissaman [65]. It was corrected with the known helicopter data by Stoddard [66].

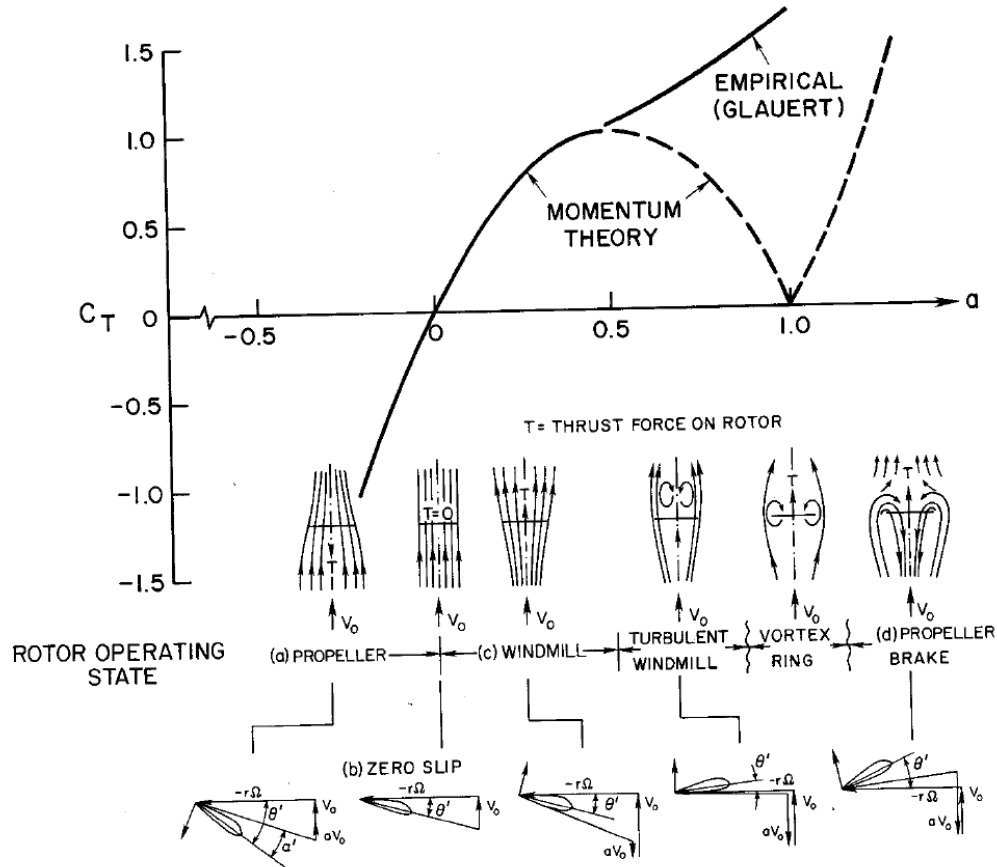


Figure 5.3 Rotor states
 (from D. M. Eggleston and F. S. Stoddard [62])

Although wind turbine is normally designed to operate in the windmill state, other states of operation may occur. Consider a rotor encountering a wind velocity, V_0 . We assume that the rotor angular velocity is kept constant at Ω , by adding or withdrawing the power on the rotor shaft. The blade pitch angle is θ' and the relative wind angle as ϕ . The effect of induced velocity is to modify the effective angle of attack that the blade sees by an amount $a = \frac{v}{V_0}$ as shown in figure 5.3. If the pitch angle θ' is greater than the relative wind angle ϕ , the rotor operates as a propeller and does work on the fluid particles. If the fluid particles are accelerated

through the rotor. Torque must be supplied to the rotor to maintain a constant Ω . This leads to a negative C_T in the plot in figure 5.2.

Figure 5.3(b) shows the zero slip state. This state is characterized by $\theta' = \phi$. Thus, angle of attack is zero. Without lift there is no induced velocity and a and v are zero in this state. If there is no friction, wind turbine can operate at constant wind speed without need of power input. At this point C_T is zero. When $0 < \theta' < \phi$, windmill state or windmill break state occurs. This state covers $0 < a < 0.5$. Rotor generates power and C_T is positive. It must be noted that momentum theory is valid in this regime. After θ' turns negative, rotor progressively goes through the turbulent windmill, vortex ring, and propeller break states. Torque and power production no longer follow momentum theory prediction. The characteristics of the rotor from this point resemble those of a helicopter.

The induced velocity increases in magnitude and results in a delay in the movement of vortex carried away from the rotor tip. If the induced velocity magnitude close to the incoming wind speed, $a=1$, the tip vortex does not convect away from the rotor disk. The tip vortices collect around the tip of the rotor in a doughnut shape as a vortex ring. This ring periodically disintegrates releasing pockets of vorticity into the flow, and reforms. The vortex ring state is thus highly unsteady.

The last state happens when the induced velocity is higher than incoming wind speed, $a > 1$. Thus incoming flow is being pushed backwards against the direction of the wind. This is the same as the powered descent of a helicopter.

Further information of all of these states can be found in the work by Sorensen [67]. Though some states might be very rare in nature, all can be easily extracted from the simulations using scientific visualization techniques.

5.4 States of Phase VI Rotors

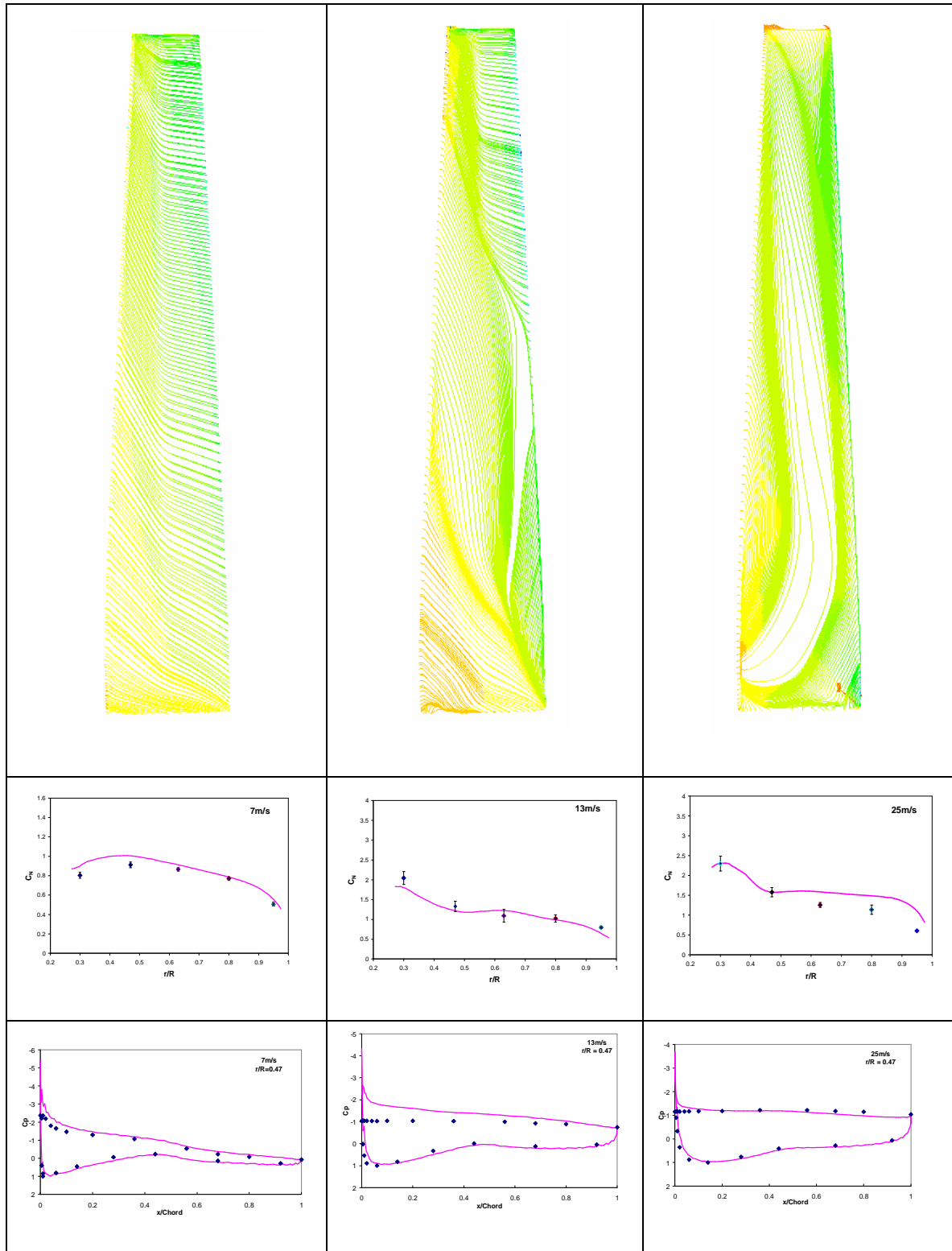


Figure 5.4 Flow field and force coefficients for phase VI rotor at low, intermediate, and high wind speeds

The phase VI rotor is stall-regulated. It is designed to operate mainly in a wind mill state. However, as all other stall-regulated turbines, it incorporates mechanism to regulate power output at designed levels. This can be achieved by allowing part of the blade to stall while other unaffected areas continue to generate torque. In figure 5.4, on the left, at low wind speed the angle of attack observed by the turbine blade is comparatively small. Thus, air flows around the blade smoothly without separation.

At moderate wind speed, stall occurs at some radial locations while higher power is generated at other radial locations. This results in a comparatively constant power output against varied wind speed. In this study, stall occurs from 9 m/s onward. The center chart in figure 5.4 presents the flow at 13 m/s where stall can be clearly seen from the root up to around mid-point span. The area close to the tip is where more than half of torque is generated and flow is still attached. The effect of the stall evidences in the drop of C_N in the area close to the root station. Furthermore, it can be seen in the flow field that the stall occurs near the leading edge. This effect is in the absence of suction peak in C_p distribution plot as well.

At high wind speeds, stall covers all the upper surface of the turbine blade. In this phase VI configuration, such a phenomenon occurs from 20 m/s onward. The force coefficient shows relatively low magnitude across the entire span. The pressure coefficient shown in this case is typical for all radial stations as well.

CHAPTER 6

RESULTS AND DISCUSSION

This chapter will present the results from the calculations and compare them with the wind tunnel data for the NREL Phase VI rotor. Several advanced turbulence models have been assessed. Grid sensitivity studies and the effectiveness of the transition models have been studied. The way that these enhancements affect the final results will be discussed.

The detailed operational state of the wind turbine will be provided to illustrate the wind power extraction process that was explained in the previous chapter. This information will present the difference in the physics of the flow at different wind speeds, and will be followed by a demonstration of the effects of several turbulence models, different grid densities, and transition models.

6.1 Computational Setting

6.1.1 Available Computational Options

There are several enhancement options available in the code. However, it is impractical to activate all of them as they may mutually interfere with each other or increase the computational time to unacceptable levels. Therefore, these options were studied one at a time, with the baseline 3rd order upwind scheme.

Both root and tip vortex models are activated. Root vortex, in particular, can have some influence because of its proximity to the blade. The strength of the root vortex is computed as part of the solution and may be comparable in strength to that of the tip vortex. The thin layer version of Navier-Stokes equations was solved using constant time steps.

The Michel and the Eppler criteria are the two transition models available in the code. The effect of both will be explored later in Section 6.4. It is possible that these transition models will play some role in the prediction.

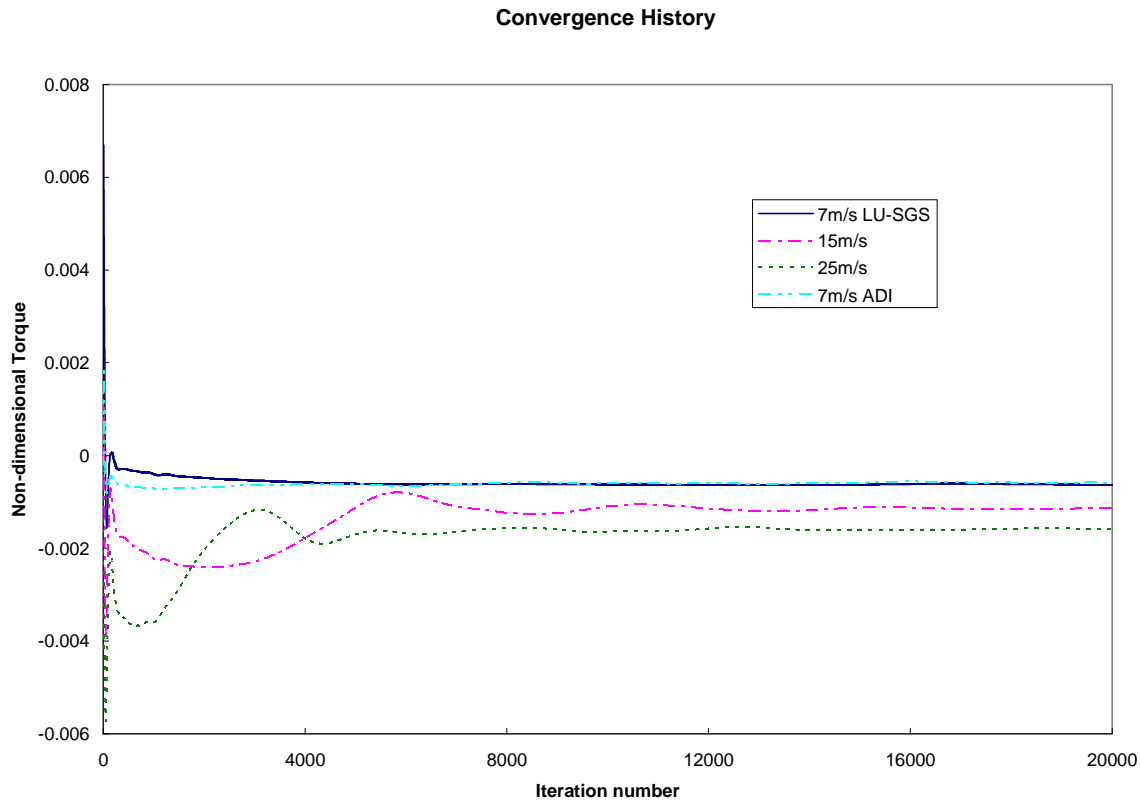


Figure 6.1 Convergence history

Figure 6.1 shows a typical converge history for torque. The time step corresponds to 0.01 degree of azimuth. The computations are seem to converge within 9,000 steps (approximately 1/4 revolution), but are extended to 24,000 steps ensure that the solution are adequately converged. These calculations were done using LU-SGS implicit scheme described in chapter 4.

It can be seen that higher wind speed cases required more time steps to converge to limit cycle state. At these high wind speeds unsteady features such as vortex shedding was observed and the torque oscillated about a mean cycle value.

6.1.2 Effect of the Shed Vortices

These simulations include only the induced velocity due to the trailing vortices from root and the tip. Shed vortex effects were not included. Tongchitpakdee [33] has considered shed vortex effects and found this influence to be negligible compared to the root and tip vortex effects.

6.1.3 Grid

In an effort to ensure grid resolution near the leading and trailing edge, and to ensure adequate spacing within the boundary layer, the simulations were done on a C-grid containing only one blade. The effect of the other blades is simulated through the effect of the tip and root vortices from all the blades. The effect of tower was not included

All the calculations were done with a C-H grid generated by the hyperbolic single block structured grid generator. The three dimensional grid is constructed from a series of 2-D C-grid with H-type topology in the radial direction. The grid generator has a built-in elliptic solver to improve the quality of the grid. This elliptic smoothing was not found necessary in this work.

The grid is clustered near the rotor leading edge and trailing edge, and at the root and tip in order to accurately capture root and tip vortex, respectively. There are about 1.7 million grid points in one block. There are 201 points in the wrap-around direction, 105 points on the span-wise direction, and 81 points in the direction normal to the surface. A grid spacing ratio of 2,000:100:1 (streamwise, radial, and normal) was found desirable.

In order to handle the viscous effects efficiently, the first grid point is set to have $y^+ < 5$ in most cases. This was achieved by setting the first spacing in normal direction to be of the order of $10^{-5} c$, where c is the local chord. This places three to four points inside the viscous sub layer. The computational area extends about six times that of the reference chord in all directions

to capture adequate flow phenomena. A sample of grid and the details near the solid surface are shown in figures 6.2 and 6.3, respectively.

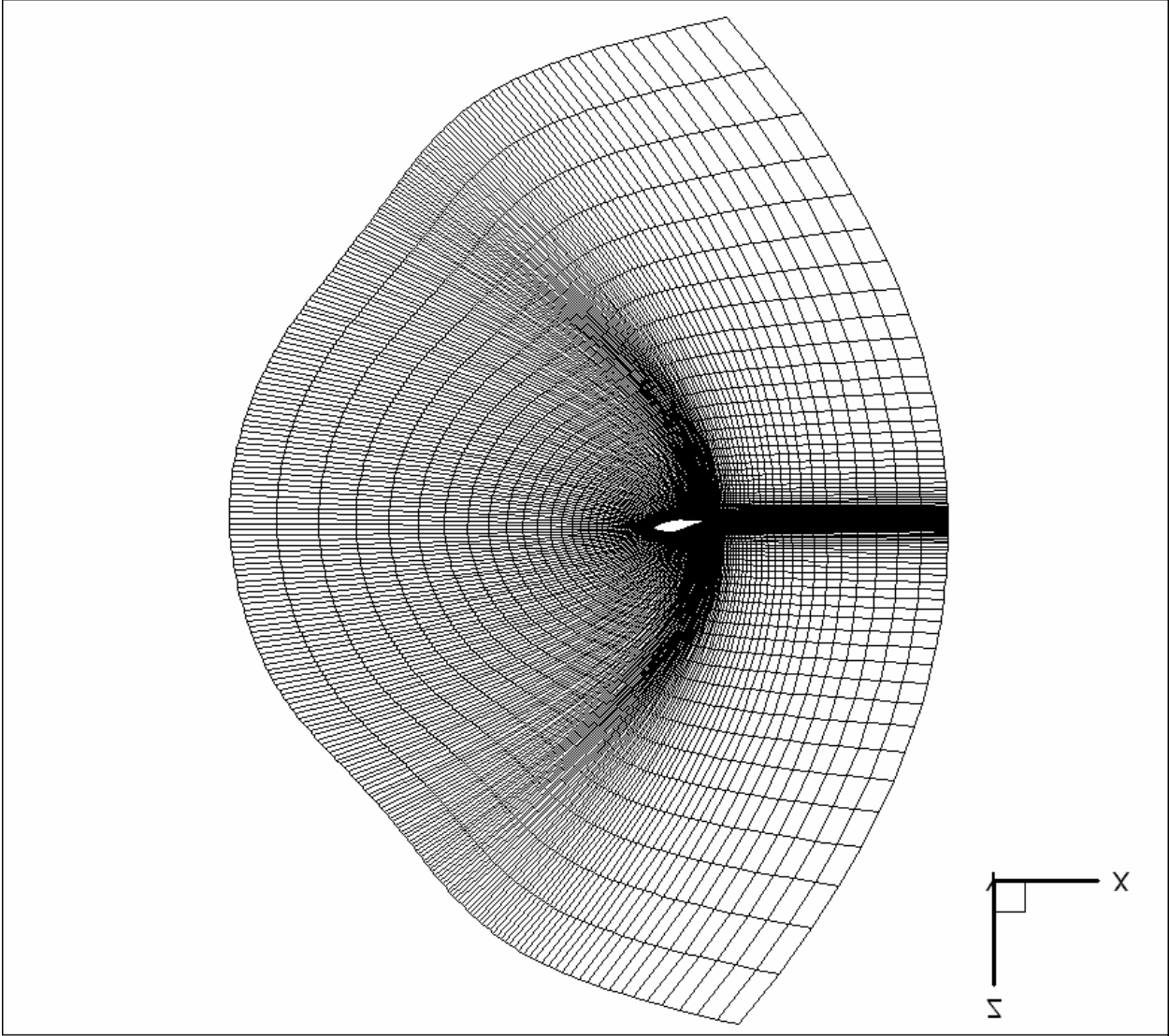


Figure 6.2 Sectional view of the computational C-grid at a typical radial location

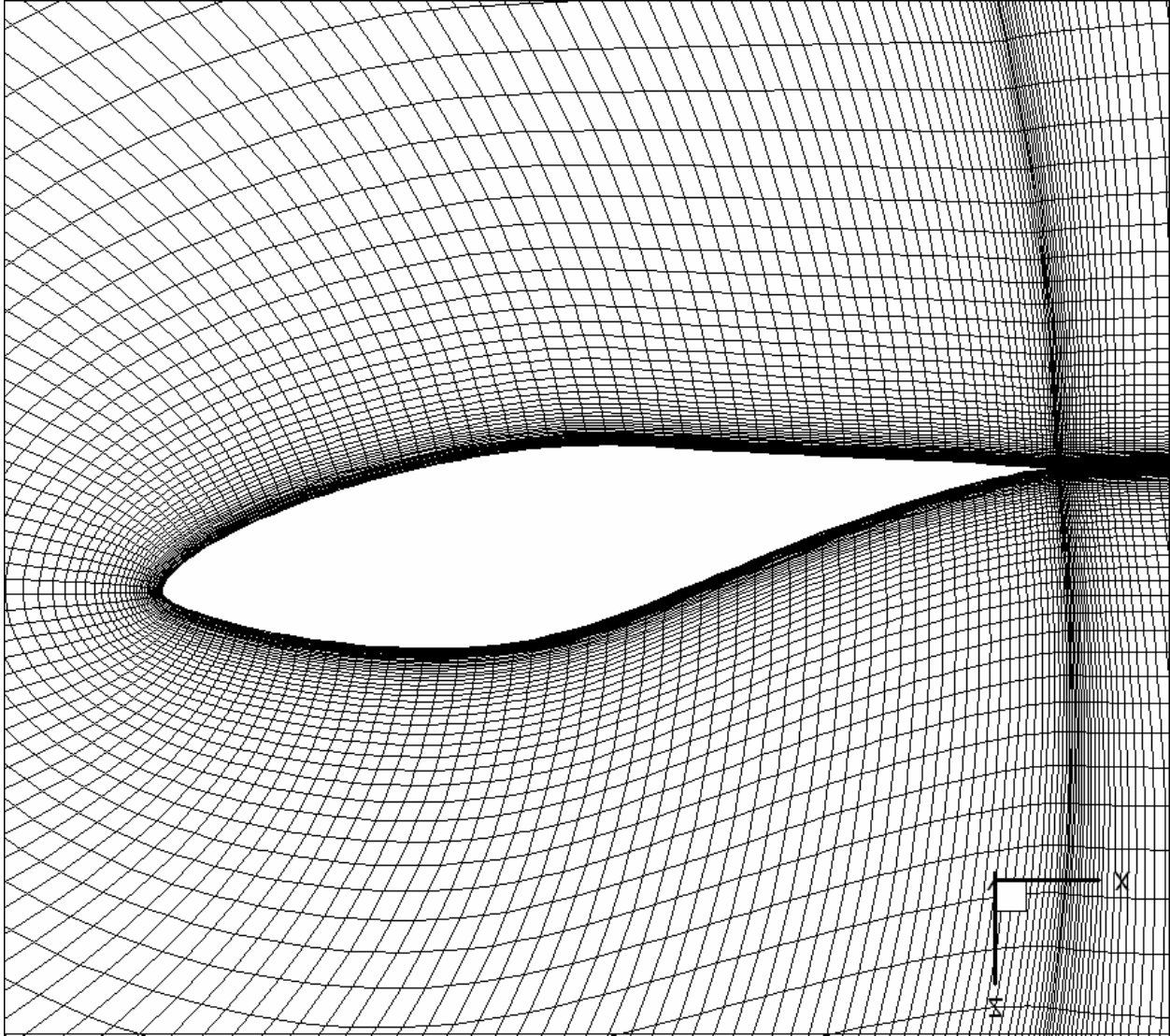


Figure 6.3 Close-up of area near the surface

6.1.4 CFL Number

Although the present simulations were done using constant time steps, CFL number was used to evaluate the grid quality and the optimal time step. The CFL number can be estimated from the following definition:

$$\Delta t = \frac{CFL}{|U| + |V| + |W| + a(|\nabla \xi| + |\nabla \eta| + |\nabla \zeta|)} \quad (6.1)$$

where U, V, W are contravariance velocities and ξ, η, ζ are coordinates in the transformed plane. The size of time step is set to be 0.01 degree/iteration.

It was found that the maximum CFL number was nearly the same on each wind speed case. This is due to the fact that the speed of sound is much higher than the wind speed and the grid speed. The highest CFL number is of the order of 100 in the area near the tip. At that location, the aspect ratio of the grid cell is high. However, a majority of the grid points (more than 95%) has a CFL number around 4 for the fine grid simulation (1.7 million grid points) and around 6 for coarse grid. Thus, these calculations yielded stable and time-accurate results.

6.1.5 Issues with Compressible Navier-Stokes Equations

The hybrid method implements the use of the compressible Navier-Stokes equations, which are applicable to high speed applications such as helicopters. However, its use in low speed applications such as wind turbines is questionable. In this study, the operation regime of the wind turbine is in the range of Mach number 0.1-0.2. This is high enough for the method to work properly in most areas. Some portions of the flow field show signs of inaccuracies such as abnormally high leading edge suction (as shown in the C_p distribution later in this chapter). These local errors did not significantly affect the load calculations in this study. Gleize [68] has studied the errors in the use of compressible solvers using the NACA0015 and Renaud [69] has studied these effects for a low Mach number the rotor-fuselage configuration. These authors recommend remedies such as use of a precondition matrix or the use of the incompressible Navier-Stokes Equations.

6.2 Grid Sensitivity Study

The study on the effect of grid density has been performed. Three grids: 100,000 cells, 400,000 cells, and 1,700,000 cells were used. Table 6.1 shows that CPU cost, and figure 6.4 shows the predicted torque as function of wind velocity. It was found the calculation converge to grid independent values as the number of cells increase from 400,000 to 1,700,000 (see figure 6.5). The 1,700,000 grid was used in all of the subsequence studies.

Table 6.1 Computational cost of each grid density

Turbulence model	Computational time per iteration	Total computational time	% difference from the baseline
Spalart-Allmaras Fine Grid	18.37	440,880	0
Spalart-Allmaras Coarse Grid	4.43	106,320	75.88

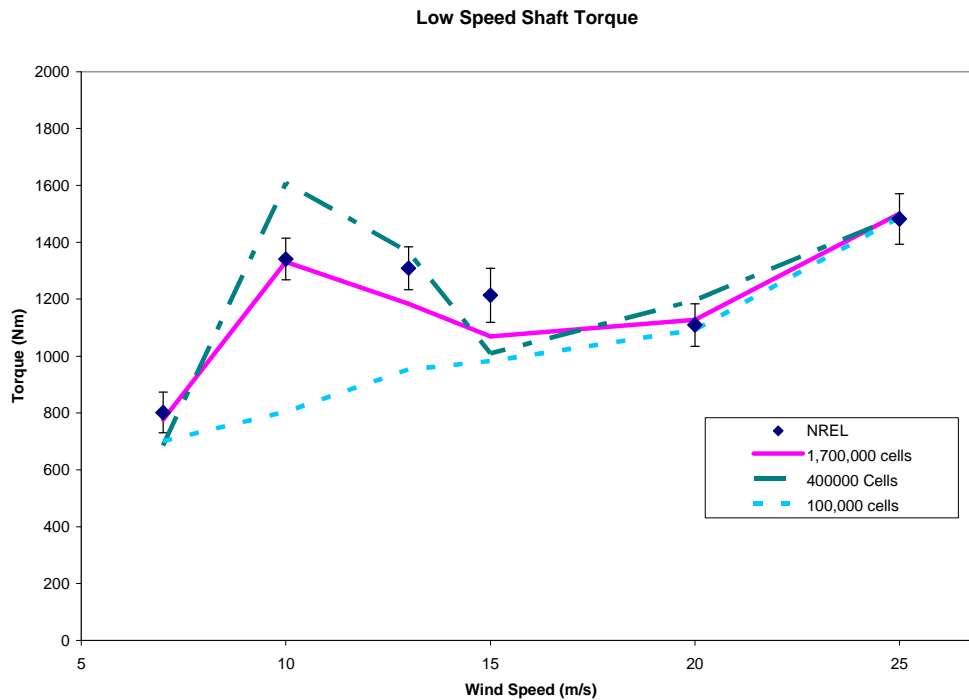


Figure 6.4 Effects of grid density on torque prediction

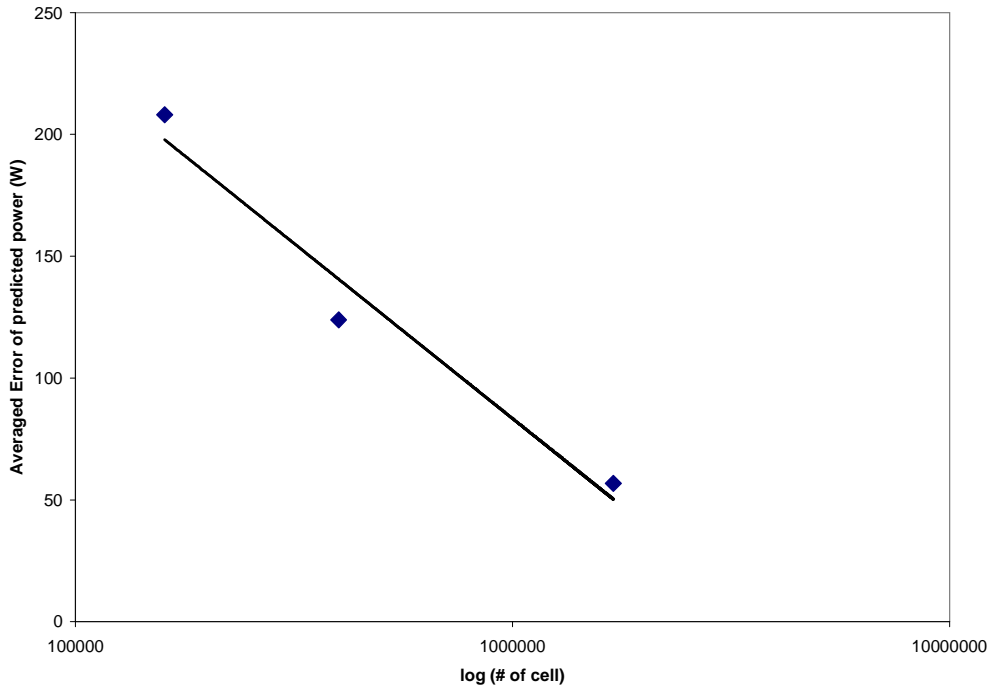


Figure 6.5 Effect of grid density on the power prediction error

6.3 Performance of the Advanced Turbulence Models

Wind turbine often operates in stalled conditions most of the time. Thus ability to accurately predict the extent of stall is crucial to predicting performance. The prediction of the turbulence viscosity in the current method depends on the use of correct turbulence models. In this work, several turbulence models have been studied, ranging from the zero-equation Baldwin-Lomax model to the DES. The Baldwin-Lomax and k-epsilon models are discussed in detail in [31],[32] and were found unsuitable. The turbulence models discussed in this dissertation are limited to the Spalart-Allmaras (SA) Model, SA-DES, and the k-omega SST model.

A wealth of experimental data is available for the validation. The performance data consist of low speed shaft torque, and the blade loads including the root flap bending moment,

and root edge bending moments. Force coefficients and pressure coefficients are also available at many span-wise locations.

6.2.1 Computational Cost

The computational cost on a machine with XEON 3.0GHz, 1 Giga Byte RAM for 1.7 million grid points is listed below in table 6.2.

Table 6.2 Computational cost of turbulence models

TURBULENCE MODEL	CPU TIME per Iteration (sec.)	Total CPU TIME (sec) (24,000 time steps)	COST OVER BASELINE (%)
Baldwin Lomax	14.875	357,000	0
Spalart-Allmaras	18.37	440,880	23.49
k-omega SST	28.79	690,960	93.55
SA DES	18.46	443,040	24.10

As expected, the higher order turbulence models require more computational resources than the lower order models. However, the DES variant of the SA model requires mostly the same resources as the baseline SA model. This is because the similarity between these two models.

The k-omega SST model, on the other hand, requires one more set of differential equations to be solved. As a result, the computational time increases compared to the other approaches.

6.3.2 Torque and Bending Moments

Figure 6.6 shows the low speed shaft torque predicted using SA, k-omega SST turbulence models and the SA-DES model. The error bars show the uncertainties in measured data at one standard deviation. The measurements were done at various wind speeds that can be classified as: low wind speed (7 m/s), intermediate wind speed (10 m/s, 13 m/s and 15 m/s) and high wind speed (20 m/s and 25 m/s) regimes. The calculations reproduce expected behavior of the stall regulated wind turbine over this speed range. In low wind speed regimes, power output increases with wind speed. In the intermediate wind speed regime, flow starts to separate over the blade to maintain the power output around the rated power of the generator. Power increases in the high wind speed regime due to phenomena that will be described later in the chapter.

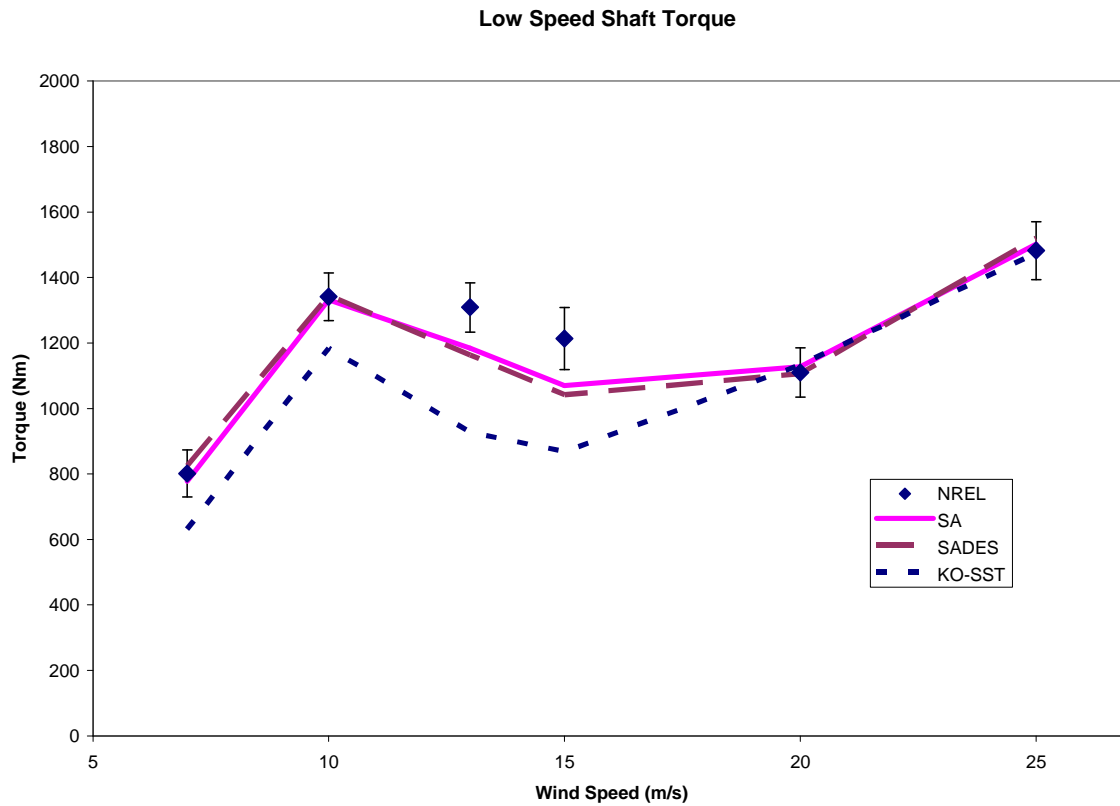


Figure 6.6 Effects of turbulence models on low speed shaft torque

Figures 6.7 and 6.8 show the root flap bending moment and root edge bending moment. Good agreement between wind tunnel data and calculations was formed for all turbulence models.

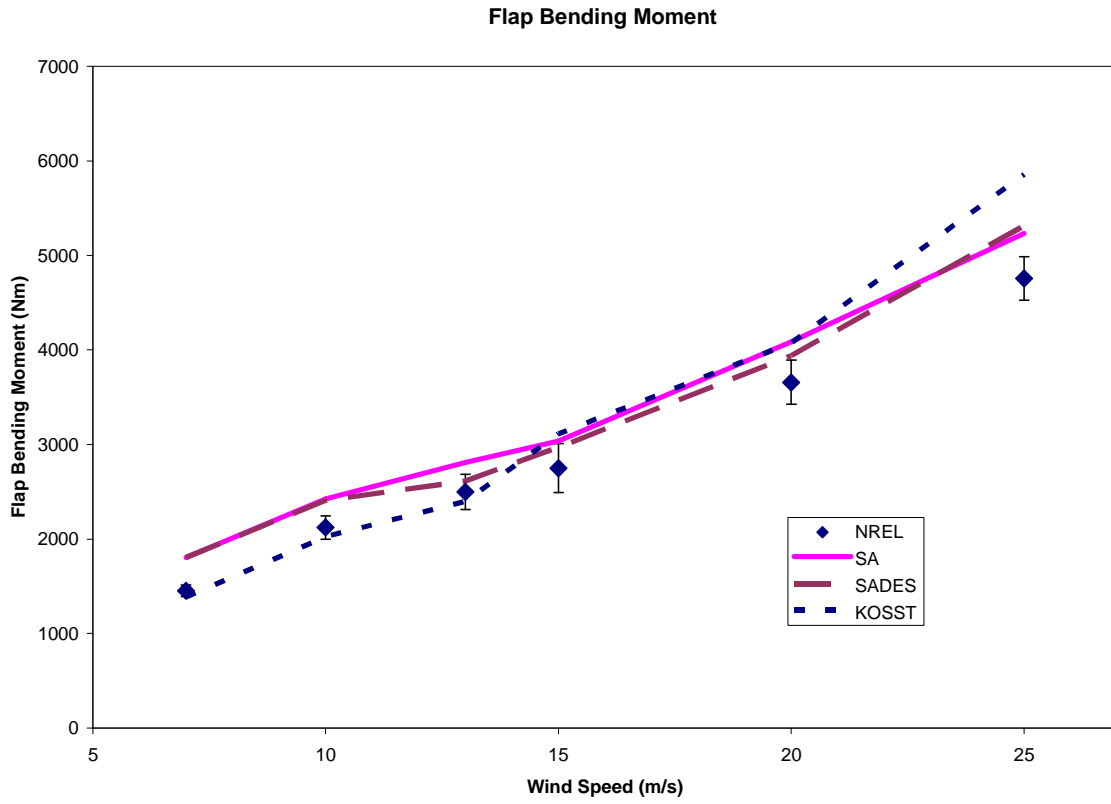


Figure 6.7 Effects of turbulence models on root flap bending moment

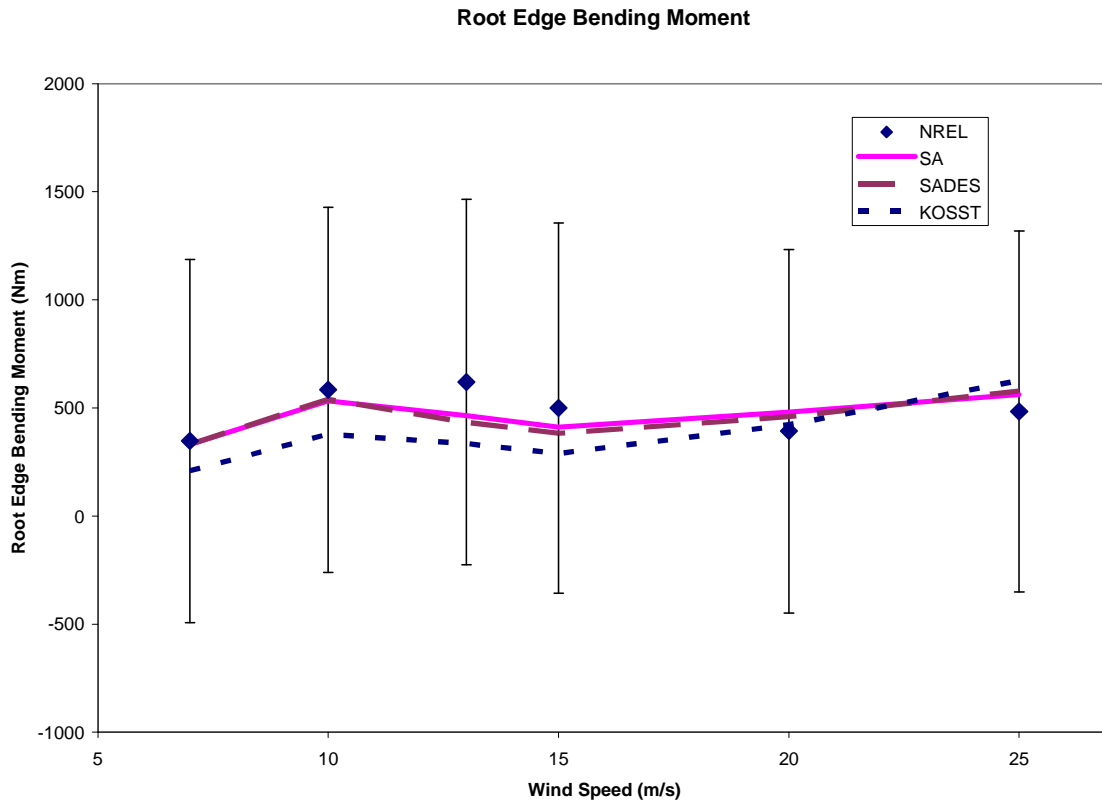


Figure 6.8 Effects of turbulence models on root edge bending moment

6.3.3 k- ω SST Model Issues

Contrary to expectations, the k- ω SST model performed poorly in this study. Work by Bardina, et. al. [70] provides a possible explanation. The authors have shown that two-equation turbulence models are very sensitive to the grid arrangement on the normal direction. According to Bardina, k- ω SST predict about 5% deviation of skin friction at y^+ is as small as 1.5 and the trend to predict worse result as y^+ increase. The current grid use y^+ of the order of 5, which is not sufficient for k- ω SST. Other researches e.g. Sorensen and Duque used y^+ around 1, and have reported good results.

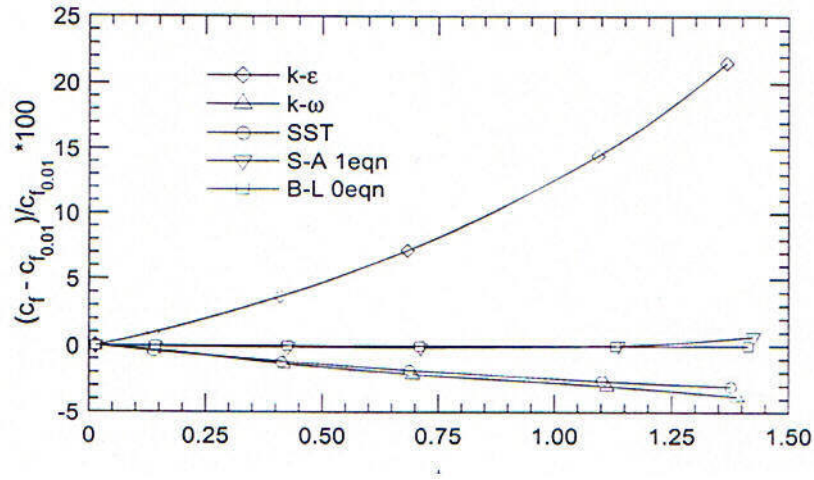


Figure 6.9 Sensitivity to the distance of the first point to the wall (from Bardina, et. al. 0)

Figure 6.9 also shows the SA model is less sensitive to the size of y^+ , possibly due to the inherent damping provided by the damping function (f_{v1} in equation 4.2). In contrast, the k-omega SST does not have a wall damping function. Furthermore, the process k-omega SST uses to transition from k-omega to k-epsilon might require a very fine grid in the normal direction in order to make a smooth transition. The grid used in this study is therefore inadequate for this turbulence model.

6.3.4 Force Coefficients

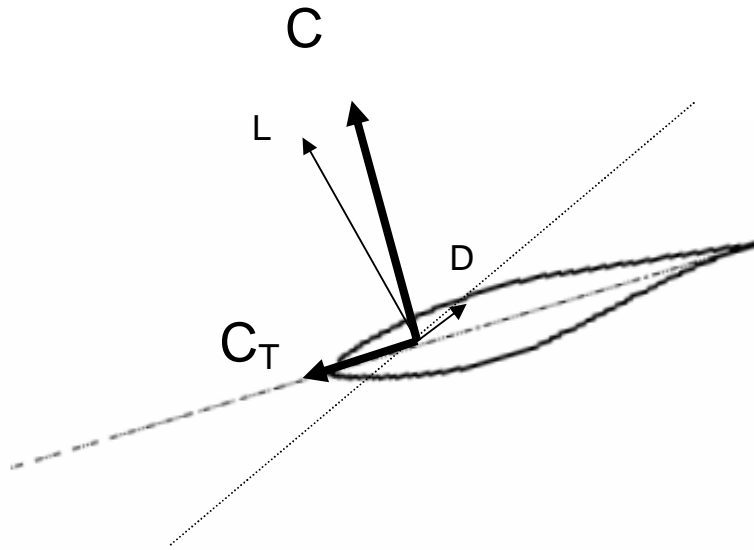


Figure 6.10 Force coefficient topology

The sectional normal and tangential force distribution were also measured in the test. Figure 6.10 shows the sign convention used. It should be noted that C_N is highly dependent on lift. At low speed, lift is relatively high compared to drag. The component of lift in the tangential direction is larger than the component of drag in the same direction, giving a positive value of C_T . Lift continues to increase with higher wind speed until stall occurs above a particular angle of attack. Once the separation occurs, lift decreases while drag suddenly increases due to the increase in pressure drag. This phenomenon results in smaller C_N and smaller or even negative C_T . This behavior is clearly seen in figures 6.11 and 6.12.

It is found that C_N predicted by SA and DES agree with the experiment. C_T deviates some from experimental data but still behaves as explained above. It should also be mentioned that the C_T value is very difficult to measure due to the sparseness of pressure taps in the leading and trailing edge regions. Due to the small size of C_T (only 1/10 of C_N), any small deviation in either

lift or drag can cause a significant error in C_T . However, these preliminary results show an improvement in prediction of both parameters (C_N and C_T) over our earlier results shown in Ref. [31],[32]

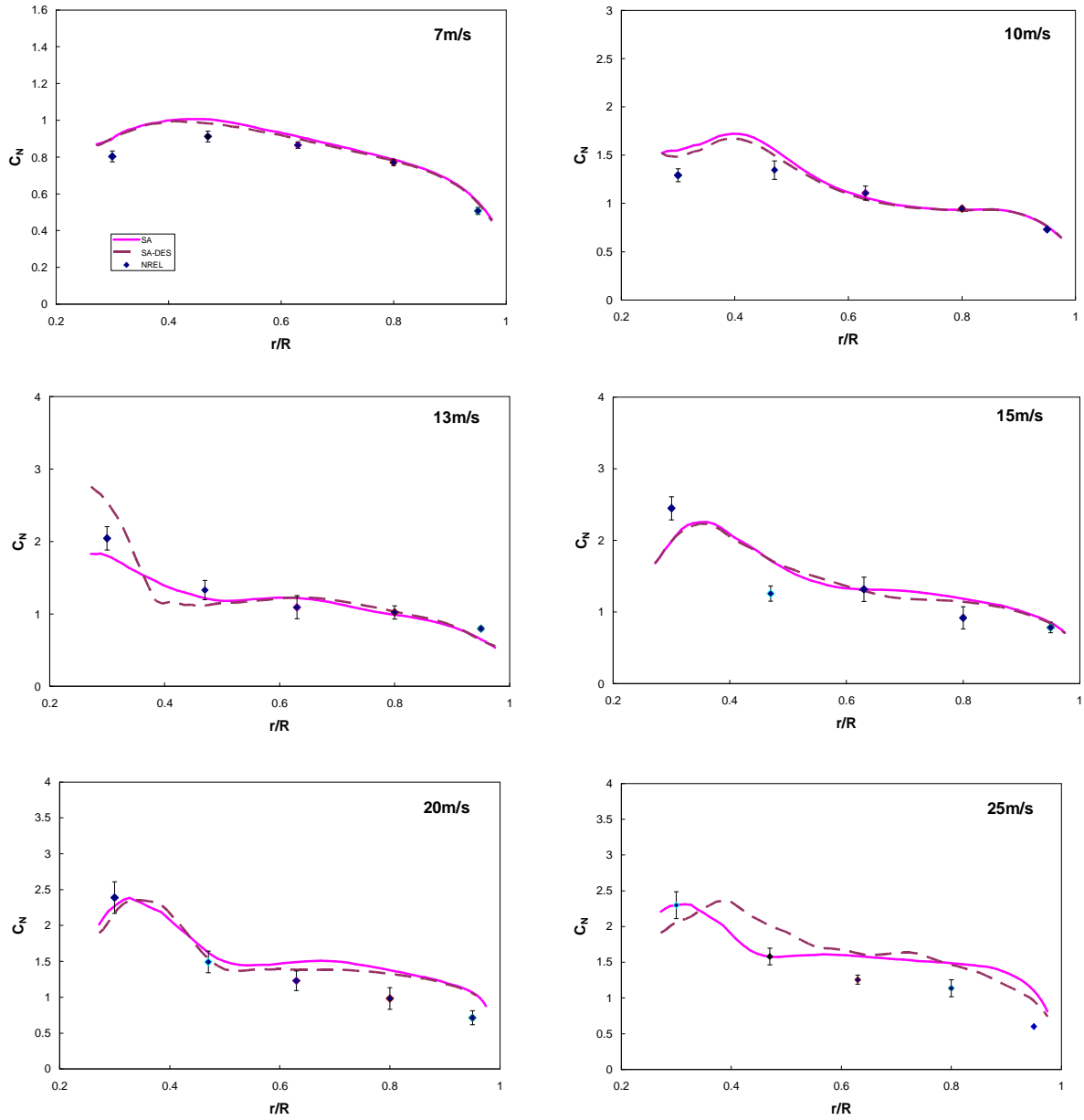


Figure 6.11 Effects of turbulence models on C_N distribution in the radial direction

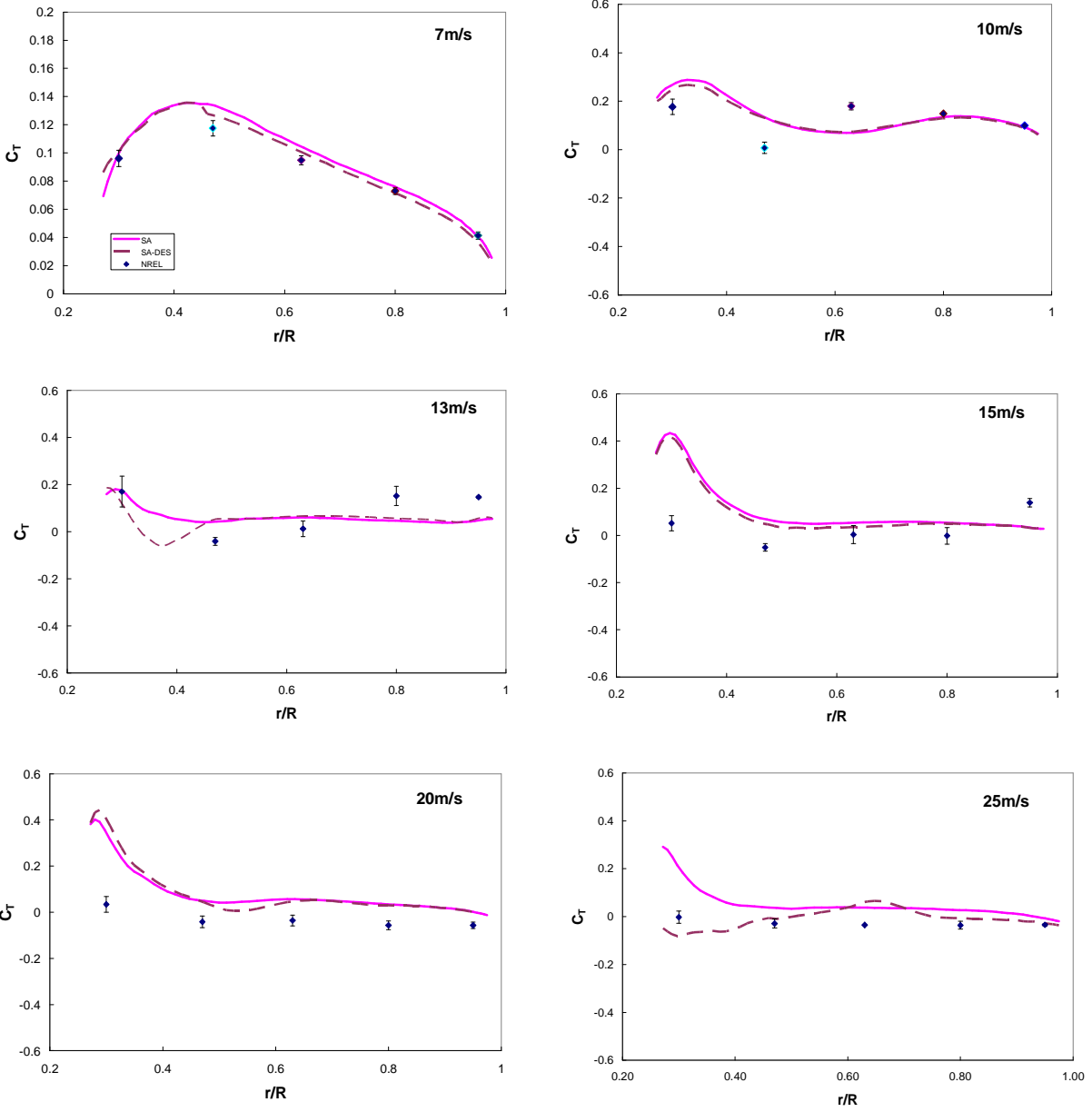


Figure 6.12 Effects of turbulence models on C_T distribution in the radial direction

The C_p distributions can give additional insight into the details of the flow around the blade sections. Figures 6.13 to 6.18 show instantaneous values of computational data against the ensemble average values of C_p from the experiment at the same azimuth angle. Only the SA and SA-DES results are shown, due to the sensitivity of the k-omega SST model to grid density as discussed earlier. The results at low wind speed (7 m/s, figure 6.13) show generally good agreement for each turbulence model. At this wind speed, the flow is completely attached.

The SA model and SA-DES both predicted the pressure coefficients on the upper surface to have increased suction compared to measurements. This C_p distribution results in higher force coefficients and consequently overpredicted torque and bending moments. This is likely due to underprediction of eddy viscosity near the leading edge.

Separation starts to appear at the inboard station at 10 m/s (figure 6.14) as the suction peak at $r/R=0.47$ disappears in the wind tunnel data. This coincides with the extremely low C_T at the same location shown in figure 6.12. A previous study by Sorensen [17] and Duque [19]) also does not predict the separation in that area. In this study, it was found that all turbulence models predict mild separation at $r/R=0.63$.

Figures 6.15 and 6.16 indicate greater deviation between our predictions and measurements in the inboard regions in the intermediate wind speed regime (13 m/s and 15 m/s).

The deviation is believed to be from two sources:

- a) The transition models were not activated (see section 6.4 for transition effect). The flow becomes turbulent well ahead of suction peaks. This causes the flow downstream to be less prone to separation.

b) Even if the transition is correctly predicted, the level of eddy viscosity in the flow will determine turbulent boundary layer growth and eventual turbulent separation. The leading edge suction is tied to both boundary layer growth and separation phenomenon.

At 20 m/s, our predictions generally showed separation over the entire rotor as observed in experiments. However, there are suction peaks present in all spanwise stations, but the peaks rapidly collapse as the separation line progresses towards the leading edge. The effect of these suction peaks has comparatively small effects on C_N and C_T and consequently the torque and bending moments.

At 25 m/sec wind speed (figure 6.18), both the measurements and the predictions indicate a fully separated flow at the leading edge, as seen by the absence of a suction peak in the experiment and in the flow field of our simulation. The present simulations indicate separation to occur just downstream of the leading edge. The small attached flow upstream did give rise to a suction peak particularly near the tip. This also increased the normal forces near the tip as seen in figure 6.11.

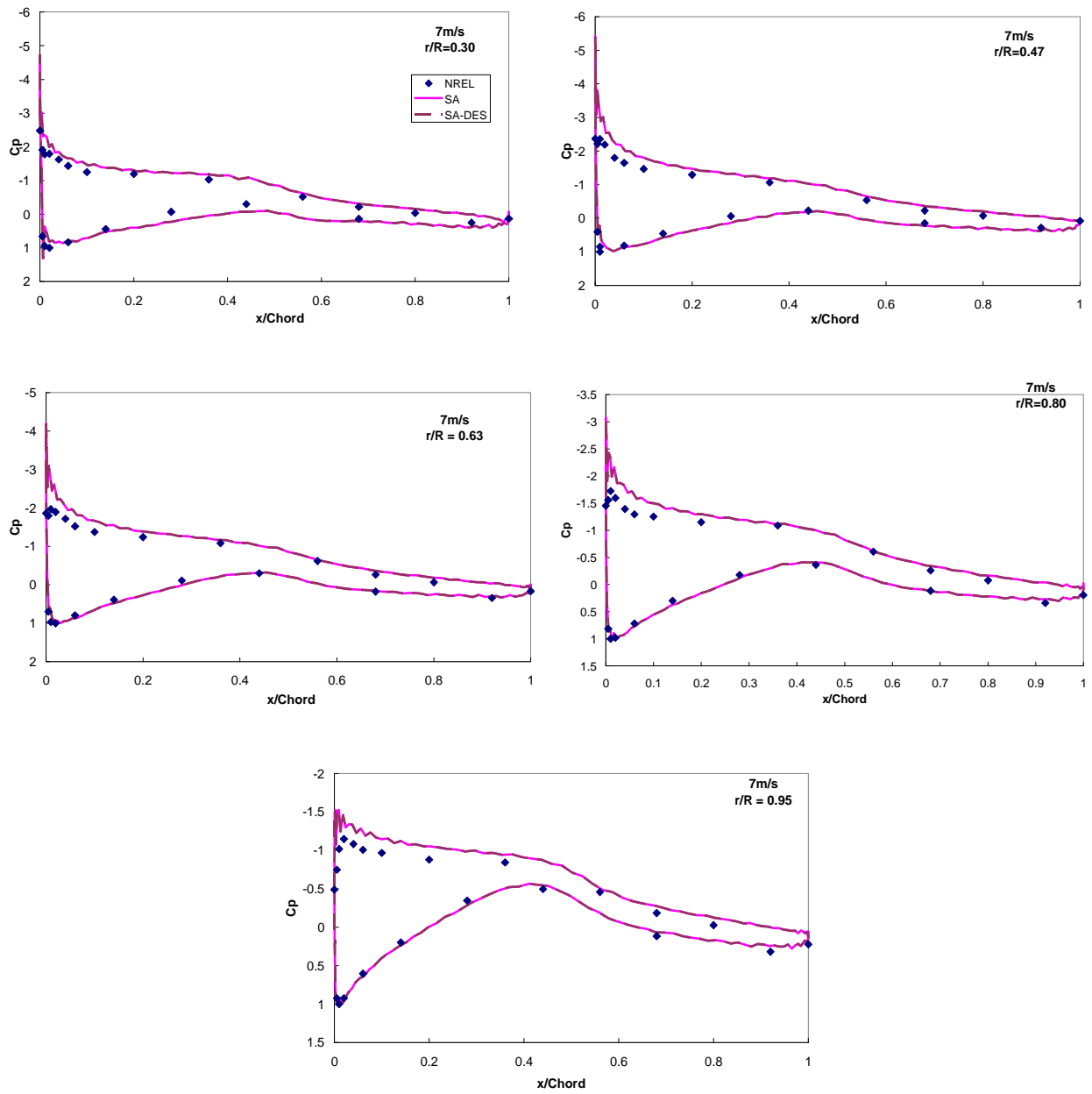


Figure 6.13 Effects of turbulence models on C_p distribution in the radial direction at 7 m/s

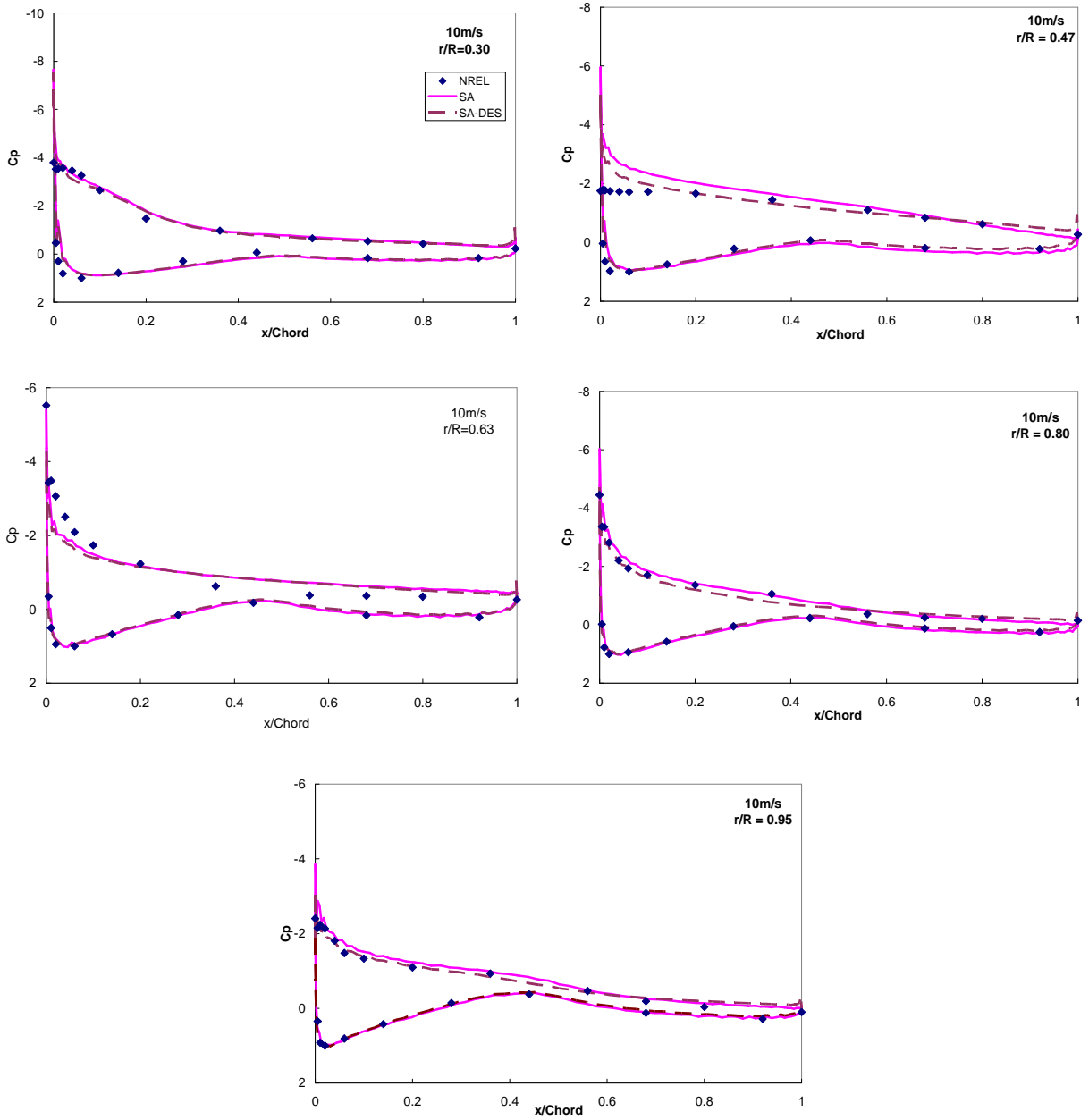


Figure 6.14 Effects of turbulence models on C_p distribution in the radial direction at 10 m/s

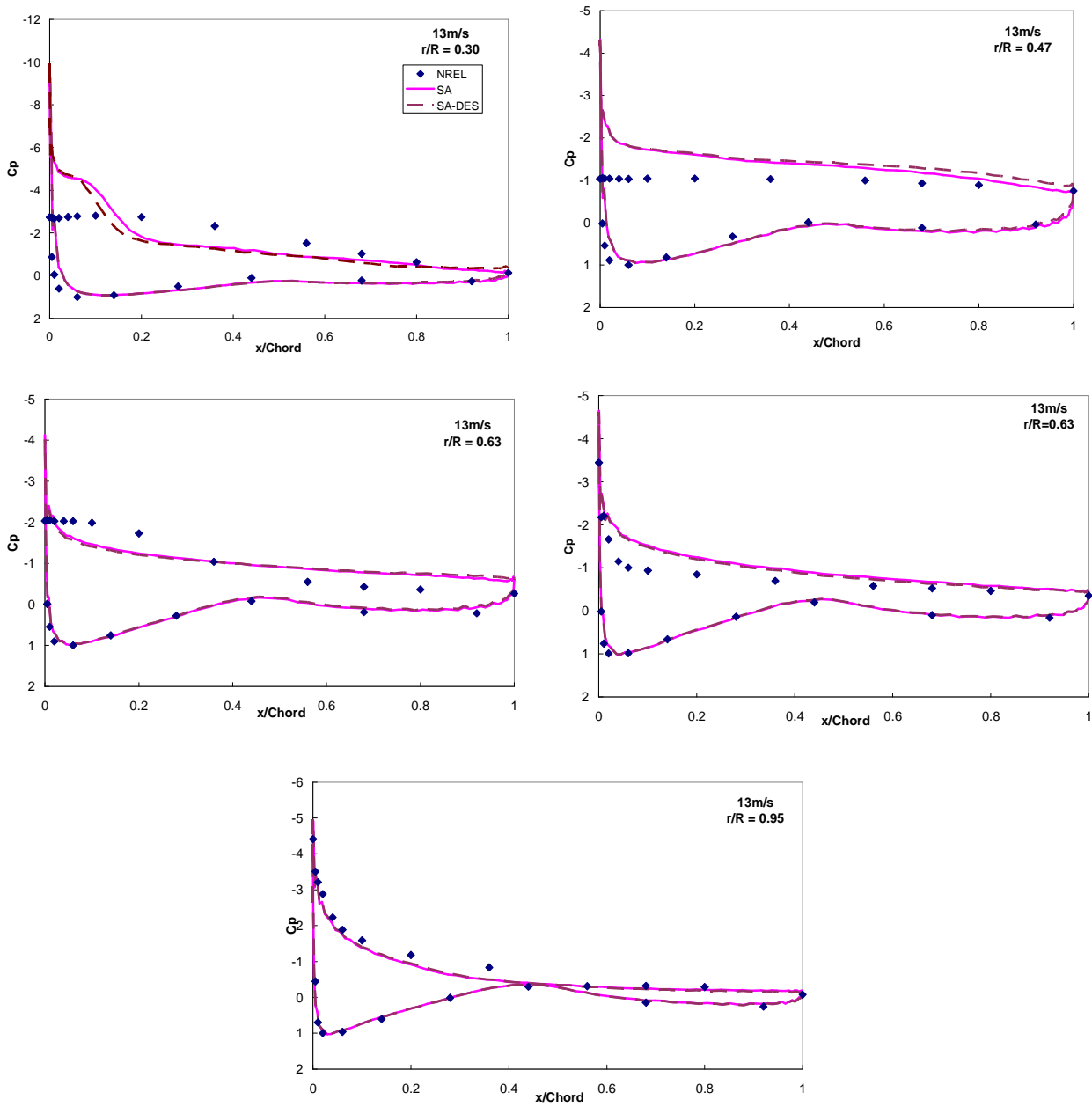


Figure 6.15 Effects of turbulence models on C_p distribution in the radial direction at 13 m/s

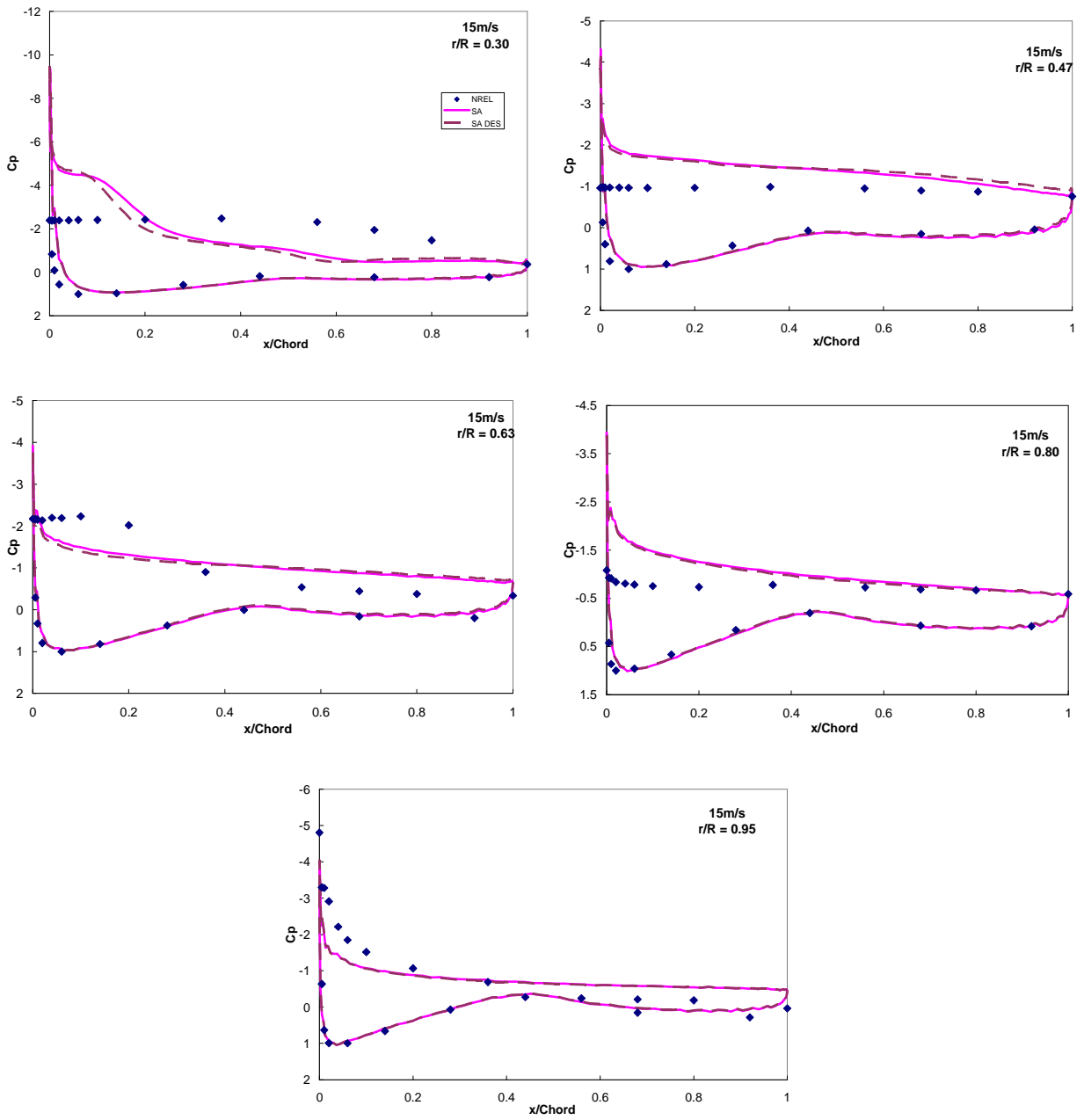


Figure 6.16 Effects of turbulence models on C_p distribution in the radial direction at 15 m/s

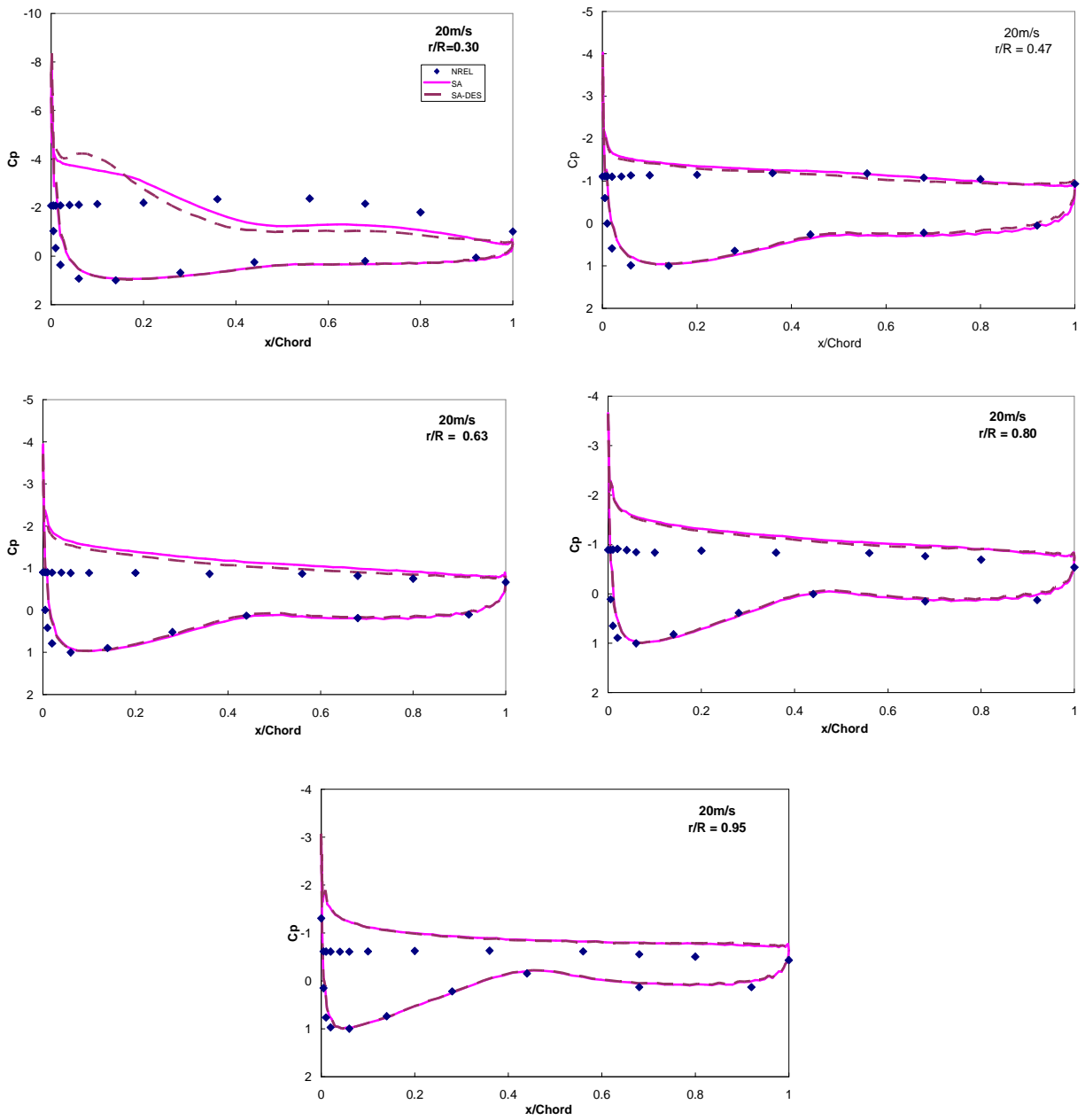


Figure 6.17 Effects of turbulence models on C_p distribution in the radial direction at 20 m/s

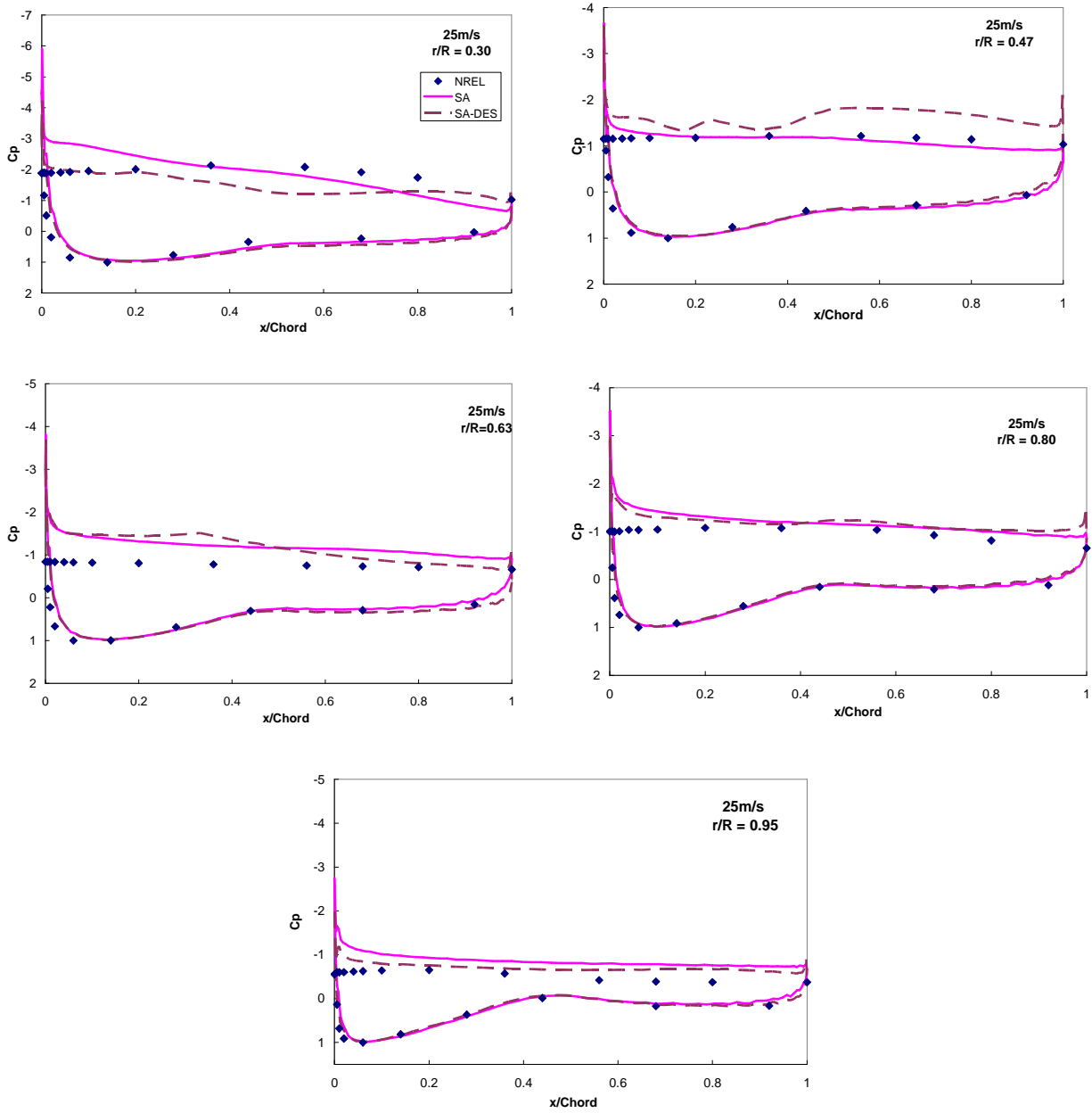


Figure 6.18 Effects of turbulence models on C_p distribution in the radial direction at 25 m/s

6.4 Effect of Transition Models

As a part of this work two existing transition models, one due to Eppler, and the second based on Michel were tested. The mathematical formulation behind these models is given in Chapter 3. The simulations were compared with fully turbulent flow predictions. SA model was used in this study.

6.4.1 Computational Cost associated with the Transitional Models

These two transition models do not have any significant impact on the computational resources, in terms of CPU time and memory usage. The computation uses only the local information such as Reynolds number based on distance from the leading edge, momentum thickness, and shape factor. These quantities are readily calculated from the flow field at each time step.

6.4.2 Force Coefficients

For a majority of the calculations, wind speed (7m/sec to 25m/s), at most radial locations, the calculations predicted a suction peak very close to the leading edge. This triggered local laminar separation in the transition models (which use $\Theta^2 \frac{du_e}{dx}$ as an empirical parameter to detect separation). Since these models, in our implementations, assume that the flow transition immediately to turbulent flow near the leading edge. This caused the predictions for integrated C_N and C_T loads to be very close to fully turbulent flow (See figure 6.19).

At some radial locations, particularly in area of 30% R, leading edge separation was not detected. In this case, transition occurs when the local pressure gradient becomes adverse on the upper and lower surface (around 50% chord- see figure 6.21). This caused local thickening of the boundary layer and triggered transition.

The thinner boundary layer upstream of the 50% chord with these turbulence models, produced slightly more circulation over these section compared to the fully turbulent case which had a thicker boundary layer. This explains in part the difference in the pressure distribution and integrated loads.

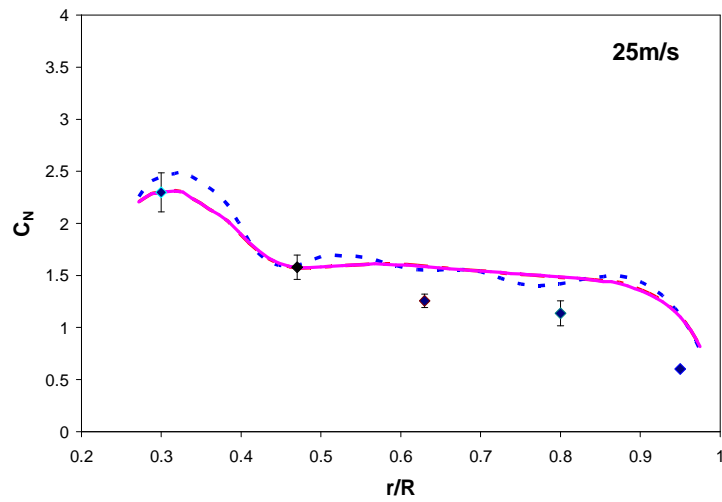
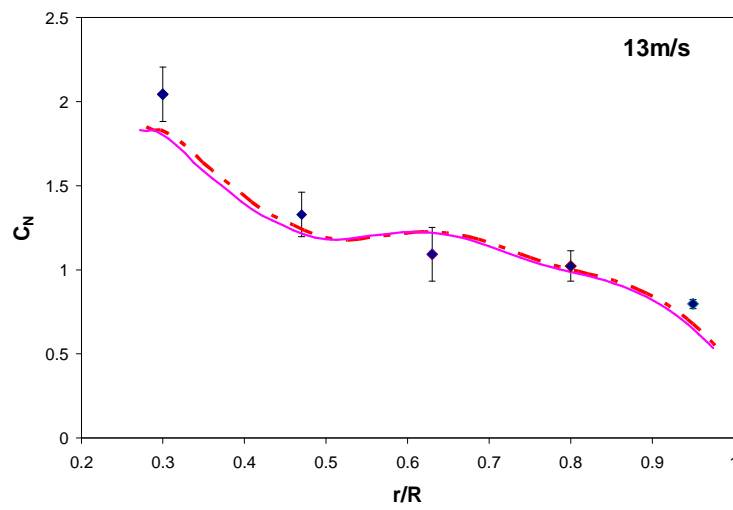
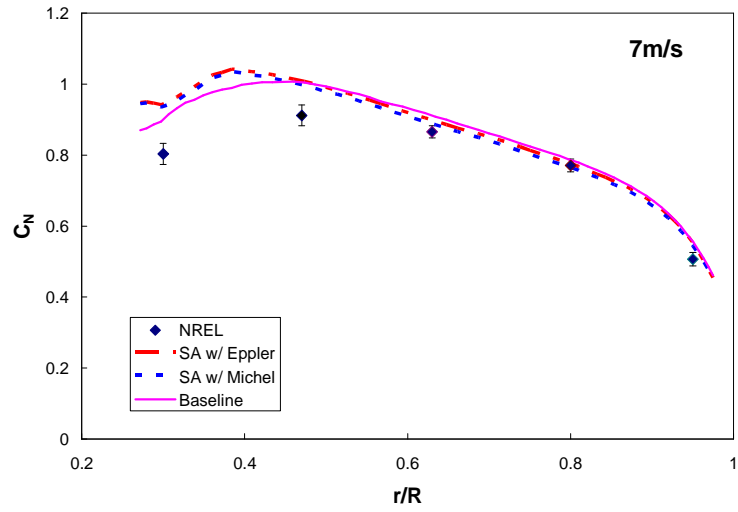


Figure 6.19 Effects of transition models on C_N distribution in the radial direction

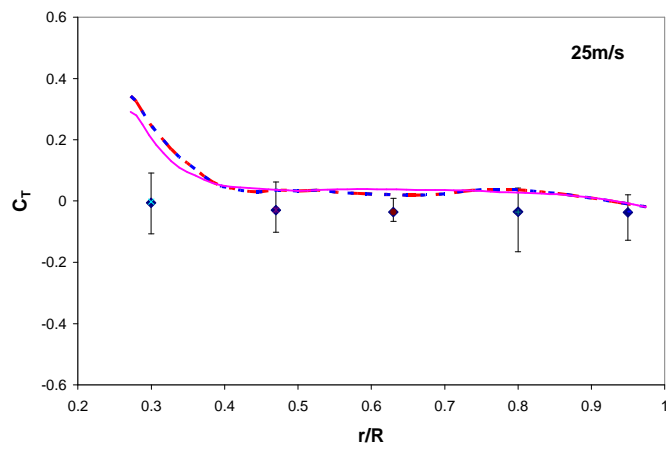
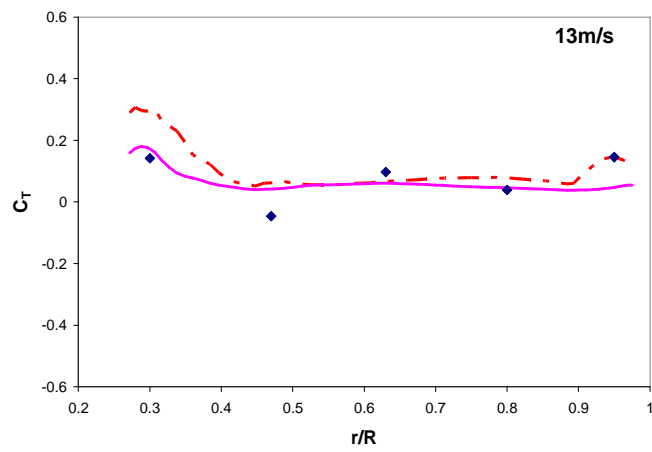
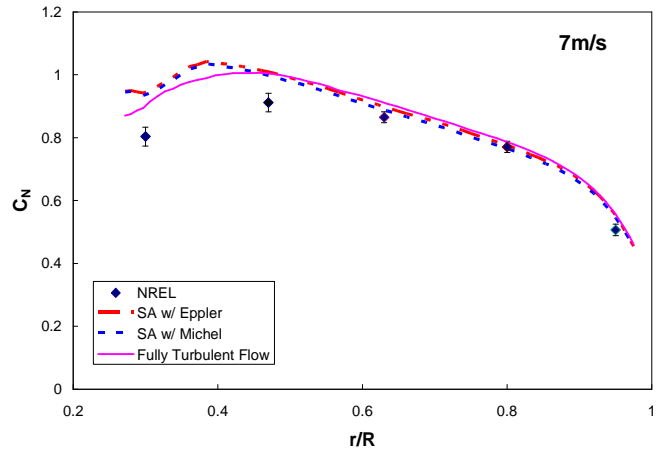


Figure 6.20 Effects of transition models on C_T distribution in the radial direction

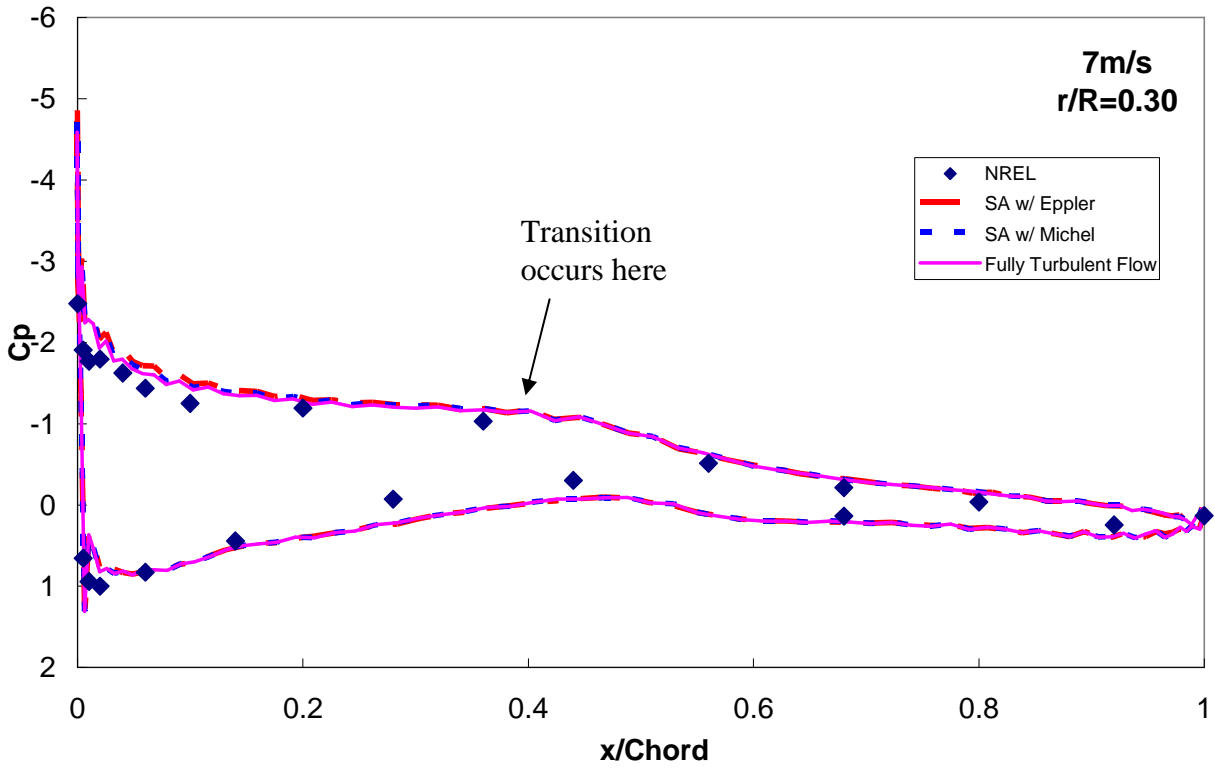


Figure 6.21 Effects of transition models on C_p distribution in the radial direction at 7 m/s

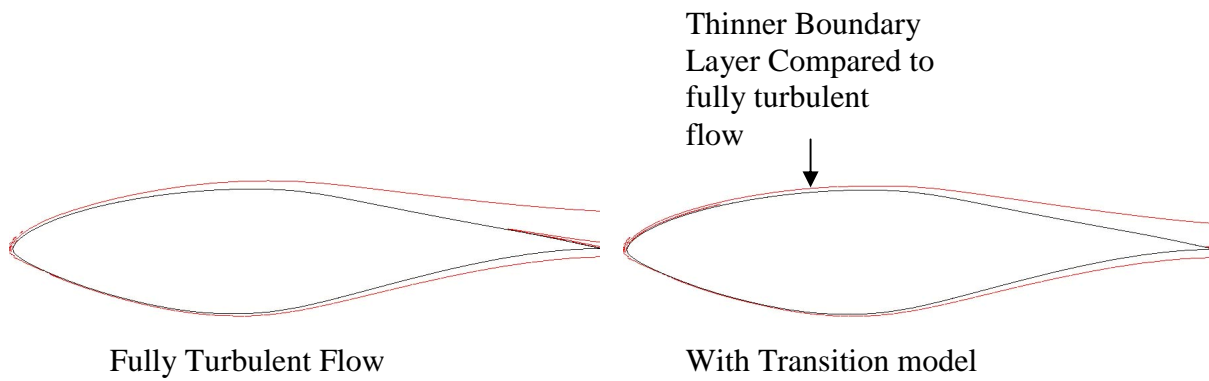


Figure 6.22 Effects of transition models on boundary layer thickness at 30% Chord and 7m/s

CHAPTER 7

CONCLUSIONS AND RECOMENDATIONS

A first-principles based method for modeling horizontal axis wind turbine configurations has been developed. As part of this work, several state of the art turbulence models have been evaluated. The effect of transition models has been studied. Grid sensitivity studies have been done to assess the sensitivity of the calculations to grid spacing, particularly in the boundary layer, and the stretching ratio. Low speed shaft torque, bending moments, force coefficients, and pressure distributions from wind tunnel tests have been compared against computational data.

Based on these studies, the following conclusions can be drawn:

1. A “fine” grid (~1,700,000 cells) with y^+ values for the first point off the wall below 5 was required for reliable power prediction, although initial engineering studies can be done with 400,000 cells. It was found that grid aspect ratio in the radial direction should be small to avoid instabilities, particularly near the tip and over the wake cut. A grid spacing ratio of 2,000:100:1 (streamwise, radial, and normal) was found desirable. Use of thin layer Navier-Stokes equations was found to relax this requirement and allow larger spacing in the streamwise and radial direction.

2. For the S809 airfoil, with a relatively small leading edge radius, the calculations revealed that local laminar separation occurred in the immediate vicinity of the leading edge and caused the boundary layer to be tripped. As a result, the calculations were insensitive to transition model. 2-D simulations by other researchers, and the present author, indicate that at low α , the flow may remain laminar up to 50% chord if the leading edge suction peak is attached and does not transition to turbulent. In the present study the effective α often exceed 7° , causing leading edge transition to turbulent. Further work is needed to systematically study and develop transition model that do not use laminar separation bubble as one of the transition criteria.

3. While the turbulence models studied here (SA, SA-DES, k-omega SST) all provided reasonable estimates (to within 10%) for torque, root bending moment, sectional forces, and surface pressure distributions, the SA-DES method performed best on the finest grid (1.7 million per blade) tested to date. The DES version, as expected, influenced the results only when the shear layer detached from the blade surface at high wind speed or high effect α , otherwise, SA and SA-DES produced comparable results.

Based on the calculations, the following points are recommended for further study.

1. All the simulation reported here were done on a single processor PC. For finer grids and engineering design, a distributed processing capability is needed. The

present approach lends itself to distributed simulations if the flow field is divided into blocks, or multiple blades are simultaneously modeled. It is recommended that this code be modified to take advantage of recent progress in distributed computation techniques.

2. The simulations here were done in the time-accurate mode with constant Δt to capture time dependent phenomena. For engineering analyses, where often only steady state results are of interest, use of dual time step methods (rather than the current single-step LU-SGS method) can significantly speed up convergence [].
3. Both active (e.g. circulation control) and passive (e.g. gurney flap) ways of enhancing power production at low and high wind condition must be explored.
4. Because the flow is predominantly incompressible matrix-preconditioning must be explored as a way of obtaining true “incompressible” result free of local oscillations in surface pressure near the leading edge. Low-Mach preconditioning is also expected to improve convergence rate.
5. For downstream wind conditions, tower effects will be significant. A version of this approach that models tower effects using overset grids exists, and needs to be updated with the turbulence models and improved algorithms implement here.

6. There has been a growing interest in the development of large diameter wind turbine with light weight tower and blades. It will be necessary to include these effects in the analysis and perform associated structural load calculations. This approach is well suited for use in conjunction with comprehensive aero elastic methods such as RCAS and DYMORE. Aeroelastic simulations are recommended.

It is hoped that this work will serve as a stepping stone for further research in the exciting world of wind turbines, and for the design and modeling of next generation configurations.

APPENDIX A

VALIDATION OF TURBULENCE MODELS

The present methodology while customized for wind turbine, can also model fixed wings and airfoil section. The validation of turbulent models has been done by computing viscous flow over of the S809 airfoil using the same solver. The airfoil used is the same as in phase VI rotor, and hence the best choice for validation of hybrid methodology for phase VI rotor application. The tests were done in the Delft University of Technology's 1.8m x 1.25m wind tunnel. A similarly sized model was also tested at Ohio State University. The results were identical. The results of these tests were first reported by Somers [35] and later discussed and compared with numerical simulation by Wolfe [71] The data used in this validation is digitized from the latter.

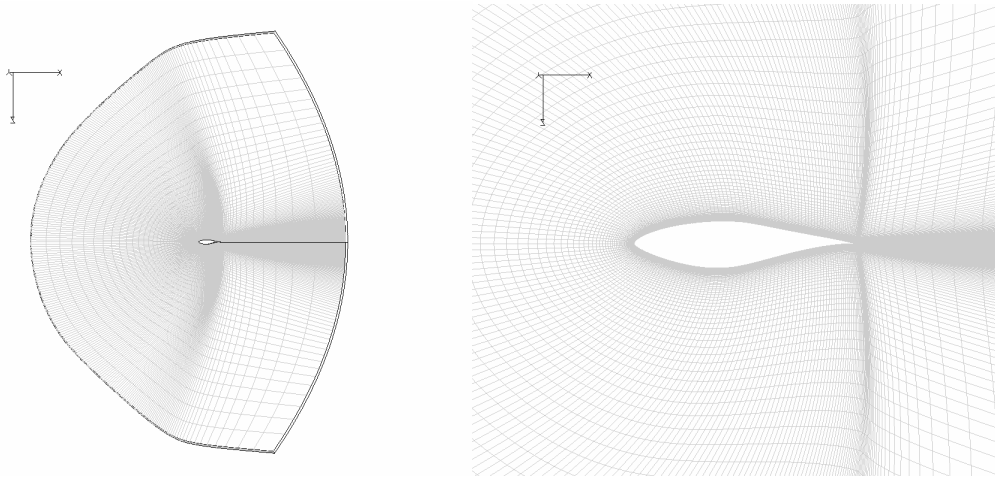


Figure A.1 Grid used in the turbulent models validation

This validation used the same C-grid topology (shown in figure A.1) as in the rotor study. It was also created by the same grid generation method. However, it contains

more points along the chord and in the normal direction. It has 257 grid points in the wrap around direction and 129 points in the normal direction but only 5 points in spanwise direction. This is the minimum number of spanwise points that allows 3rd order Roe scheme to be used with no changes. The flow, of course, has not spanwise gradient. The y^+ is set to be less than one and there are more than ten points inside the boundary layer allowing a more accurate prediction of turbulent viscosity in the boundary layer.

This validation focused on both Spalart-Allmaras (SA) and k-omega SST turbulence models, and the DES method. The validation has been done by comparing the C_p , C_l and C_d values available from the wind tunnel data. The calculation of these coefficient were done using the same subroutine as for Phase VI rotor study.

Numerical Results

All calculations were made at a Reynolds number of 2×10^6 to match measurements. The calculations were carried forward for 18,000 time steps to ensure the convergence of the results. The size of time step is set such that the CFL number is of the order of 5 or less. Fully turbulent flow was assumed. The eddy viscosities were very low over the first 50% of the chord indicating that the flow is nearly laminar over the favorable pressure gradient region

Figure A.2 shows the convergence history of the normal force (C_N) at two angles of attack. The convergence of the loads at the higher attack case takes much longer time than for the lower angle of attack.

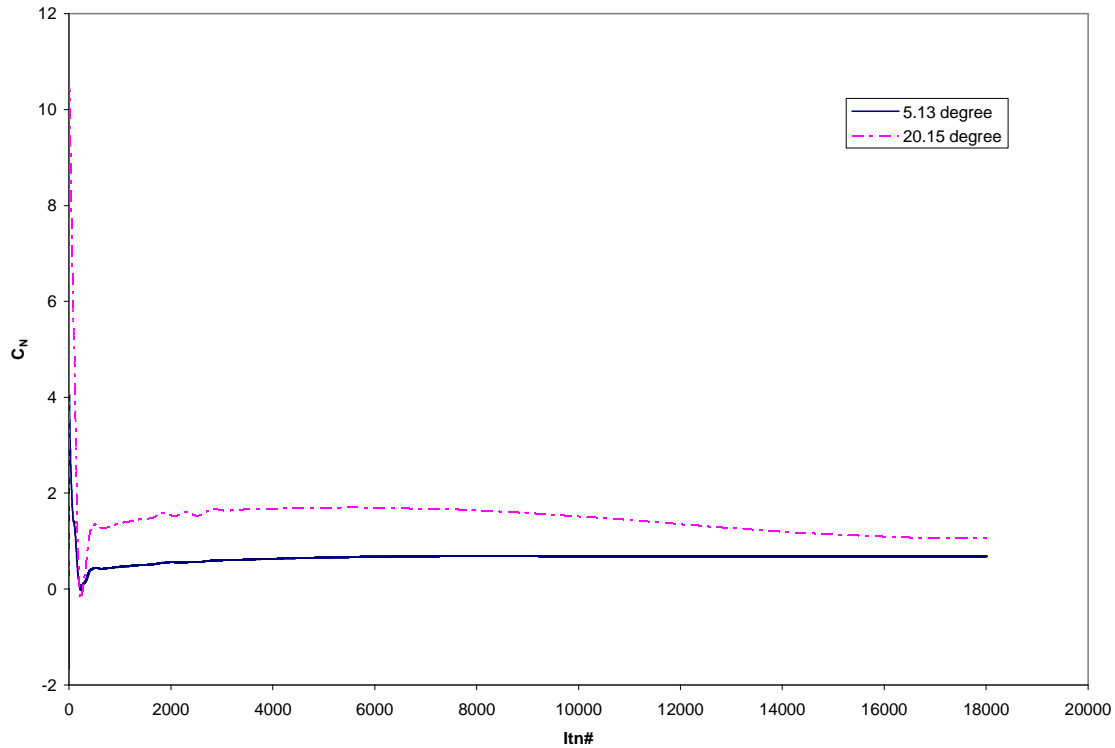


Figure A.2 Grid used in the turbulent models validation

Figures A.3 through A.8 show comparisons between calculated and experimental surface pressure distribution (C_p) for angles of attack: 0° , 1.02° , 5.13° , 9.22° , 14.24° and 20.15° respectively. The C_p distribution show reasonably good agreement over the entire airfoil surface up to 14.22° . It should be noted that the small discrepancy around the mid chord of 0° to 5.13° cases were likely due to the presence of laminar separation bubble, which was not resolved.

The C_p prediction from SA model and SA DES are almost identical. This is because DES is activated only in free shear layers. The turbulent viscosity in the free shear layer was small compared to the values within the boundary layer. This results in and almost identical turbulent viscosity distribution within the wall bounded shear layer and, as a consequence, identical pressures. On the other hand, the k-omega SST model predicts a bit higher turbulent (figure A.9) viscosity on the upper surface of the airfoil,

which produced a somewhat thicker boundary layer over the upper surface and lead to lower suction levels.

The advantage of DES method over conventional turbulence models can clearly be seen in figure A.8. While SA model duplicates the results by Yang, et al [72], and Wolfe [71] (not shown for clarity) and while k-omega SST provides a marginal improvement, the SA DES method gives very good agreement with measurements. At this particular angle of attack, flow over the airfoil is massively stalled, and proper estimates of eddy viscosity in the free shear layer (as done by the DES) become important (figure A.10).

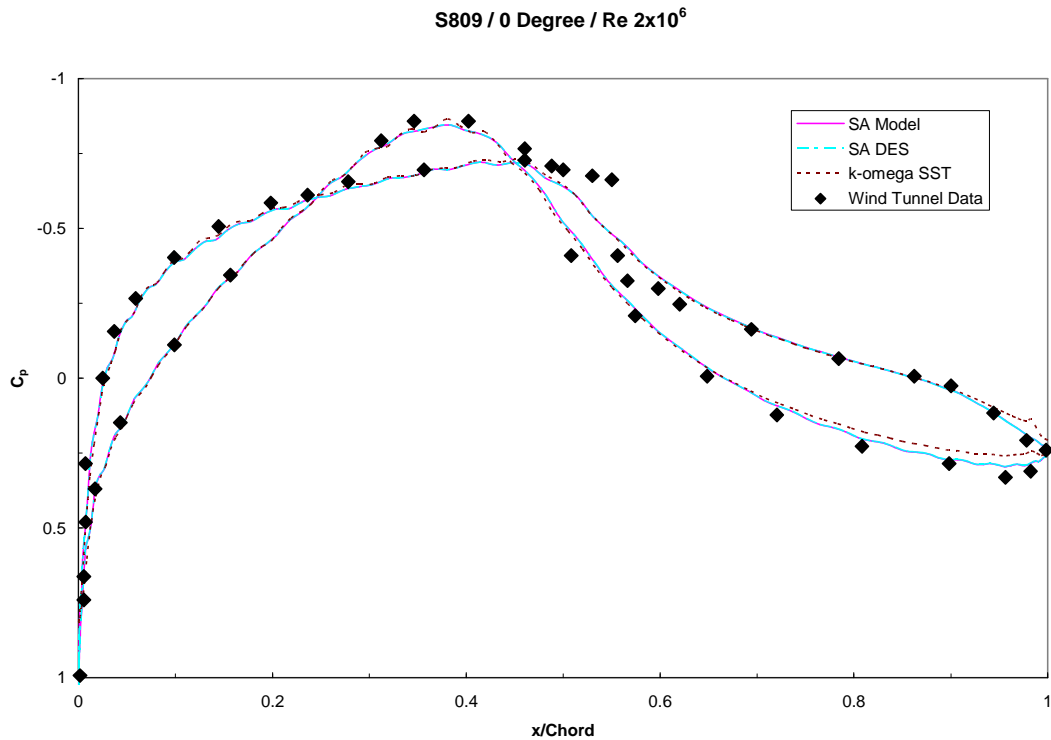


Figure A.3 Pressure Distribution for Angle of Attack = 0 degree, Fully Turbulent Calculation

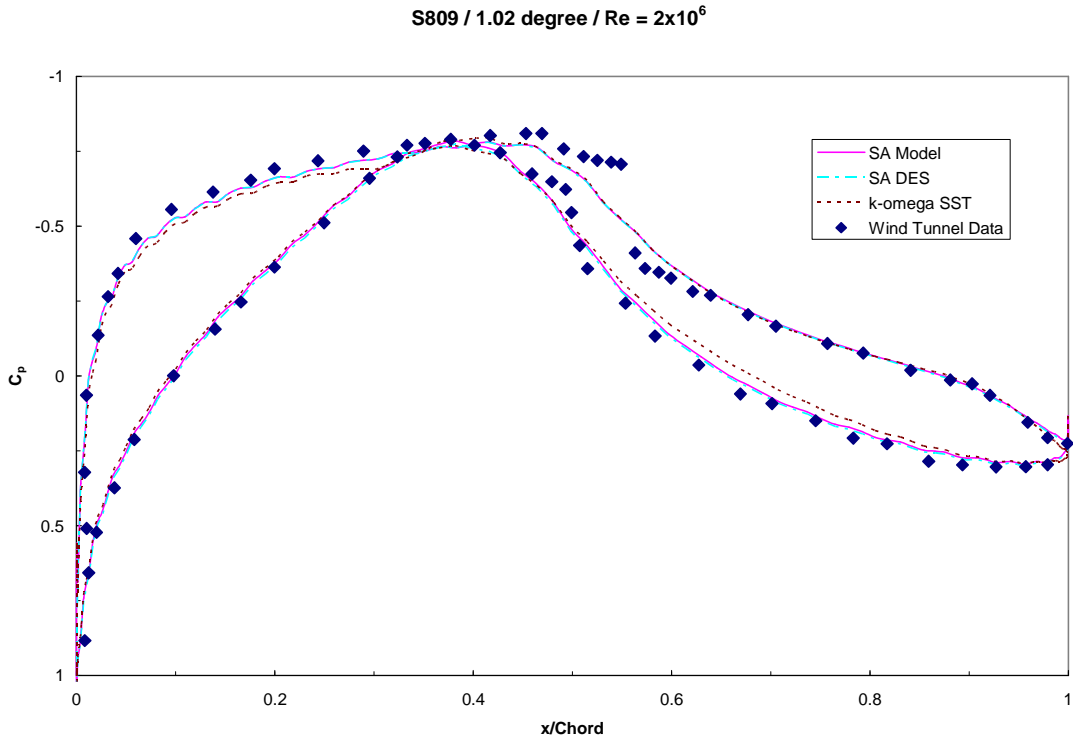


Figure A.4 Pressure Distribution for Angle of Attack = 1.02 degree, Fully Turbulent Calculation

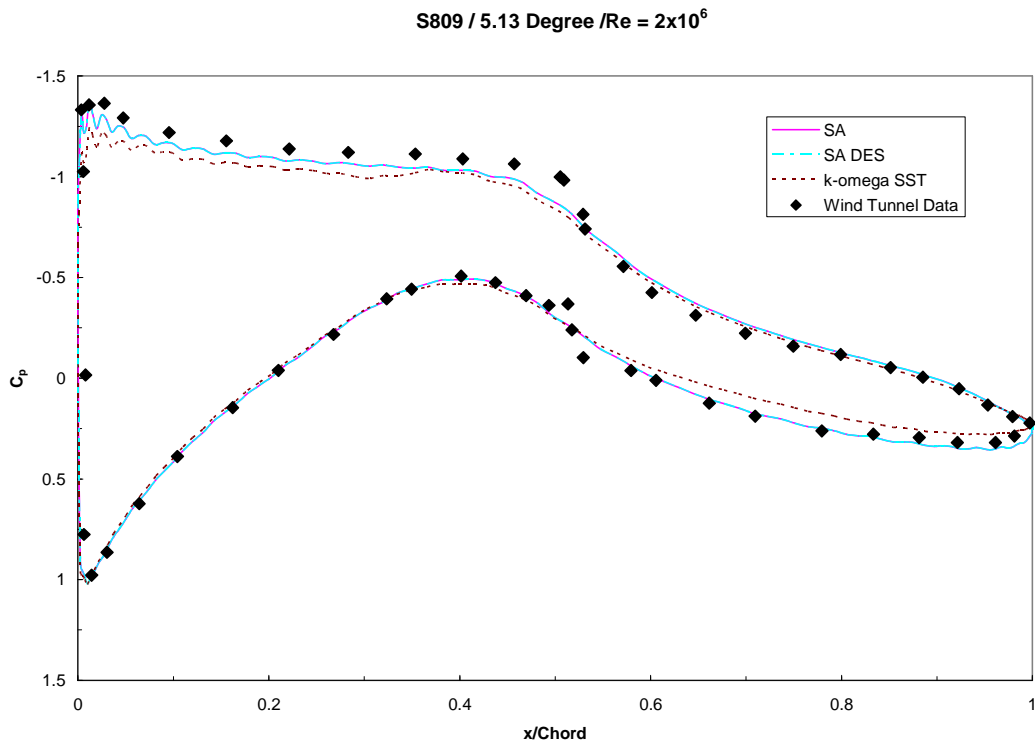


Figure A.5 Pressure Distribution for Angle of Attack = 5.13 degree, Fully Turbulent Calculation

S809 / 9.22 Degree / Re = 2x10⁶

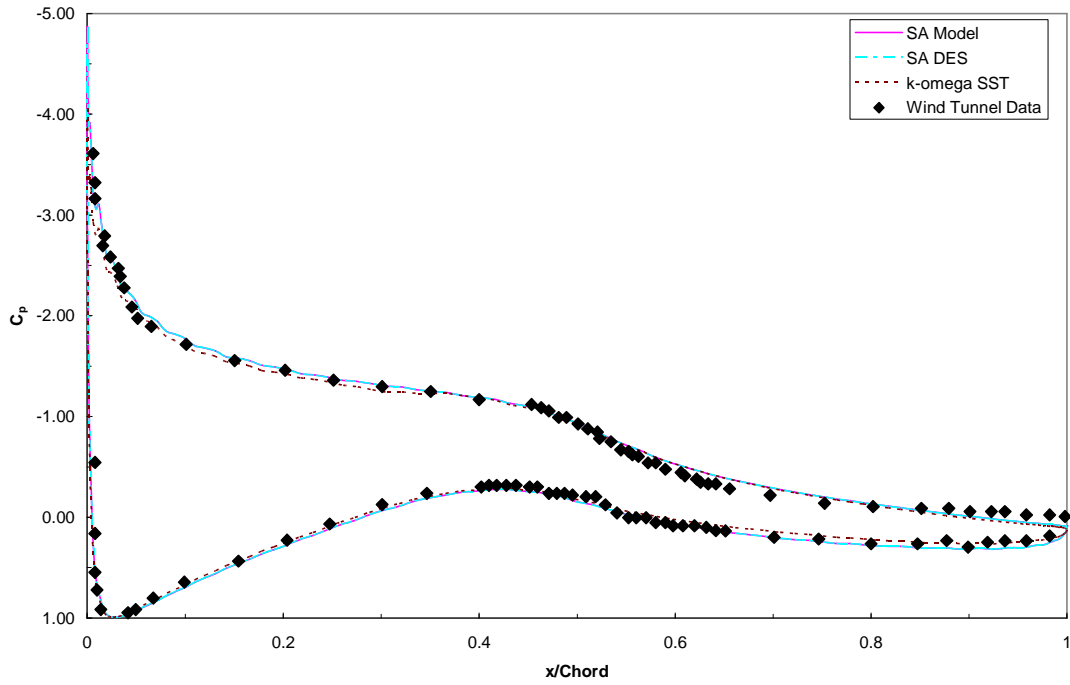


Figure A.6 Pressure Distribution for Angle of Attack = 9.22 degree, Fully Turbulent Calculation

S809 / 14.24 degree / Re = 2x10⁶

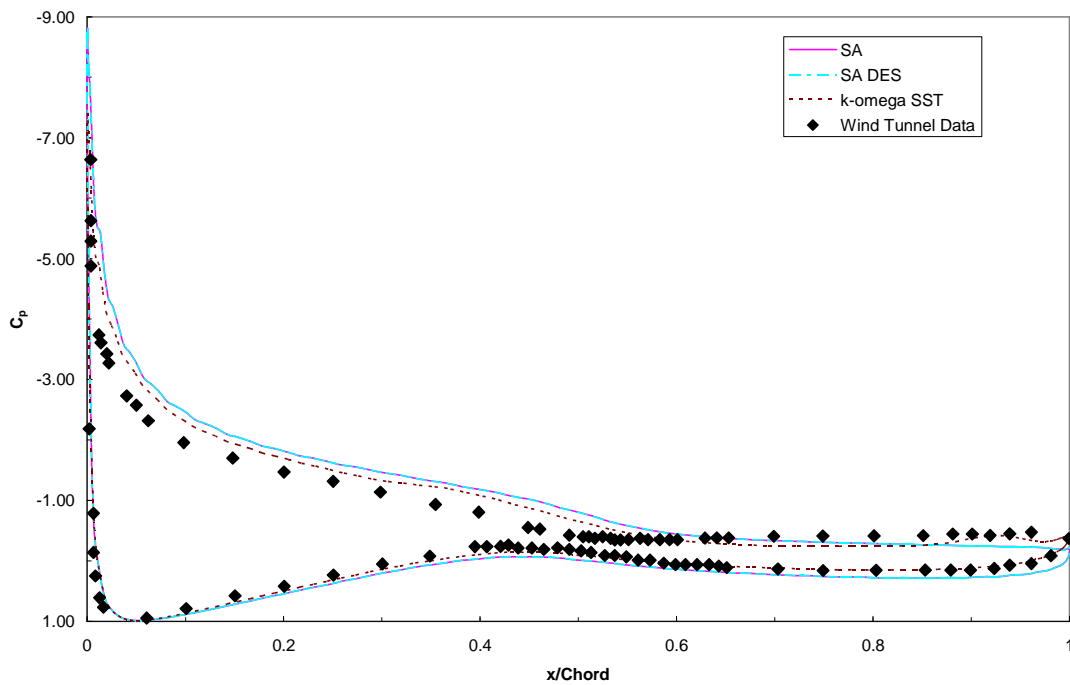
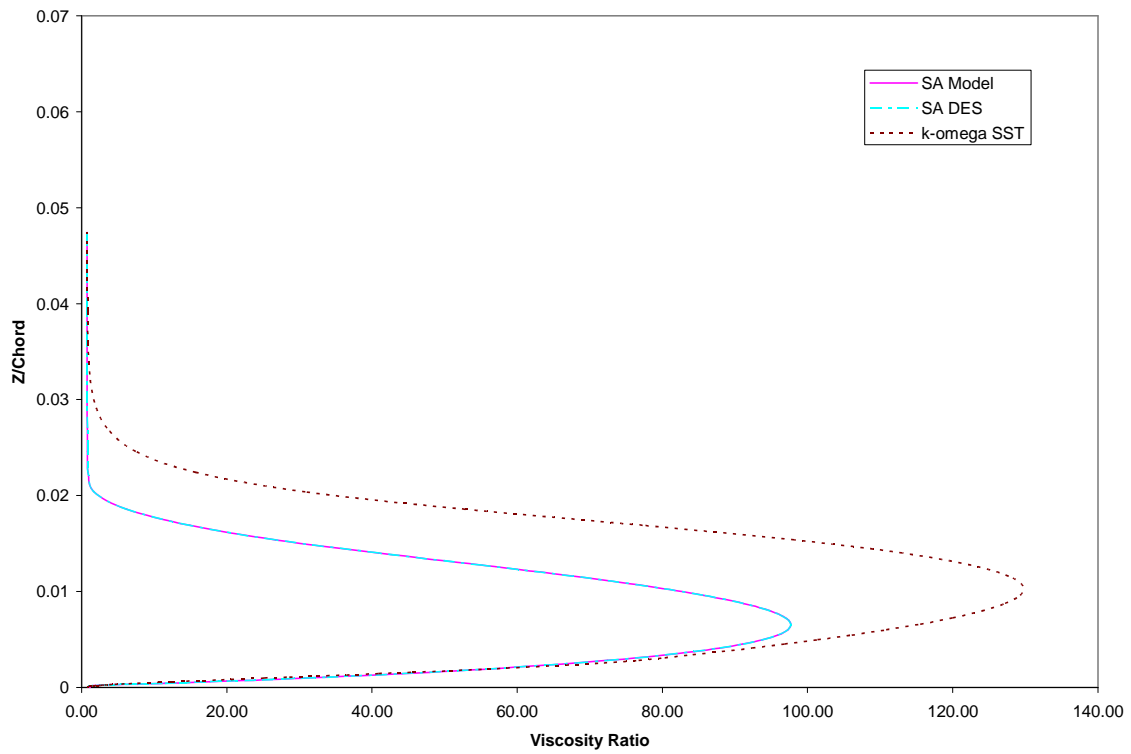
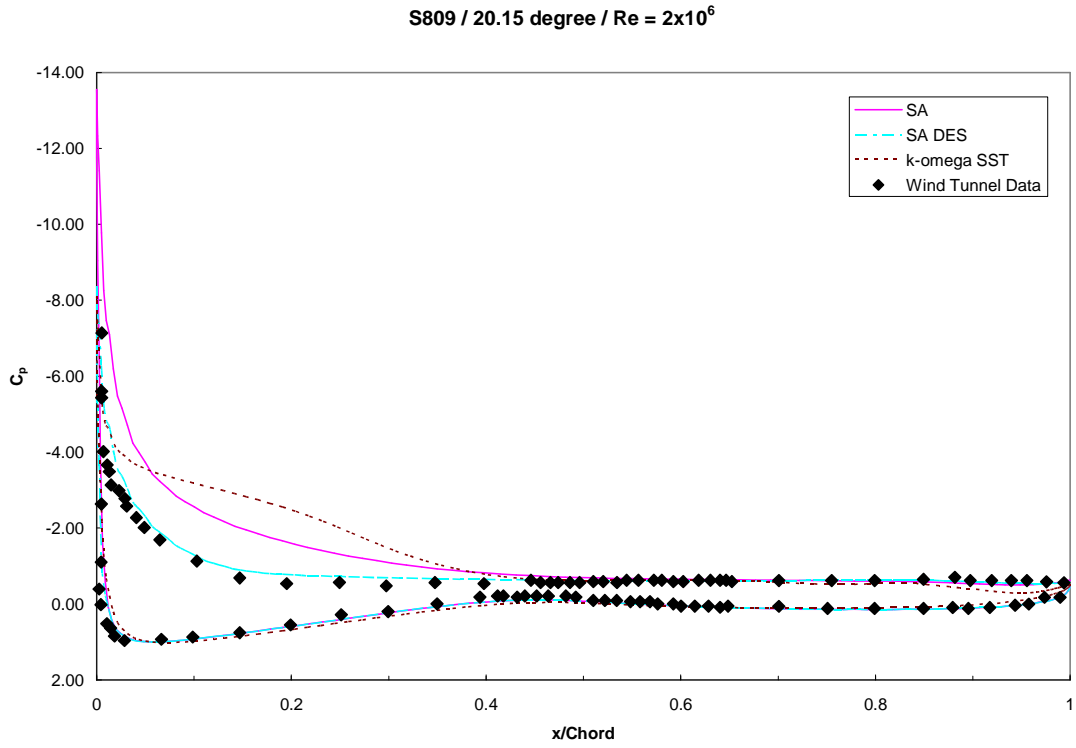
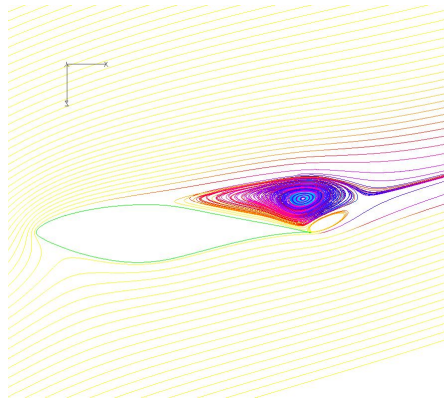
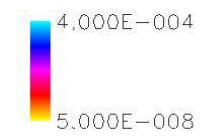
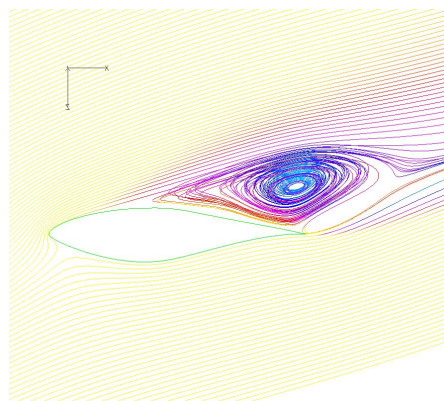


Figure A.7 Pressure Distribution for Angle of Attack = 14.24 degree, Fully Turbulent Calculation

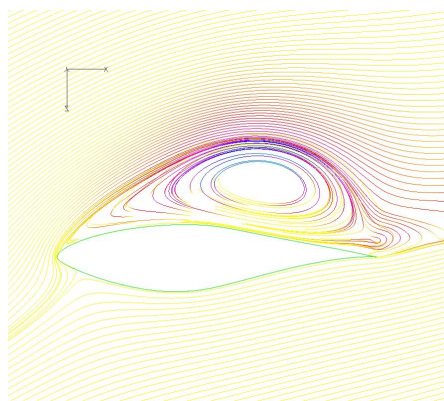




(a)



(b)



(c)

Figure A.10 Stream lines colored by turbulent viscosity $\left(\frac{\mu_T}{\mu_\infty} \cdot \left(\frac{M_\infty}{Re} \right) \right)$ at 20.15° Angle of Attack using (a) SA Model (b) SA DES (c) k-omega SST Model

Figures A.11 and A.12 show variation lift and drag coefficients respectively with angle of attack. It can be noticed that k-omega SST predicts lower lift than both SA model and SA DES. This is again due to the thicken boundary layer causes lower suction on the upper surface in most of the case.

SA DES predicts results almost identical to the SA model up to 14.22° angle of attack. However, as the flow moves towards severe stall, with increasing angle of attack, the DES gives the best performance for reasons discussed earlier.

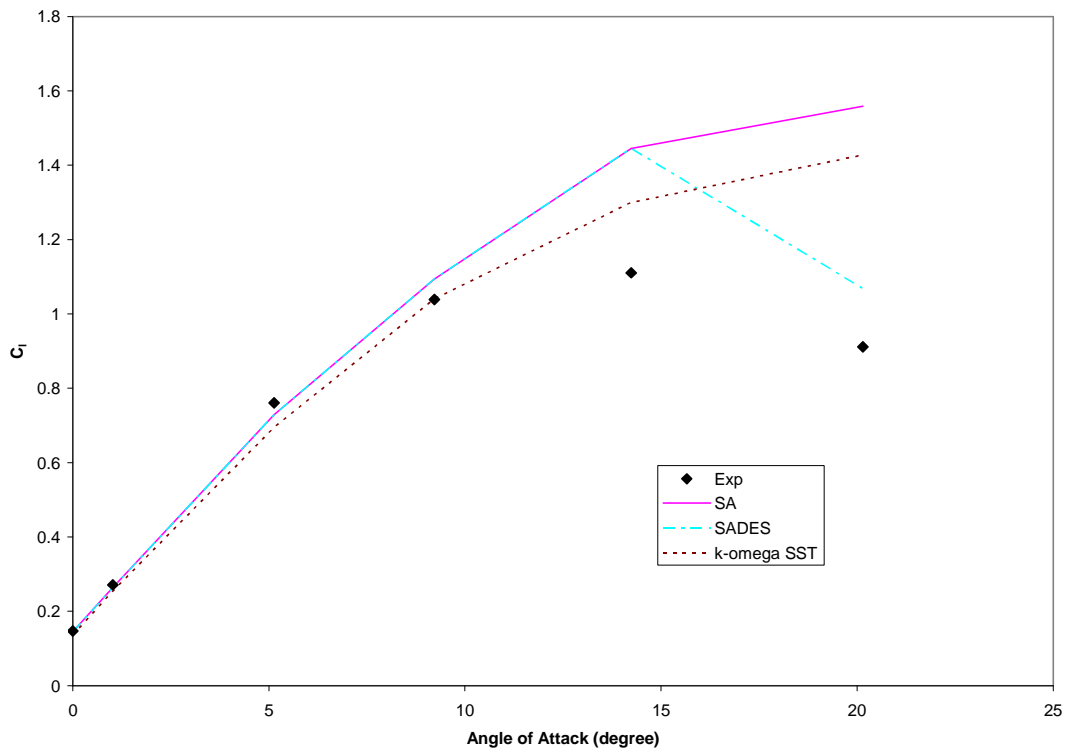


Figure A.11 Lift Coefficients

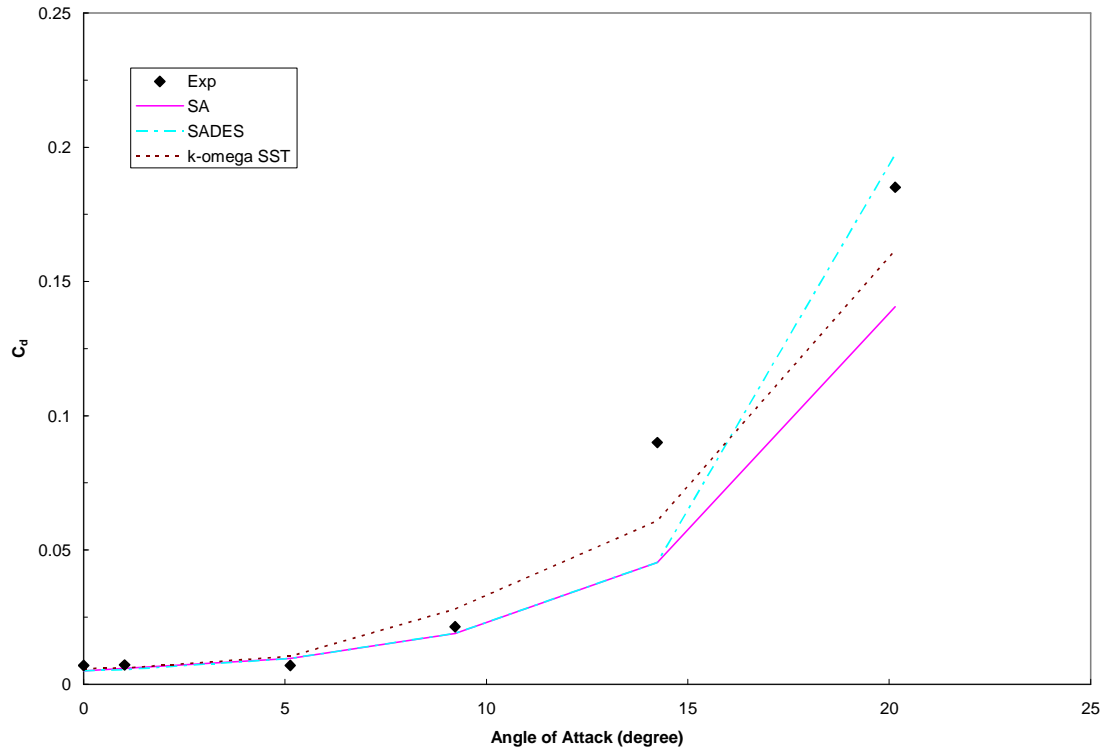


Figure A.12 Drag Coefficients

REFERENCES

- [1] Buhl, M.L., Wright, A.D. and Pierce, K.G. "Wind Turbine Design Codes: A Comparison of the Structural Response," 19th American Society of Mechanical Engineers (ASME) Wind Energy Symposium Reno, Nevada January 10-13, 2000.
- [2] Tangler, J. L., Smith, B. and Jager, D.. "SERI Advanced Wind Turbine Blades," NREL/TP-257-4492, Golden, CO, 1992.
- [3] Eppler, R., *Airfoil Design and Data*, Springer-Verlag, New York, 562pp, 1990.
- [4] Selig, M. S., Donovan, J. F. and Fraser, D. B. *Airfoils at Low Speeds*, Soartech 8, Virginia Beach, VA, H. A. Stokely, 1989.
- [5] Glauert, H. "An Aerodynamic Theory of the Airscrew." *ARC R&M 786*, January 1922.
- [6] Hansen, A. C. and Butterfield, C. P., "Aerodynamics of Horizontal-Axis Wind Turbines," *Annual Review of Fluid Mechanics*. Volume 25, pp. 115-149, 1993.
- [7] Laino, D. and Butterfield, C. P., "Using YAWDYN to Model Turbines with Aerodynamic Control Systems," ASME Wind Energy Conference, New Orleans, 1994.
- [8] Hansen, A.C. and Laino, D.J., "User's Guide to the Wind Turbine Dynamics Computer Programs YawDyn and AeroDyn for ADAMS" 1999 Available for download from: <http://wind.nrel.gov/designcodes/simulators/yawdyn/> (accessed July 25th, 2006).
- [9] Leishman, J. G. and Beddoes, T. S., "A semi-Empirical Model for Dynamic Stall," *Journal of the American Helicopter Society*, Volume 34, pp. 3-17, 1989.
- [10] Marshall L. Buhl Jr., "The NWTC Design-Codes Suite: An Overview," *NREL-NWTC*, January 2005.
- [11] Gerber, Tangler, Duque, and Kocurek, "Peak and Post-Peak Aerodynamics from Phase VI NASA Ames Wind Turbine Data," *Journal of Solar Energy Engineering*, Volume 127, Issue 2, pp. 192-199, May 2005
- [12] Earl P. N. Duque, Wayne Johnson, C. P. vanDam, "Numerical Predictions of Wind Turbine Power and Aerodynamic Loads for the NREL Phase II Combined Experiment Rotor," Proceedings of the 1999 ASME Wind Energy Symposium, Reno, NV, Jan. 1999.

- [13] Earl P. N. Duque, C. P. van Dam, and Shannon C. Hughes, "Navier-Stokes Simulations of The NREL Combined Experiment Phase II Rotor", AIAA paper 99-0037, January 1999.
- [14] Kocurek, D., "Lifting Surface Performance Analysis for Horizontal Axis Wind Turbines," NREL Subcontract Report, SERI/STR-217-3163, Golden, CO, 316 pp., 1987
- [15] Sorensen, N. N., and Michelsen, J. A., "Aerodynamic predictions for the Unsteady Aerodynamics Experiment Phase II rotor at the National Renewable Energy Laboratory", AIAA paper 2000-0037, 2000
- [16] Hand, M. M. ; Simms, D. A. ; Fingersh, L. J. ; Jager, D. W. ; Cotrell, J. R.; Schreck, S. ; Larwood, S. M., "Unsteady Aerodynamics Experiment Phase VI: Wind Tunnel Test Configurations And Available Data Campaigns", NREL/TP-500-29955, December 2001.
- [17] Sørensen, N., Michelsen, J., and Schreck, S., "Navier-Stokes Predictions of the NREL Phase VI Rotor in the NASA Ames 80- by-120 Wind Tunnel", *Wind Energy*, Volume 5, Number 2/3, April-September 2002.
- [18] Madsen, H., Sørensen, N., and Schreck, S., "Yaw Aerodynamics Analyzed with Three Codes In Comparison with Experiment", AIAA-2003-0519, *Proceeding 2003 ASME Wind Energy Symposium*.
- [19] Duque, E., Burklund, M., and Johnson, W., "Navier-Stokes and Comprehensive Analysis Performance Predictions of the NREL Phase VI Experiment," AIAA-2003-0355, *Proceeding 2003 ASME Wind Energy Symposium*.
- [20] Xu, G., "Computational Studies of Horizontal Axis Wind Turbines", *Doctoral Thesis*, School of Aerospace Engineering, Georgia Institute of technology, Atlanta, GA.
- [21] Moulton, M. A., Hafez, M. M. and Caradonna, F. X., "Zonal Procedure for Predicting the Hovering Performance of a Helicopter," *ASME Journal*. Volume 184, 1984.
- [22] Sankar, L.N., Bharadvaj, B. ,Tsung, K., Fu-Lin, "Three-dimensional Navier-Stokes/full-potential coupled analysis for viscous transonic flow", *AIAA Journal*, Volume.31 no.10, pp. 1857-1862, 1993
- [23] Nathan, H. and Sankar, L., "A Review of Computational Techniques for Rotor Wake Modeling," AIAA-2000-0014, *Proceeding 38th AIAA Aerospace Sciences Meeting, Reno, NV, 2000*

- [24] Niazi, S., and Sankar, L., "Computational Analysis of Stall Control Using Bleed Valve in a High-Speed Compressor," AIAA-2000-3507, *Proceeding 36th AIAA Joint Propulsion Conference, Huntsville, AL, 2000*
- [25] Berezin, C., Sankar, L., "Improvements to a tightly coupled viscous-inviscid procedure for three-dimensional unsteady transonic flow," *Computers & Fluid* Volume 26, pp. 689-694, 1997
- [26] Mert E. Berkman; Lakshmi N. Sankar; Charles R. Berezin; Michael S. Torok, "Navier-Stokes/Full Potential/Free-Wake Method for Rotor Flows," *Journal of Aircraft*, Volume.34 no.5, pp.635-640, 1997
- [27] Zhong Yang, Lakshmi N. Sankar, Marilyn Smith, and Olivier Bauchau, "Recent improvements to a hybrid method for rotors in forward flight", AIAA-2000-260, *Proceeding 38th Aerospace Sciences Meeting and Exhibit, Reno, NV, 2000*
- [28] Xu, G. and Sankar, L., "Application of a Viscous Flow Methodology to the NREL Phase VI Rotor", AIAA-2002-0030, *Proceeding 2002 ASME Wind Energy Symposium*
- [29] Xu, G., and Sankar, L., "Computational Study of Horizontal Axis Wind Turbines," AIAA-99-0042, *Proceeding 1999 ASME Wind Energy Symposium*.
- [30] Xu, G., and Sankar, L., "Effects of Transition, Turbulence and Yaw on the Performance of Horizontal Axis Wind Turbines," AIAA-2000-0048, *Proceeding 2000 ASME Wind Energy Symposium*.
- [31] Benjanirat, S., Sankar, L., "Recent Improvements To a Combined Navier-Stokes Full Potential Methodology for Modeling Horizontal Axis Wind Turbines," AIAA-2004-0831 *Proceeding 2004 ASME Wind Energy Symposium*.
- [32] Benjanirat, S., Sankar, L., and Xu, G., "Evaluation of Turbulence Models of the Prediction of Wind Turbine Aerodynamics," AIAA-2003-0517, *Proceeding 2003 ASME Wind Energy Symposium*
- [33] Tongchitpakdee, C., Benjanirat, S. and Sankar, L., "Numerical Simulation of the Aerodynamics of Horizontal Axis Wind Turbines Under Yawed Flow Conditions," AIAA-2005-773, *Proceeding 2005 ASME Wind Energy Symposium*
- [34] Giguère, P. and Selig, M.S., "Design of a Tapered and Twisted Blade for the NREL Combined Experiment Rotor," NREL Subcontract Report, NREL/SR-500-26173.
- [35] Somers, D.M., "Design and experimental results for the S809 airfoil," *NREL/SR-440-6918, 1997*.

- [36] Simms, D., Schreck, S., Hand, M., Fingersh, L., Cotrell, J., Pierce, K. and Robinson, M., "Plans for Testing the NREL Unsteady Aerodynamics Experiment 10-m Diameter HAWT in the NASA Ames Wind Tunnel.", NREL/TP-500-27599, October 1999
- [37] Sankar, L. N., Rou, S. Y., Wake, B. E. Wu, "An efficient procedure for the numerical solution of three-dimensional viscous flows," *AIAA Journal*, AIAA-1987-1159.
- [38] Kocurek, J. D. and Tangler, J. L., "A Prescribed Wake Lifting Surface Hover Performance Analysis," *Proceedings of 32nd Annual Forum of the American Helicopter Society*, May, 1976.
- [39] Baldwin, B. S., and Lomax, H., "Thin Layer Approximation and Algebraic Model for Separated Turbulent Flow," AIAA Paper 78-257, 1978.
- [40] Launder, B. E. and Spalding, D. B. "The Numerical Computation of Turbulent Flows, Comput. Methods, Appl.," *Mech. Eng.*, Volume 3, pp. 269-289, 1974
- [41] Gorski, J.J., "A New Near-Wall Formulation for the k-e Equations of Turbulence," AIAA-86.0556, *Proceeding AIAA 24th Aerospace Sciences Meeting, Reno, Nevada*, 1986
- [42] Spalart, P. R., and Allmaras, S. R., "A One-Equation Turbulence Model for Aerodynamic Flows," AIAA Paper 92-0439, 1992.
- [43] Spalart, P. R., and Allmaras, S. R., "A One-Equation Turbulence Model for Aerodynamic Flows," *La Recherche Aerospatiale*, 1994.
- [44] Karl K. Chen and Noel A. Thyson, "Extension of Emmons' Spot Theory to Flows on Blunt Bodies," *AIAA Journal*, Volume 9 No.5, May 1971.
- [45] Spalart, P.R., Jou, W-H., Strelets, M., And Allmaras, S. "Comments on the Feasibility of LES for Wings and on a Hybrid RAN/LES Approach," *Proceeding 1st AFOSR Int. Conf. on DNS/LES*, Ruston, LA. 1997.
- [46] Camelli, F.E. and Lohner, R., "Combining the Baldwin Lomax and Smagorinsky Turbulence Models to Calculate Flows with Separation Regions," AIAA-2002-0426, *Proceeding AIAA 40th Aerospace Sciences Meeting, Reno, Nevada*, 2002
- [47] Nichols, R.H. and Nelson, C.C., "Application of Hybrid RANS/LES Turbulence Models", AIAA-2003-0083, *Proceeding AIAA 41st Aerospace Sciences Meeting, Reno, Nevada*, 2003

- [48] Batten, P., Goldberg, U., and Chakravarthy, S., "Using Synthetic Turbulence to Interface RANS and LES", AIAA 2003-0081, *Proceeding AIAA 41st Aerospace Sciences Meeting, Reno, Nevada*, 2003
- [49] Kapadia, S. and Roy, S., "Detached Eddy Simulation of Turbine Blade Cooling", AIAA 2003-3632, *Proceeding AIAA 41st Aerospace Sciences Meeting, Reno, Nevada*, 2003
- [50] Nicoud, F., Baggett, J. S., Moin, P., and Cabot, W., "Large eddy simulation wall-modeling based on suboptimal control theory and linear stochastic estimation", *Physics of Fluids*, Volume 13, Number 10, pp. 2968-2983, 2001
- [51] Constantinescu, G. S. and Squires, K. D., "LES and DES investigation of turbulent flow over a sphere", AIAA-2000-0540, *Proceeding AIAA 38th Aerospace Sciences Meeting, Reno, Nevada*, 2003
- [52] Johansen, J., Sorensen, N. N., Michelsen, J. A., and Schreck, S., "Detached-Eddy Simulation of Flow Around the NREL Phase VI Blade", *Wind Energy* ; Volume 5 185-197, 2002
- [53] Menter, F. R., "Zonal Two Equation $k-\omega$ Turbulence Models for Aerodynamic Flows", AIAA 93-2906, *Proceeding 23rd Fluid Dynamics, Plasmadynamics, and Lasers Conference*, Orland FL, 1993
- [54] Wilcox, D.C., "Reassessment of the Scale Determining Equation for Advanced Turbulence Models," *AIAA Journal*, Volume 26, No. 11, pp 1299-1310, 1998
- [55] David C. Wilcox, *Turbulence Modeling for CFD, second edition*, DCW Industries, 2000.
- [56] Langtry, R.B. and Sjolander, S.A., "Prediction of Transition for Attached and Separated Shear layers in Turbomachinery," AIAA 2002-3641, *Proceeding 38th AIAA Joint Propulsion Conference*, Indianapolis, Indiana, 2002
- [57] David C. Wilcox, "Simulation of Transition with a Two-Equation Turbulence Model," *AIAA Journal*, Volume 32, No.2, February 1994.
- [58] Jameson and D.A. Caughey, "How Many Steps are Required to Solve the Euler Equations of Steady Compressible Flow: In Search of a Fast Solution Algorithm", AIAA 2001-2673AIAA, *Proceeding 15th Computational Fluid Dynamics Conference*, Anaheim, CA, 2001
- [59] Wright, C. and Pampolini, G., "Data-parallel Lower-Upper Relaxation Method for the Navier-Stokes Equations," *AIAA Journal*, Volume 34, no.7 pp.1371-1377, 1996

- [60] Wright, C., and Bose, D., “Data-Parallel Line Relaxation Method for the Navier-Stokes Equations,” *Proceeding 13th AIAA Computational Fluid Dynamics Conference*, Snowmass Village, CO, 1997
- [61] Warming, R. F. and Beam, R. M., “An extension of a-stability to alternating direction implicit methods,” *BIT*, vol. 19, pp. 395–417, 1979.
- [62] Eggleston, D. M. and Stoddard, F. S., *Wind Turbine Engineering Design*, Van Nostrand Reinhold, New York, 1987.
- [63] Glauert, H. “*Airplane Propellers.*” *From Div. L, Aerodynamic Theory*, ed. W. F. Durand. Berlin: Springer Verlag, 1935 (Reprinted by Peter Smith, Glouster, Mass., 1976.).
- [64] Tony Burton and others, *Wind Energy Handbook* John Wiley and Sons, London, 2001
- [65] Wilson, R. E., and Lissaman, P. B. S. *Applied Aerodynamics of Wind Power Machines*. Oregon State University, 1974.
- [66] Stoddard, F. S. “Momentum theory and flow states for windmills,” *Wind Technology Journal* 1, No. 1, Spring, 1977.
- [67] Sorensen, J. N., Shen, W. Z. and Munduate, X., “Analysis of Wake States by a Full-field Actuator Disc Model,” *Wind Energy*, Volume 1, pp.73-88, 1998.
- [68] Gleize, V., Szydowski, J. and Costes, M., “Numerical and Physical Analysis of The Turbulent Viscous Flow Around a NACA0015 Profile at Stall,” ECCOMAS 2004, Jyvaskyla (Finland)
- [69] Renaud, T., O’Brien, D., Smith M., Potsdam, M., “Evaluation of Isolated Fuselage and Rotor-Fuselage Interaction Using CFD,” *AHS forum proceeding*, 2005
- [70] Bardina, J. E., Huang, P. G. and Coakley, T.J., “Turbulence Modeling Validation, Testing, and Development,” *NASA Technical Memorandum* 110446, April 1997
- [71] Wolfe, W.P. and Ochs, S.S. “CFD Calculations of S809 Aerodynamic Characteristics,” AIAA-97-0973, *Proceeding 35th AIAA Aerospace Sciences Meeting and Exhibit*, Reno 1997
- [72] Yang, S.L. , Chang, Y.L. and O. Arici, “Incompressible Navier-Stokes Computation of the NREL Airfoils Using a Symmetric Total Variational Diminishing Scheme,” *Journal of Solar Energy Engineering*, Volume 116, pp. 174-182, 1994

- [73] Langtry R.B., Gola J., and Menter, F.R., "Predicting 2-D and 3-D Wind Turbine Performance using a Transition Model for General CFD Codes," AIAA 2006.0395, *Proceeding 44th AIAA Aerospace Sciences Meeting and Exhibit*, Reno 2006.
- [74] Hanjalic K., Launder B. E., and Schiestel, R., "Turbulent Shear Flows 2," *Selected papers from the Second International Symposium on Turbulent Shear Flows*, Imperial College London, July 24 ,1979 (Springer, Berlin, 1980), p. 36.
- [75] Kim,S.W. and Chen,C.P., "A multi-time-scale turbulence model based on variable partitioning of the turbulent kinetic energy spectrum", *Numerical Heat Transfer*, Volume 16, pp.193-211, 1998
- [76] Liou, W.W., Shih, T.H., and Duncan, B.S., "A multiple-scale model for compressible turbulent flows," *Physics of Fluids*, Volume 7, pp.658-666, 1995

VITA

Sarun Benjanirat was born in Chiangmai, Thailand on July 25th, 1974. He graduated from Montfort College of Chiangmai, Thailand in 1991. He received a Bachelor degree in Mechanical Engineering from Chulalongkorn University in June 1995. He worked in a utility company for 3 years then was a lecturer in Burapha University, Chonburi until August 2000. He entered the graduate program at Georgia Institute of Technology in fall semester of 2000 and was granted funding to work in wind energy project from National Renewable Energy Laboratory. He earned his Master's Degree from School of Aerospace Engineering in December 2001.

He is a student member of the American Institute of Aeronautics and Astronautics. He is the son of Mr. and Mrs. Benjanirat, Chiangmai, Thailand.